

論文 / 著書情報
Article / Book Information

題目(和文)	トポロジカル半金属およびギャップレス超伝導体のトポロジカル相転移
Title(English)	Topological phase transitions of topological semimetals and gapless superconductors
著者(和文)	奥川亮
Author(English)	Ryo Okugawa
出典(和文)	学位:博士(理学), 学位授与機関:東京工業大学, 報告番号:甲第10721号, 授与年月日:2018年3月26日, 学位の種別:課程博士, 審査員:村上 修一,西田 祐介,古賀 昌久,西森 秀稔,平原 徹
Citation(English)	Degree:Doctor (Science), Conferring organization: Tokyo Institute of Technology, Report number:甲第10721号, Conferred date:2018/3/26, Degree Type:Course doctor, Examiner:,,,,,
学位種別(和文)	博士論文
Type(English)	Doctoral Thesis

Topological phase transitions of topological semimetals and gapless superconductors

Department of Physics, Tokyo Institute of Technology
Ryo Okugawa

Abstract

Topological materials have attracted attentions in condensed matter physics because of various topological properties. As a manifestation of the topological nontriviality, topological surface states appear in the topological materials for instance. To investigate the characteristic properties, we need to establish a way to search for the topological materials systematically. Therefore, in this thesis, we study topological phase transitions involving topological semimetals and gapless superconductors.

Firstly, we study band evolution of surface states when a topological phase transition happens from a Weyl semimetal phase to a topological insulator phase. To see the band evolution, we focus on time-reversal invariant systems without inversion symmetry, where both of the Weyl semimetal and the topological insulator can be realized. By using an effective Hamiltonian and a lattice model, we reveal a relationship between the Weyl semimetal and the topological insulator in the view of the surface states.

Secondly, we clarify a general phase transition from a topological nodal-line semimetal phase to spinless Weyl semimetal phase. We classify topological nodal-lines according to their locations and shapes in the three-dimensional Brillouin zone in order to elucidate the topological phase transition. From the classification, we show that the phase transition under symmetry breaking varies depending on the type of the nodal lines. Furthermore, we discuss how crystallographic symmetries affect the topological phase transition in the topological nodal-line semimetal.

Finally, we investigate topological phase transitions in three-dimensional odd-parity or noncentrosymmetric superconductors with mirror symmetry when the system breaks time-reversal symmetry. In the three-dimensional superconductors with mirror symmetry, Weyl superconductor and topological crystalline superconductor phases are realizable as well as a trivial superconductor phase. To clarify a relationship among these superconducting phases, we construct a universal topological phase diagram in the mirror-symmetric superconductors. As a result, it is shown that the Weyl superconductor phase generally appears between the trivial and the topological crystalline superconductor phases. We also demonstrate how a trajectory of the Weyl nodes determines topological invariants which characterize the topological phases.

Acknowledgements

I would like to thank my supervisor, Prof. Shuichi Murakami for helpful discussion and generous support. During my student life, I acquired a lot of knowledge of physics from him. I could complete our papers thanks to his invaluable advice and insightful comments. Without his help, I could have not accomplish my work. I also thank Assistant Prof. Takehito Yokoyama. He inspired me to study a new theme of topological materials.

Moreover, I acknowledge collaborations with Dr. Motoaki Hirayama, Dr. Shoji Ishibashi, and Dr. Takashi Miyake. Through the instructive collaboration, I learned material science. I also express gratitude to Junya Tanaka, Prof. Takashi Koretsune and Prof. Susumu Saito. The fruitful collaborations with them were beneficial to my research. I must thank members of our group for stimulating discussions: Akihiro Okamoto, Taiki Yoda, Masato Hamada, Heejae Kim, Ryo Takahashi, Kazuki Yokomizo, Tomohiro Inoue, Ryo Furuta, Yusuke Aihara, Manabu Takeichi, Daisuke Hara and Dr. Kokin Nakajin. I also thank research and educational assistant Rie Tsukui. I am grateful to all members of the Condensed Matter Theory Group at Tokyo Tech. for great assistance.

Finally, I express my appreciation to my parents for encouragement to study physics.

Contents

Abstract	i
Acknowledgements	ii
1 Introduction	1
2 Topological materials	4
2.1 Topological insulators	4
2.1.1 Chern insulator	4
2.1.2 Edge states	7
2.1.3 \mathbb{Z}_2 Topological insulator	8
2.1.4 Strong TIs and weak TIs	10
2.1.5 Surface fermion parity	11
2.2 Topological semimetals	13
2.2.1 Weyl semimetal	13
2.2.2 Stability of the Weyl nodes	14
2.2.3 Fermi arc	16
2.2.4 Phase diagram for the time-reversal invariant WSM	17
2.2.5 Gap closing in noncentrosymmetric materials	19
2.2.6 General theory of the Gap closing and the topological phase transitions	22
2.2.7 Topological nodal-line semimetals	23
2.2.8 Topological protection of the topological nodal-line	24
2.2.9 Spinless nodal-line semimetals protected by mirror sym- metry	25
2.2.10 Spinless Weyl semimetals	25
2.3 Topological superconductors	26
2.3.1 Bogoliubov-de Gennes Hamiltonian	26
2.3.2 Spinless chiral p -wave superconductors	28
2.3.3 Weyl superconductors	29
2.3.4 Topological crystalline superconductors	29
2.3.5 Detection of topological superconductivity	31

3	Topological surface states and their evolution in Weyl semimetal and topological insulator phases	32
3.1	Effective Hamiltonian for NI-WSM-TI phase transition	33
3.1.1	Construction of the effective Hamiltonian	33
3.1.2	Surface states from the effective Hamiltonian	34
3.2	Numerical calculation of surface states of Weyl semimetal in a lattice model	38
3.2.1	Model	38
3.2.2	Numerical calculation of surface states	39
3.2.3	WSM-TI phase transition and evolution of the Fermi-arc surface states	42
3.3	Conclusion	45
4	Topological phase transition of spinless topological semimetals	46
4.1	Classification of TNLSMs into two types	47
4.2	Phase transition involving TNLSMs	50
4.2.1	Type-A TNLSMs with broken time-reversal symmetry	50
4.2.2	Type-A TNLSMs with inversion-symmetry breaking	51
4.2.3	Type-B TNLSMs with broken time-reversal or inversion symmetry	52
4.2.4	Phase transition in a lattice model	52
4.3	Crystal symmetries and band structures of type-A TNLSMs	53
4.3.1	Band structures of the type-A TNLSMs	53
4.3.2	Applications of the theory of the band structures to the candidate materials of TNLSMs	55
4.4	Phase transitions of type-A TNLSMs and crystal symmetries	55
4.4.1	Type-A TNLS protected by crystal symmetries with broken time-reversal symmetry	55
4.4.2	Type-A TNLS protected by crystal symmetries with inversion-symmetry breaking	56
4.5	Conclusion and discussion	57
5	General phase transition of Weyl superconductivity in mirror-symmetric superconductors	59
5.1	Theory of gap closing in mirror-symmetric superconductors	60
5.1.1	Gap closing in noncentrosymmetric SCs	60
5.1.2	Gap closing in inversion-symmetric SCs	61
5.2	General phase transition of Weyl superconductivity in mirror-symmetric superconductors	62
5.3	Model calculation	65
5.4	Evolution of Majorana surface states: from Majorana arc to Majorana cone	66
5.5	Conclusion and discussion	69
6	Summary and Outlook	70

A Classification of the type-A TNLs and their band structures	72
List of Publications and Preprints	81
List of Publications	81
List of Preprints	81

Chapter 1

Introduction

The twenty-first century has seen development of a new field in condensed matter physics; topological phases. The topological phases are characterized by nontrivial topology of the wavefunctions of the system. Therefore, the topological phase emerges through a change of the band topology, i.e. a topological phase transition. Thus, the phase transition is not conventional because the topological phases cannot be understood from spontaneous symmetry breaking. Namely, the topological phase transition is one of the quantum phase transitions at zero temperature. The first example of the topological phases in electronic systems is a quantum Hall insulator, which was reported in 1980 [1]. Nevertheless, a new topological phase was not realized until the theoretical prediction of \mathbb{Z}_2 topological insulators in 2005 [2, 3]. After that, the \mathbb{Z}_2 topological insulator was observed experimentally in 2007 [4]. Since the discovery of the \mathbb{Z}_2 topological insulators, various works on the topological phases have been created countlessly until now [5, 6].

As the name suggests, such topological insulators are distinguished from ordinal ones by topological invariants which are integral. As one of their intriguing features, we can see robust gapless edge or surface states characterized by the topological invariants. In the two-dimensional topological insulators, there exist gapless edge states protected topologically, while their bulk states are gapped. The protection originates from the fact that the topological invariant takes an integer. Namely, because the topological invariant is not continuously changed if perturbations are added, the edge states are protected. Then, the idea of the topological insulator was applied to superconductors because their band structures are also basically gapped [7]. If gapped superconductors are topologically nontrivial, it is called topological superconductors, which have gapless edge excitations as with the topological insulators. As a result, many topological phases have been theoretically suggested in the gapped matters.

The concept was extended to matters with gapless bulk states, subsequent to theoretical proposal of the topological gapped phase. An early example of topological gapless phases is a Weyl semimetal [8, 9]. The Weyl semimetal hosts gapless point nodes protected topologically in the bulk. There also appear topo-

logical surface states called Fermi arcs in the Weyl semimetal. Moreover, such gapless phase can be realized in nodal superconductors, in which the gaplessness is also generally protected by topology. The quantum matters in the topological gapped or gapless phases are generally known as topological materials.

In the topological materials, symmetries also play a fundamental role because they determine topological structures of the system. In other words, distinct topological phases appear depending on the symmetries of the system. For example, the quantum Hall insulator is realizable only when time-reversal symmetry is broken. On the other hand, the \mathbb{Z}_2 topological insulator is realizable when time-reversal symmetry is present. Furthermore, it is known that crystal symmetries lead to new topological phases, which are named topological crystalline phases [10, 11]. Nowadays, various topological phases are proposed from systematic topological classifications of the quantum matters based on symmetries [12].

Thanks to such topological gapless states, the topological materials have potential for application to spintronics and quantum computation. Moreover, their low-energy excitations obey the same equations as those for the Weyl fermions, the Majorana fermions and so on, which have been discussed in particle physics [13–15]. Thus, the topological materials also have attracted attention as matters which will exhibit phenomena analogous with high-energy physics [13, 16]. Hence, the topological materials are expected to open new solid-state physics through the complex interplay between topology and symmetry. However, few topological materials have been established experimentally, and therefore, discovery of them is imperative.

For experimental observation of the topological materials, theoretical predictions are very important. Therefore, we need to search for candidate materials with nontrivial band structures. Meanwhile, for the search of topological materials, we can use topological phase transitions which leads to topologically nontrivial phases. From the knowledge of the topological phase transitions, we can get a deep insight into the classes of the topological materials. Therefore, it is important to establish a universal theory of the topological phase transitions, which is independent of microscopic details of the matters. In other words, the theory must depends only on the symmetries of the systems. Furthermore, we need to elucidate band evolution when the topological phase transition happens since many properties including transport properties are determined by the band structure.

In this thesis, we study topological phase transitions involving topological semimetals and gapless superconductors. First, we discuss changes of the surface states when the topological phase transition happens from the Weyl semimetal to the topological insulator. While the topological insulator has Dirac cones on the surface, the Weyl semimetal has Fermi arcs. Therefore, we clarify how these different surface states are related in the topological phase transition. Secondly, we investigate topological phase transitions between topological nodal-line semimetals and Weyl semimetals in spinless systems. The topological nodal-line semimetal has line nodes in the momentum space, unlike the Weyl semimetal. We give conditions to realize the Weyl semimetal phase

from the topological nodal-line semimetal phase. Finally, we study topological phase transition in superconducting phases. Superconductors can be gapped or gapless topological phases such as a Weyl phase and a topological crystalline phase. The topological crystalline superconductor is a topologically nontrivial gapped phase which is realizable in the presence of mirror symmetry. We construct a universal phase diagram for the Weyl and the topological crystalline superconductors.

The thesis is organized as follows. Particularly, Chapters 3, 4 and 5 are based on the author's papers [17], [18] and [19], respectively. In Chapter 2, we review various topological materials in previous works, especially related to the thesis. In Chapter 3, we discuss evolution of surface states of a Weyl semimetal and a topological insulator when a topological phase transition happens between these two phases. We construct an effective model to describe general structures of the surface states of the Weyl semimetal. Then, we investigate the band evolution by using a lattice model when the topological phase transition occurs. In Chapter 4, we study topological phase transitions between topological nodal-line semimetal and spinless Weyl semimetal phases by using an effective model and a lattice model. In particular, we discuss a relationship between the topological phase transition and shapes of the nodal line. We also reveal effects of crystal symmetries on the topological phase transition and the band structures. In Chapter 5, we show that the Weyl superconductor phase generally appears between the trivial and the topological crystalline superconductor phases if time-reversal symmetry is broken. The results can be generally explained from an effective model. We also elucidate band evolution of the bulk and the surface in the topological phase transition by using a lattice model. In Chapter 6, we summarize the conclusions of the previous chapters.

Chapter 2

Topological materials

In this chapter, we review topological materials. In Sec. 2.1, we explain topological insulators such as Chern insulators and \mathbb{Z}_2 topological insulators. In particular, we see topological invariants and topological surface states because they characterize the topological insulators. Next, we discuss topological semimetals including Weyl semimetals and topological nodal-line semimetals in Sec. 2.2. In Sec. 2.2, we focus on a gap closing to realize the topological semimetals. In the last Sec. 2.3, topological properties of superconductors are described. In the mean-field theory, the Bogoliubov de-Gennes Hamiltonian and the gap function determine the properties of the superconductors. By using the Bogoliubov de-Gennes Hamiltonian, we can treat gapped and nodal superconductors in the similar way as insulators and semimetals, respectively. Therefore, we show several topological superconductors as analogues of the topological insulators and the topological semimetals. In Sec. 2.3, we introduce spinless chiral superconductors, Weyl superconductors, and topological crystalline superconductors.

2.1 Topological insulators

2.1.1 Chern insulator

In 1980, quantization of the Hall conductivity was discovered in a two-dimensional system with an external magnetic field by von Klitzing et al. [1], which is called quantum Hall effect. The quantum Hall effect is observed under the magnetic field perpendicular to the two-dimensional electron gas at low temperatures, when the Fermi level is in the gap between the Landau levels. Thereafter, Haldane suggested theoretically a model which shows the quantum Hall effect even without the external magnetic field when time-reversal symmetry is broken [20]. The phenomenon is named anomalous quantum Hall effect. While the Haldane model is a toy model, recently the anomalous quantum Hall effect was established experimentally in thin films of chromium-doped $(\text{Bi,Sb})_2\text{Te}_3$ [21]. Such insulators which show the anomalous quantum Hall effect are called Chern insulators.

In this subsection, we explain how the quantization comes from band topology. Here we consider two-dimensional systems in the xy plane. The Hall conductivity at zero temperature is calculated from the Kubo formula [22]. When the Fermi energy E_F lies in the gap, the Hall conductivity is

$$\sigma_H = \frac{e^2}{h} \frac{1}{2\pi i} \sum_{m=1}^{occ.} \int_{BZ} d\mathbf{k} \left(\left\langle \frac{\partial u_{m\mathbf{k}}}{\partial k_x} \middle| \frac{\partial u_{m\mathbf{k}}}{\partial k_y} \right\rangle - \left\langle \frac{\partial u_{m\mathbf{k}}}{\partial k_y} \middle| \frac{\partial u_{m\mathbf{k}}}{\partial k_x} \right\rangle \right), \quad (2.1)$$

where $u_{m\mathbf{k}}$ represents the Bloch function with the band index m and the wave vector $\mathbf{k} = (k_x, k_y)$. $-e$ and \hbar are the electron charge and the Planck constant, respectively. In Eq. (2.1), the sum is taken over the occupied bands below the Fermi energy, and the integral is performed over the two-dimensional Brillouin zone (BZ). Here, we introduce the Berry connection given by [23]

$$\mathbf{A}_m(\mathbf{k}) = i \langle u_{m\mathbf{k}} | \nabla_{\mathbf{k}} | u_{m\mathbf{k}} \rangle. \quad (2.2)$$

By using the Berry connection, we can rewrite the formula of the Hall conductivity as

$$\sigma_H = -n \frac{e^2}{h}, \quad (2.3)$$

$$n = \sum_{m=1}^{occ.} \int \frac{d\mathbf{k}}{2\pi} (\nabla_{\mathbf{k}} \times \mathbf{A}_m)_z \equiv \sum_{m=1}^{occ.} n_m. \quad (2.4)$$

We can show that n is an integer as follows. Because the integral over the BZ becomes a line integral along the boundary of the BZ from the Stokes theorem, Eq. (2.4) becomes

$$n_m = \frac{1}{2\pi} \oint d\mathbf{k} \cdot \mathbf{A}_m(\mathbf{k}). \quad (2.5)$$

From this formula, n_m seems to be always zero. However, this argument is not always correct; n_m can become nonzero since Eq. (2.5) is applicable only when there are no singularities of \mathbf{A}_m in the BZ. To use the Stokes theorem in the cases where \mathbf{A}_m has singularities, we need to do a gauge transformation to avoid the singularities. In other words, we need to divide the BZ into some regions in each of which the Berry connections are written in its individual gauge. If the BZ is divided into two regions R^1 and R^2 without singularities, we obtain

$$n_m = \frac{1}{2\pi} \int_{R^1} d\mathbf{k} (\nabla_{\mathbf{k}} \times \mathbf{A}_m^1)_z + \frac{1}{2\pi} \int_{R^2} d\mathbf{k} (\nabla_{\mathbf{k}} \times \mathbf{A}_m^2)_z. \quad (2.6)$$

Here, \mathbf{A}_m^i is the Berry connection smoothly defined in the region R^i . On the boundary between R^1 and R^2 , the eigenstates $|u_{m\mathbf{k}}^1\rangle$ and $|u_{m\mathbf{k}}^2\rangle$ are related by the gauge transformation $|u_{m\mathbf{k}}^2\rangle = e^{if(\mathbf{k})} |u_{m\mathbf{k}}^1\rangle$, where $f(\mathbf{k})$ is a real function. It yields

$$\mathbf{A}_m^2(\mathbf{k}) = \mathbf{A}_m^1(\mathbf{k}) - \nabla_{\mathbf{k}} f(\mathbf{k}). \quad (2.7)$$

Because the Stokes theorem can be used in each region, we obtain

$$n_m = \frac{1}{2\pi} \oint_{\partial R} d\mathbf{k} \cdot \nabla_{\mathbf{k}} f(\mathbf{k}), \quad (2.8)$$

where ∂R represents the boundary between the two regions. From Eq. (2.8), n_m is an integer. As a result, n is also an integer and it is called a Chern number, which is a topological invariant. Therefore, when the Chern number is nonzero, there is an obstruction to choosing a single gauge in the whole BZ. This means that the nonzero Chern number stems from the nontrivial topology of the fiber bundle on the BZ [24].

Because the Chern number n is integral, n cannot change by continuous deformation of the system. Here, the continuous deformation of the system means a continuous change of the parameters in the Hamiltonian without a gap closing [25]. Below, we show that n changes when the band gap closes [Fig. 2.1]. To see the change of n , let us consider a massive Dirac Hamiltonian described by

$$H(\mathbf{k}) = k_x \sigma_x + k_y \sigma_y + m \sigma_z. \quad (2.9)$$

Because the eigenvalues are $E_{\pm}(\mathbf{k}) = \pm \sqrt{k^2 + m^2}$, the gap closes when $m = 0$. We assume $E_F = 0$. Between $m < 0$ and $m > 0$, the change of the Chern number is given by

$$\Delta n = \frac{1}{2\pi} \int d\mathbf{k} (\boldsymbol{\Omega}_-(m > 0))_z - \frac{1}{2\pi} \int d\mathbf{k} (\boldsymbol{\Omega}_-(m < 0))_z. \quad (2.10)$$

Here, $\boldsymbol{\Omega}_- = \nabla_{\mathbf{k}} \times \mathbf{A}_-$ whose subscript $-$ indicates the occupied band. $\boldsymbol{\Omega}_m = \nabla_{\mathbf{k}} \times \mathbf{A}_m$ is called Berry curvature [23]. We obtain $(\boldsymbol{\Omega}_-)_z = \frac{m}{2(k^2 + m^2)^{3/2}}$ from Eq. (2.9). Thus, we obtain

$$\Delta n = 1. \quad (2.11)$$

Hence, it is proved that the gap closing accompanies the change of the Chern number.

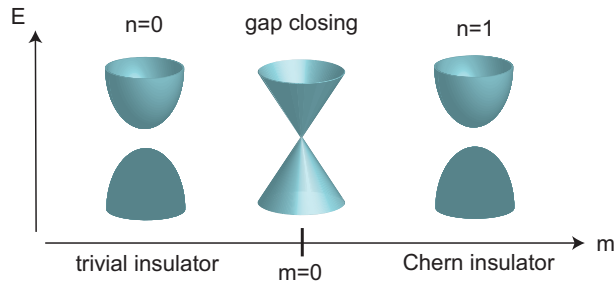


Figure 2.1: Gap closing in the bulk energy bands by the change of m . This example illustrates the relationship between the gap closing and the change of the Chern number n .

2.1.2 Edge states

In the Chern insulator, the bulk cannot carry an electric current since the Fermi energy lies in the gap. Nevertheless, the Hall conductivity is nonzero. Namely, the nonzero Hall conductivity means that the electric current flows along the edges as illustrated in Fig. 2.2(a). Therefore, the quantum Hall system is insulating in the bulk, and is metallic in the edge. In this subsection, we see that the Chern insulators have gapless edge states protected by the nontrivial topology.

We consider a boundary between a Chern insulator and vacuum. Because in the vacuum the Chern number is zero, the Chern number varies at the boundary. As shown in the previous subsection, a change of the Chern number requires a gap closing. Therefore, gapless states are expected to appear at the boundary. Actually, we can derive the gapless states from Eq. (2.9) [Fig. 2.2(b)]. To derive the edge states, we set the boundary at $y = 0$ along the x direction. In order to introduce the change of the Chern number, we assume that $m(y) < 0$ for $y < 0$, and that $m(y) > 0$ for $y > 0$. Now since k_y is not a good quantum number, Eq. (2.9) becomes

$$H(k_x, y) = k_x \sigma_x - i \partial_y \sigma_y + m(y) \sigma_z. \quad (2.12)$$

Then, we can confirm that this equation gives the gapless edge states with $E = k_x$ described by

$$\psi(x, y) = e^{ik_x x} e^{-\int_0^y m(y') dy'} \frac{1}{\sqrt{2}} \begin{pmatrix} 1 \\ -1 \end{pmatrix}. \quad (2.13)$$

The gapless edge states are called chiral edge states, which correspond to a chiral Dirac fermion. The chiral edge states originate from the nontrivial Chern number in the bulk. Namely, the topology of the bulk Hamiltonian determines existence of the edge states. This is called bulk-edge correspondence [26]. Therefore, as long as a Chern number is nonzero, the chiral edge states are guaranteed to exist. Hence, the chiral edge states are protected topologically because the Chern number is unchanged by small perturbations.

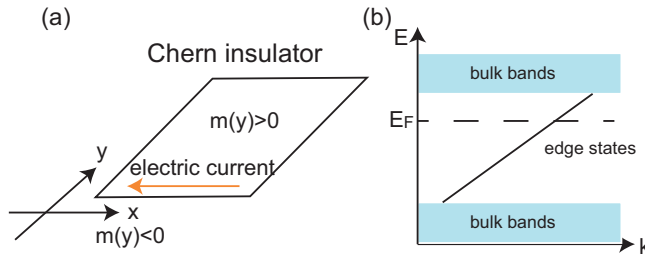


Figure 2.2: (a) Electric currents along the boundary between the Chern insulator and the vacuum. (b) Edge states in the Chern insulator. E_F represents the Fermi energy.

2.1.3 \mathbb{Z}_2 Topological insulator

A \mathbb{Z}_2 topological insulator (TI) is a quantum phase proposed theoretically by Kane and Mele in 2005 [2,3]. The \mathbb{Z}_2 TI is realized in a time-reversal symmetric system. In the \mathbb{Z}_2 TI, a spin current flows along the edges unlike the Chern insulator because of the time-reversal symmetry. The \mathbb{Z}_2 TIs can be realized both in two- and three-dimensional systems [27–29], and various TIs have been discovered experimentally [4,30,31].

When the time-reversal symmetry is present, the Chern number is always zero [32]. Thus, the Chern number cannot be used to determine whether time-reversal invariant systems are topologically nontrivial or not. Therefore, topological distinction of time-reversal invariant systems had not been established until the theoretical suggestion of the \mathbb{Z}_2 TI by Kane and Mele [2,3]. Kane and Mele suggested that graphene gapped by the spin-orbit coupling is a two-dimensional \mathbb{Z}_2 topological insulator (2DTI). Then, a new topological invariant ν was introduced to distinguish the 2DTI and normal insulator (NI). ν is called a \mathbb{Z}_2 topological number. Here, we see definition of the \mathbb{Z}_2 topological number characterizing the edge states of the \mathbb{Z}_2 TI.

We begin with a 2DTI. To define the \mathbb{Z}_2 topological number, let us introduce time-reversal invariant momenta (TRIM) represented by

$$\mathbf{\Gamma}_{i=(n_1,n_2)} = \frac{1}{2}(n_1\mathbf{G}_1 + n_2\mathbf{G}_2), \quad (n_j = 0, 1), \quad (2.14)$$

where $\mathbf{G}_{1,2}$ are the primitive reciprocal lattice vectors. The TRIM satisfy $\mathbf{\Gamma} = -\mathbf{\Gamma} \pmod{\mathbf{G}}$. By using Bloch functions $|\psi_{n,\mathbf{k}}\rangle = e^{i\mathbf{k}\cdot\mathbf{r}}|u_{n\mathbf{k}}\rangle$ with a band index n , we also define a complex matrix w for a time-reversal operator Θ as

$$w_{m,n}(\mathbf{k}) = \langle u_{m,-\mathbf{k}} | \Theta | u_{n,\mathbf{k}} \rangle, \quad (2.15)$$

where m and n are band indices for occupied bands. Then, ν is defined as [33]

$$(-1)^\nu = \prod_{n_j=0,1} \delta_{n_1 n_2}, \quad (2.16)$$

$$\delta_i = \frac{\sqrt{\det[w(\mathbf{\Gamma}_i)]}}{\text{Pf}[w(\mathbf{\Gamma}_i)]}. \quad (2.17)$$

Here, δ_i is equal to ± 1 , since $\text{Pf}[w(\mathbf{\Gamma}_i)]^2 = \det[w(\mathbf{\Gamma}_i)]$. Therefore, we obtain

$$\nu = 0, 1 \pmod{2}. \quad (2.18)$$

If $\nu = 1(0)$, the system is in the 2DTI (NI) phase. The 2DTI has edge states protected topologically. The edge states are degenerate at the TRIM because of Kramers theorem due to the time-reversal symmetry. The bands of the edge states cross the Fermi energy between the two edge TRIM an odd number of times, as shown in Fig. 2.3 (a). On the other hand, the edge bands in the trivial insulator cross the Fermi energy between the two edge TRIM an even number

of times including zero. In the \mathbb{Z}_2 topological insulator, the gapless edge states are called helical edge states.

Furthermore, the \mathbb{Z}_2 topological number can be defined in three-dimensional systems [28, 32, 34, 35]. In three-dimensional topological insulators (3DTIs), we have four topological invariants taking values zero or one:

$$\nu_0; (\nu_1 \nu_2 \nu_3). \quad (2.19)$$

The definition of the topological numbers is given in the same way as in the 2DTI. In three-dimensional systems, the TRIM are

$$\mathbf{\Gamma}_{i=(n_1, n_2, n_3)} = \frac{1}{2}(n_1 \mathbf{G}_1 + n_2 \mathbf{G}_2 + n_3 \mathbf{G}_3), \quad (n_j = 0, 1), \quad (2.20)$$

where $\mathbf{G}_{1,2,3}$ are the three-dimensional reciprocal lattice vectors. By introducing $w(\mathbf{k})$ similarly as in Eq. (2.15), we can define the four topological invariants as

$$(-1)^{\nu_0} = \prod_{n_j=0,1} \delta_{n_1 n_2 n_3}, \quad (2.21)$$

$$(-1)^{\nu_{i=1,2,3}} = \prod_{n_j(\neq i)=0,1; n_i=1} \delta_{n_1 n_2 n_3}. \quad (2.22)$$

These topological invariants can also be interpreted as an obstruction to a choice of a gauge for the states in the same Kramers pair, which is analogous to the Chern number [33, 36]. We can know the information about the surface states from the \mathbb{Z}_2 topological numbers. $\nu_{i=1,2,3}$ correspond to the two-dimensional topological invariants in the three-dimensional system. For example, ν_1 characterizes band topology on the plane which contains four TRIM $\mathbf{\Gamma}_{(n_1=1, n_2, n_3)} = \frac{1}{2}(\mathbf{G}_1 + n_2 \mathbf{G}_2 + n_3 \mathbf{G}_3)$. Insulators with $\nu_0 = 1$ are called strong topological insulators (strong TIs). The strong TIs necessarily have an odd number of surface Dirac modes. Meanwhile, when ν_0 is zero and some of $\nu_{i=1,2,3}$ are nonzero, the insulators are called weak topological insulators (weak TIs). In the next subsection, the strong TIs and the weak TIs are explained in detail.

When the system has inversion symmetry, the expression of \mathbb{Z}_2 topological numbers are simplified considerably. The index δ_i is rewritten as [28]

$$\delta_i = \prod_{m=1} \xi_{2m}(\mathbf{\Gamma}_i), \quad (2.23)$$

where $\xi_{2m}(\mathbf{\Gamma}_i)$ is the parity eigenvalue of the wave function with the band index $2m$ at $\mathbf{k} = \mathbf{\Gamma}_i$ below the Fermi energy. The value $2m$ comes from Kramers degeneracy due to presence of the time-reversal and the inversion symmetries. Therefore, the \mathbb{Z}_2 topological number ν_0 is obtained from

$$(-1)^{\nu_0} = \prod_{i=1}^8 \prod_{m=1} \xi_{2m}(\mathbf{\Gamma}_i). \quad (2.24)$$

Thus, ν_0 changes typically by one in the inversion-symmetric system when the energy gap closes and reopens at the TRIM $\mathbf{\Gamma}_i$ [Fig. 2.3(b)].

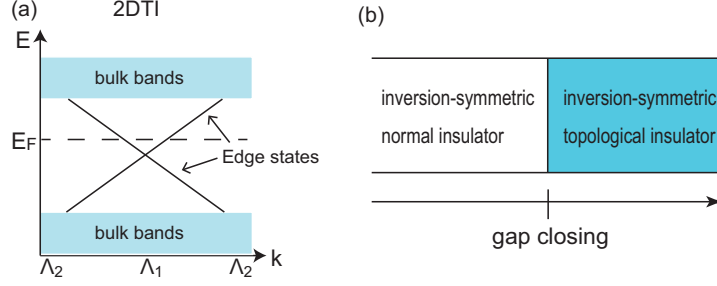


Figure 2.3: (a) Dispersion of edge states in the 2DTI. E_F and $\Lambda_{1,2}$ represent the Fermi energy and the edge TRIM, respectively. (b) Topological phase transition in the inversion-symmetric insulator. The horizontal axis is a parameter which drives the phase transition.

2.1.4 Strong TIs and weak TIs

To understand the difference between the strong TIs and the weak TIs, we clarify the meaning of the indices δ_i . Firstly, we consider the edge states of the 2DTIs. For the edge considered, there are two edge TRIM $\Lambda_{a=1,2}$. Among the four bulk TRIM $\Gamma_{i=1,2,3,4}$, let Γ_{a1} and Γ_{a2} be the bulk TRIM which are projected onto Λ_a . Then, we have a relationship between the two TRIM Γ_{a1} and Γ_{a2} given by

$$\Gamma_{a1} - \Gamma_{a2} = \frac{\mathbf{G}}{2}, \quad (2.25)$$

where \mathbf{G} is the reciprocal lattice vector normal to the edge. Here, we define new indices

$$\pi_a = \delta_{a1}\delta_{a2} = \pm 1, \quad (2.26)$$

where δ_{a1} and δ_{a2} are the indices corresponding to Γ_{a1} and Γ_{a2} , respectively. Thus, $\pi_a = \pm 1$ is determined for each edge TRIM Λ_a . We consider the product of the two indices π_1 and π_2 :

$$\pi_1\pi_2 = \pm 1. \quad (2.27)$$

Because $(-1)^\nu = \pi_1\pi_2$, where ν is the topological invariant in Eq. (2.16), the edge states intersect the Fermi energy between Λ_1 and Λ_2 an odd number of times when $\pi_1\pi_2 = -1$, and an even number of times when $\pi_1\pi_2 = 1$. Therefore, we can extract information on the edge Fermi surface by the indices δ_i .

The above idea can be generalized to three-dimensional insulators [34]. Then, we have eight indices δ_i for the bulk TRIM and four indices $\pi_{a=1,2,3,4}$ for the surface TRIM. Similarly to the 2DTI, an odd (even) number of the surface Fermi surface exists between Λ_a and Λ_b when $\pi_a\pi_b = -1(+1)$, as shown in Fig. 2.4. Therefore, if $\nu_0 = 1$, at least one Fermi surface exists in any surfaces since the topological number ν_0 is equal to the product of all the indices π_a . In other words, any surfaces of the strong TI necessarily have gapless states. In contrast,

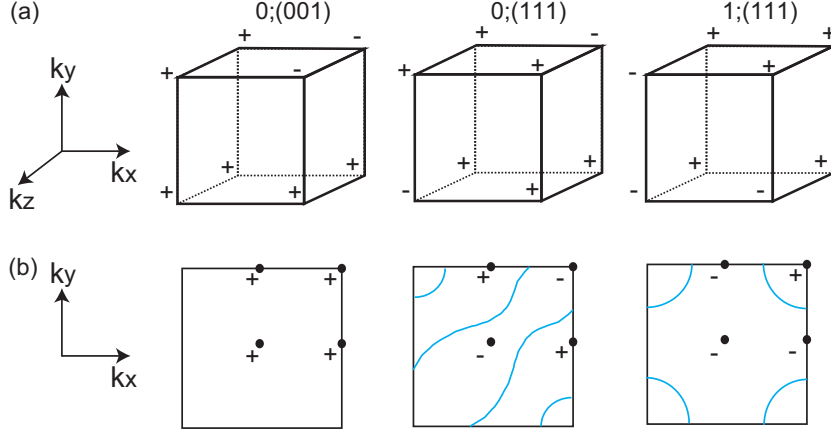


Figure 2.4: Examples of the indices δ_a , π_a and the surface Fermi surfaces on the (001) surface in the TIs. (a) depicts the values $\delta_a = \pm 1$ at the eight TRIM Γ_a in the TIs with $\nu_0; (\nu_1 \nu_2 \nu_3)$. (b) visualizes relationships between the surface Fermi surfaces and $\pi(\Lambda_a) = \pm 1$ at the four surface TRIM Λ_a . The blue lines in the surface BZ represent the surface Fermi surfaces.

the surface bands in the weak TI can be gapped out, regardless of the values of $\nu_{1,2,3}$.

We note that the gapless surface states in the weak TI are fragile against time-reversal symmetric perturbations while they are robust in the strong TI. Let us suppose that we have the two surface Fermi surfaces between the TRIM in the weak TI. Because we can add perturbations making the two surface modes hybridize without violating the Kramers theorem, we can open a gap in the surface states. On the other hand, we consider the strong TI with one gapless surface mode between the surface TRIM. The surface states must remain gapless against the perturbations, since Kramers degeneracy prohibits opening of the gap for the surface states. As a result, whether the gapless surface states are robust against perturbations depends on the number of the surface Fermi surfaces between the surface TRIM, which is determined by whether the system is the strong TI or the weak TI.

2.1.5 Surface fermion parity

The products of δ_i in Eq. (2.23) help us know if surface states exist between two TRIM in the TIs. Furthermore, δ_i determines the parity of the surface fermion number $N(\Lambda_a)$ in the inversion-symmetric TI [37]. $N(\mathbf{q})$ represents excess charges near the surface at wavevector \mathbf{q} in the surface BZ, and takes an integer value when the inversion symmetry is present. When $N(\mathbf{q}) = 0$, the wavevector at \mathbf{q} is outside the surface Fermi surface. Meanwhile, if $N(\mathbf{q})$ is positive (negative), the wavevector \mathbf{q} is inside the $N(\mathbf{q})$ electron (hole) pockets.

The parity of $N(\mathbf{\Lambda}_a)$ at the surface TRIM $\mathbf{\Lambda}_a$ is given by [37]

$$(-1)^{N(\mathbf{\Lambda}_a)} = (-1)^{n_b} \delta_{a1} \delta_{a2} \equiv \tilde{\pi}_a, \quad (2.28)$$

where n_b is a half of the number of the occupied bands. Thus, $\mathbf{\Lambda}_a$ is necessarily inside the surface Fermi surface when $\tilde{\pi}_a = -1$. From Eq. (2.23), $\tilde{\pi}_a$ is rewritten as

$$\tilde{\pi}_a = (-1)^{n_b} \prod_{m=1} \xi_{2m}(\mathbf{\Gamma}_{a1}) \xi_{2m}(\mathbf{\Gamma}_{a2}). \quad (2.29)$$

Therefore, $\tilde{\pi}_a$ depends on the choice of an inversion center $\mathbf{r} = \mathbf{c}$ through $\xi_{2m}(\mathbf{\Gamma}_a)$. This implies that the surface band structures depend on how the crystal is terminated. General three-dimensional crystals have eight different inversion centers. Two different inversion centers \mathbf{c} and \mathbf{c}' are related by a half of the Bravais lattice vector \mathbf{R} . The relationship is given by $\mathbf{c}' = \mathbf{c} + \frac{\mathbf{R}}{2}$. In the following, when we take the inversion center at $\mathbf{r} = \mathbf{c}'$ instead of $\mathbf{r} = \mathbf{c}$, we add the superscript $'$ to the parity eigenvalues and the indices at TRIM $\mathbf{\Gamma}_i$. Then, we obtain $\xi'_{2m}(\mathbf{\Gamma}_i) = \xi_{2m}(\mathbf{\Gamma}_i) e^{i\mathbf{\Gamma}_i \cdot \mathbf{R}}$, which leads to

$$\delta'_i = \delta_i e^{in_b \mathbf{\Gamma}_i \cdot \mathbf{R}}. \quad (2.30)$$

Thus, the correspondent $\tilde{\pi}_a$ and $\tilde{\pi}'_a$ are related by

$$\tilde{\pi}'_a = \tilde{\pi}_a \exp[in_b(\mathbf{\Gamma}_{a1} - \mathbf{\Gamma}_{a2}) \cdot \mathbf{R}]. \quad (2.31)$$

Hence, depending on which of the points \mathbf{c} or \mathbf{c}' is located in the plane of the surface, the surface bands changes if $\tilde{\pi}_a = -\tilde{\pi}'_a$ [Fig. 2.5]. As a result, whether the surface TRIM is inside or outside the surface Fermi surface depends on the surface termination.

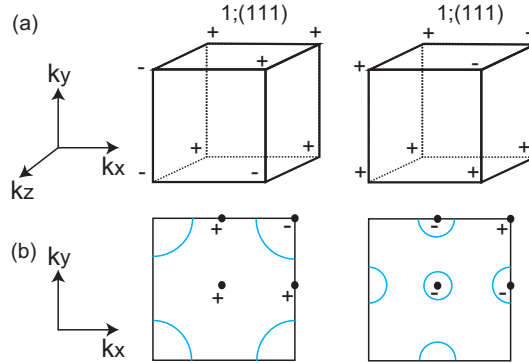


Figure 2.5: Dependence of the surface Fermi surfaces on the surface termination in the TI with $\nu_0; (\nu_1 \nu_2 \nu_3) = 1; (111)$ and $n_b = 1$. The inversion center taken in the right figure differs from that in the left figure by a half of the Bravais lattice parallel to the z direction. (a) depicts $\delta_a = \pm 1$ in the bulk BZ. (b) shows $\tilde{\pi}_a = \pm 1$ and the surface band structures. The TRIM with $\tilde{\pi}_a = -1$ are inside the surface Fermi surface.

2.2 Topological semimetals

2.2.1 Weyl semimetal

Recent works have revealed topological properties in nodal semimetals in addition to topological insulators. Semimetals with nodes protected topologically are named topological semimetals. One of the topological semimetals is a Weyl semimetal (WSM) [9]. WSMs have point nodes formed accidentally by two non-degenerate bands, and these point nodes are called Weyl nodes. In the WSM, the conduction and the valence bands form three-dimensional nondegenerate Dirac cones around the Weyl nodes. In the simplest case, the Hamiltonian around the Weyl node is described as

$$H = v\mathbf{k} \cdot \boldsymbol{\sigma}, \quad (2.32)$$

where $\boldsymbol{\sigma} = (\sigma_x, \sigma_y, \sigma_z)$ are Pauli matrices indicating the conduction and the valence bands. Here, \mathbf{k} is a wavevector measured from the position of the Weyl nodes. In this section, we review topological properties of the WSM from Eq. (2.32).

We study necessary conditions for realization of the WSM before discussion about its properties. Since the Weyl nodes consist of the two nondegenerate bands, the system should break either time-reversal or inversion symmetry. In this system, energy bands are generally nondegenerate because Kramers degeneracy is absent. Thus, we can describe the conduction and the valence bands near the Fermi energy as a 2×2 Hamiltonian given by

$$H_{eff}(\mathbf{k}) = a_0(\mathbf{k})\mathbf{1}_{2 \times 2} + a_x(\mathbf{k})\sigma_x + a_y(\mathbf{k})\sigma_y + a_z(\mathbf{k})\sigma_z. \quad (2.33)$$

where $a_{0,x,y,z}(\mathbf{k})$ are real functions. In the three-dimensional WSMs, $a_x = a_y = a_z = 0$ at the Weyl nodes. Namely, there are three conditions for realization of the Weyl nodes. In three-dimensional systems, the solutions can exist because we have three variables (k_x, k_y, k_z) . Therefore, the WSMs are generally realizable in the three-dimensional systems but not in two- and one-dimensional systems [8, 38], unless the system has some additional symmetries which allow existence of Weyl nodes.

Noncentrosymmetric WSMs were discovered in the TaAs family (TaAs, TaP, NbAs, and NbP) by several groups performing angle-resolved photoemission spectroscopy [39–44], after the theoretical predictions [45, 46]. The TaAs family is nonmagnetic, and belongs to the nonsymmorphic space group No.109. TaAs has 24 Weyl nodes in the bulk by the strong spin-orbit interaction leading to the band touching. On the other hand, no experimental research has been reported for direct observation of Weyl nodes in magnetic WSMs yet. The possible candidates are pyrochlore iridates $A_2\text{Ir}_2\text{O}_7$ ($A=\text{Y, Eu, Sm, Nd}$) [9, 47], HgCr_2Se_4 [48], Co-based Heusler compounds XCo_2Sn ($\text{X}=\text{Zr, Nb, V}$) [49], Mn_3Ge , Mn_3Sn [50] and so on. Recent experimental measurements show that Mn_3Sn exhibits a large anomalous Nernst effect [51] and positive magnetoconductance [52], which are expected to originate from topological properties of the Weyl nodes.

2.2.2 Stability of the Weyl nodes

The intriguing feature of the Weyl nodes is stability against small perturbations. This stability can be intuitively understood from a simple argument using Pauli matrices. For example, we add a term $m\sigma_z$ to Eq. (2.32) as a perturbation. Then, we obtain

$$H = k_x\sigma_x + k_y\sigma_y + (k_z + m)\sigma_z, \quad (2.34)$$

where we put $v = 1$ for simplicity. The energy eigenvalues are

$$E = \pm \sqrt{k_x^2 + k_y^2 + (k_z + m)^2}. \quad (2.35)$$

Because the bands are gapless at $(k_x, k_y, k_z) = (0, 0, -m)$, we can see that the m term does not open the gap. As discussed in the previous subsection, to obtain Weyl nodes, we need three tunable parameters to make the coefficients of three Pauli matrices $\sigma_{x,y,z}$ zero simultaneously. Now, we have the three components of the wavevector, k_x , k_y , and k_z . Therefore, even if small perturbations are added to the Weyl Hamiltonian, the Weyl node still persists as can be seen in Eq. (2.34). Hence, because the perturbations only shift the position of the Weyl node, they are stable as long as wavevectors are well-defined by translational symmetry.

The stability can be also understood from topological aspects. To see this, we consider Berry connection $\mathbf{A}_\alpha(\mathbf{k})$ and Berry curvature $\mathbf{\Omega}_\alpha(\mathbf{k})$ for the α th band given by [8, 23, 53]

$$\mathbf{A}_\alpha(\mathbf{k}) = i \langle u_{\alpha,\mathbf{k}} | \nabla_{\mathbf{k}} | u_{\alpha,\mathbf{k}} \rangle, \quad \mathbf{\Omega}_\alpha(\mathbf{k}) = \nabla_{\mathbf{k}} \times \mathbf{A}_\alpha(\mathbf{k}). \quad (2.36)$$

We also define the monopole density as

$$\rho_\alpha(\mathbf{k}) = \frac{1}{2\pi} \nabla_{\mathbf{k}} \cdot \mathbf{\Omega}_\alpha(\mathbf{k}) = \frac{1}{2\pi} \nabla_{\mathbf{k}} \cdot (\nabla_{\mathbf{k}} \times \mathbf{A}_\alpha). \quad (2.37)$$

If the Berry curvature $\mathbf{\Omega}_\alpha$ is well-defined in the whole BZ, $\rho_\alpha(\mathbf{k}) = 0$ from Eq. (2.37).

However, if the energy bands have Weyl nodes, $\rho_\alpha(\mathbf{k})$ does not vanish. Topological properties of the Weyl node can be found from the nonzero monopole density. We use Eq. (2.32) to see $\rho_\alpha(\mathbf{k}) \neq 0$. The Berry curvature is given by

$$\mathbf{\Omega}_\pm(\mathbf{k}) = \mp \text{sgn}(v) \frac{\mathbf{k}}{2k^3} = \pm \frac{\text{sgn}(v)}{2} \nabla_{\mathbf{k}} \left(\frac{1}{k} \right), \quad (2.38)$$

where $+$ and $-$ represent the upper and the lower bands, respectively. Since $\nabla_{\mathbf{k}}^2(1/k) = -4\pi\delta(\mathbf{k})$, we obtain

$$\rho_\pm(\mathbf{k}) = \mp \text{sgn}(v) \delta(\mathbf{k}). \quad (2.39)$$

Therefore, the Weyl node gives the nonzero monopole density. In fact, $\rho_\alpha(\mathbf{k})$ is related to a topological invariant. Below, we show that $\text{sgn}(v)$ in Eq. (2.39) is a Chern number q for the lower band on a spherical surface S^2 enclosing the Weyl

node. If we integrate the Berry curvature on S^2 by using the Gauss's theorem, the Chern number for the lower band is calculated as

$$q = \frac{1}{2\pi} \int_{S^2} \boldsymbol{\Omega}_-(\mathbf{k}) \cdot d\mathbf{S} = \int \rho_-(\mathbf{k}) d^3k = \text{sgn}(v). \quad (2.40)$$

This integer q is also called a monopole charge. Thus, the Weyl node is characterized by the monopole charge corresponding to the Chern number. This means that the Weyl node is stable because q is unchanged by small perturbations. In general, a Weyl node with $q > 0$ ($q < 0$) is called a monopole (an antimonopole).

As a general case, when an anisotropic Weyl node lies at $\mathbf{k} = \mathbf{k}_0$, we can obtain the effective Hamiltonian by expanding Eq. (2.33) to the first order of the wavevector. The Hamiltonian is

$$H_{eff}(\mathbf{k}) = \sum_{m,i=1}^3 \left(\frac{\partial a_m}{\partial k_i} \right)_{\mathbf{k}=\mathbf{k}_0} q_i \sigma_m, \quad (2.41)$$

where $\mathbf{q} = \mathbf{k} - \mathbf{k}_0$. We have ignored the a_0 term because this term only shifts the energy. In this case, we get $q = \text{sgn} \left[\det \left(\left(\frac{\partial a_m}{\partial k_i} \right)_{\mathbf{k}=\mathbf{k}_0} \right) \right]$ [8, 9, 53].

Moreover, we study implications of time-reversal and inversion symmetries in the WSM phase [8, 9, 17]. Let us denote time-reversal and inversion operations as T and P , respectively. The two symmetries relate electronic states at \mathbf{k} and $-\mathbf{k}$. Namely, $|u_{\alpha_T, -\mathbf{k}}\rangle = T |u_{\alpha, \mathbf{k}}\rangle$ and $|u_{\alpha_I, -\mathbf{k}}\rangle = P |u_{\alpha, \mathbf{k}}\rangle$ up to a phase, where $\alpha_T(\alpha_I)$ is a band index related with the α th band by the time-reversal (inversion) symmetries. Thus, these two symmetries restrict the Berry curvature and the monopole density. The time-reversal symmetry leads to

$$\boldsymbol{\Omega}_\alpha(\mathbf{k}) = -\boldsymbol{\Omega}_{\alpha_T}(-\mathbf{k}), \quad \rho_\alpha(\mathbf{k}) = \rho_{\alpha_T}(-\mathbf{k}), \quad (2.42)$$

while the inversion symmetry leads to

$$\boldsymbol{\Omega}_\alpha(\mathbf{k}) = \boldsymbol{\Omega}_{\alpha_I}(-\mathbf{k}), \quad \rho_\alpha(\mathbf{k}) = -\rho_{\alpha_I}(-\mathbf{k}). \quad (2.43)$$

As a result, monopoles are distributed symmetrically (asymmetrically) with respect to the origin $\mathbf{k} = 0$ in the system with time-reversal (inversion) symmetry. Thus, if both time-reversal and inversion symmetries are present, the monopole density is zero everywhere in the BZ. Hence, we can understand from the topological argument that Weyl nodes are absent in the system with time-reversal and inversion symmetries.

Finally, we discuss gapless points when systems have both time-reversal and inversion symmetries. Then, since all the states are doubly degenerate by the Kramers theorem, the gapless points are typically fourfold-degenerate. The gapless points are called Dirac nodes, and the phase with the Dirac nodes near the Fermi energy is named a Dirac semimetal (DSM). The Dirac nodes are generally unstable because the monopole density is zero. Therefore, in order to make the Dirac nodes stable, the system requires additional crystalline symmetries [54–57]. Nonetheless, DSM phases were observed experimentally in Na_3Bi [58–60] and Cd_3As_2 [61], where the stability of the Dirac nodes are guaranteed by rotational symmetries.

2.2.3 Fermi arc

Another topological property of the WSM is existence of surface states protected topologically [9, 62, 63]. The surface states form arcs at the Fermi energy in the surface BZ, which are called Fermi arcs. In this subsection, we show that the Fermi arc connects between a monopole and an antimonopole (Fig. 2.6). To study the topological surface states, we consider a WSM with Weyl nodes on the k_z axis. When we fix k_z as a parameter, the Hamiltonian of the WSM is written as

$$H(\mathbf{k}) = H(k_x, k_y)_{[k_z]}. \quad (2.44)$$

This Hamiltonian can be regarded as that for a two-dimensional system. Then, because the energy bands are gapped except at the Weyl nodes, the Chern number can be defined on the two-dimensional plane (k_x, k_y) at each k_z like a two-dimensional insulator. The Chern number is expressed as

$$n(k_z) = \frac{1}{2\pi} \int dk_y dk_x \Omega_-^z(k_x, k_y)_{[k_z]}, \quad (2.45)$$

where this integral is performed over the two-dimensional BZ with fixed k_z . Since the Chern number depends on k_z , the surface states appear on the plane at k_z with the nonzero Chern number, if the WSM is cut parallel to the z axis.

Next, we see that $n(k_z)$ changes at points where the Weyl nodes lie. Let us assume that the Weyl node is located at $\mathbf{k}_0 = (0, 0, k_W)$, and that the Hamiltonian around the Weyl node is described by

$$H(\mathbf{k}) = v\mathbf{q} \cdot \boldsymbol{\sigma}, \quad (2.46)$$

where $\mathbf{q} = \mathbf{k} - \mathbf{k}_0$. $\text{sgn}(v)$ determines if the Weyl node is a monopole or an antimonopole. To see the change of $n(k_z)$, we calculate difference of the Chern number between $q_z > 0$ and $q_z < 0$. The difference is given by

$$\begin{aligned} n(q_z > 0) - n(q_z < 0) &= \frac{1}{2\pi} \int dk_y dk_x \Omega_-^z_{[q_z > 0]} - \frac{1}{2\pi} \int dk_y dk_x \Omega_-^z_{[q_z < 0]} \\ &= \text{sgn}(v). \end{aligned} \quad (2.47)$$

Therefore, if the energy bands have a monopole (an antimonopole) at $\mathbf{k}_0 = (0, 0, k_W)$, $n(k_z)$ changes by $+1(-1)$ between $k_z > k_W$ and $k_z < k_W$. This change is similar to that of Eq. (2.11) by identifying k_z with m . Thus, the WSM can be regarded as a stack of Chern insulators in \mathbf{k} space.

From Eq. (2.47), we note that a monopole and an antimonopole necessarily emerge in pairs. Since $n(k_z)$ is periodic because of translational symmetry in the z direction, it is impossible that the Brillouin zone has only one monopole or one antimonopole. In other words, the monopole and the antimonopole are always created or annihilated in pairs when the Weyl nodes appear or vanish. This result is known as Nielsen-Ninomiya theorem [64, 65]. Indeed, if the monopole and the antimonopole are located at the same point \mathbf{k}_0 , the Weyl nodes become

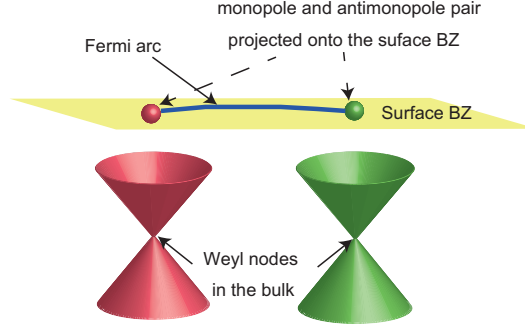


Figure 2.6: A surface Fermi arc connecting between the monopole-antimonopole pair. The red and green points indicate the monopole and the antimonopole, respectively.

unstable because $\rho_-(\mathbf{k}_0) = 0$. Hence, it is shown that the Fermi arc connects the monopole and the antimonopole because they necessarily appear in pairs.

Furthermore, it is significant that the minimal number of Weyl nodes are different between the WSMs with time-reversal and those with inversion symmetry. Time-reversal invariant WSMs have Weyl nodes with the same monopole charge at \mathbf{k} and $-\mathbf{k}$ from Eq. (2.42). However, if the energy bands have only the two Weyl nodes, it is inconsistent with Nielsen-Ninomiya theorem. Therefore, the time-reversal invariant WSMs have at least four Weyl nodes. Meanwhile, in inversion-symmetric WSMs, The Nielsen-Ninomiya theorem is automatically satisfied even if the number of the Weyl nodes is two, since a monopole and an antimonopole are located at \mathbf{k} and $-\mathbf{k}$ from Eq. (2.43), respectively.

2.2.4 Phase diagram for the time-reversal invariant WSM

An ordinary Chern number offers topological classification of mappings from the two-dimensional BZ to the Bloch Hamiltonian. However, the Chern number necessarily becomes zero when time-reversal symmetry is present. Nevertheless, Moore and Balents found a nontrivial \mathbb{Z}_2 topological invariant by extending the notion of the Chern number in time-reversal invariant systems by considering a map from a half of the two-dimensional BZ to the Bloch Hamiltonian if the inversion symmetry is broken [32]. The topological invariant is equivalent to the \mathbb{Z}_2 topological invariant ν in Eq. (2.16). Thus, a change of ν accompanies a gap closing in a half of the two-dimensional BZ.

We can apply the new Chern number to three-dimensional systems without inversion symmetry by slicing the three-dimensional BZ [32]. Then, while the gap closing may change some of the topological invariants $\nu_0; (\nu_1\nu_2\nu_3)$, Weyl nodes are generally created in pairs [8, 53]. Thus, the system cannot move from the NI phase to the 3DTI phase directly as shown in Fig. 2.7 (a). Hereafter, we discuss how the system enters the 3DTI phase via the WSM phase.

To elucidate the phase transition, we introduce a tunable parameter m which determines the phases. We assume that the system is in a trivial insulator phase within $m < m_1$, and that pair creation happens at $m = m_1$. When we increase the parameter $m > m_1$, the emergent Weyl nodes move in the three-dimensional BZ while preserving the time-reversal symmetry. We also assume that the system becomes gapped again by pair annihilation of the Weyl nodes at $m = m_2$. Here, to see change of ν_0 , we consider a plane containing four TRIM $\Gamma_{(n_1=1, n_2, n_3)} = \frac{1}{2}(\mathbf{G}_1 + n_2\mathbf{G}_2 + n_3\mathbf{G}_3)$ in the first BZ, which we dub S_1 . From the above argument by Moore and Balents [32], if the gap closes on a half of the plane S_1 once, ν_0 and ν_1 change by one modulo two. Thus, the realized phase within $m > m_2$ depends on the number of the times when the Weyl nodes pass through the half of the plane S_1 . In other words, trajectories of the Weyl nodes determine whether the gapped phase within $m > m_2$ is topological or not. Therefore, it is found that the gapped phase is a strong TI when the trajectories of the Weyl nodes intersect with the half of S_1 an odd number of times [8, 53]. As a result, $(2N + 1)$ intersections with integer N appears between the trajectory of the Weyl nodes and the half of S_1 in the NI-WSM-3DTI phase transition, as illustrated in Fig. 2.7 (b). In contrast, if the trajectories intersect with the half of S_1 an even number of times, the phase becomes trivial again for $m > m_2$ [8, 53].

We can use this general phase diagram in Fig. 2.7(a) to predict new materials of WSMs. The NI-WSM-TI phase transition is expected to happen in BiTeI under pressure from first-principle calculations [66]. Although BiTeI had been proposed to become a noncentrosymmetric 3DTI directly from a NI by increasing pressure at first [67, 68], it was shown later that BiTeI becomes a WSM before it enters the 3DTI phase [66].

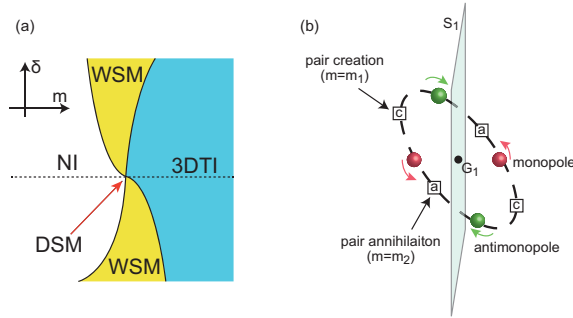


Figure 2.7: (a) General phase diagram of the NI-WSM-3DTI phase transition. δ is an inversion-breaking term, and m is the tunable parameter. If $\delta = 0$, the WSM phase does not appear. (b) An example of the trajectory of the Weyl nodes in the NI-WSM-3DTI phase transition. The red (green) points represent monopoles (antimonopoles). When m changes from m_1 to m_2 , the trajectory intersects with the plane S_1 $2(2N + 1)$ times.

2.2.5 Gap closing in noncentrosymmetric materials

A gap closing is essential for realization of WSMs. Although a crystal belongs to one of the space groups, we have not taken into account the crystal symmetries in the discussion so far. Therefore, we need to clarify effects of the crystal symmetries in the gap closing. If the gap closes at $\mathbf{k} = \mathbf{k}_0$, the behavior can be described by symmetries which leave \mathbf{k}_0 invariant [69]. In time-reversal invariant systems, the behaviors are completely elucidated in all the 138 space groups without inversion symmetry in Ref. [69]. In this subsection, we give some parts of the results.

Here, let us explain the setup to analyze the gap closing. We use the two-band effective Hamiltonian in Eq. (2.33):

$$H_{eff}(\mathbf{q}, m) = a_0(\mathbf{q}, m)\mathbf{1}_{2 \times 2} + a_1(\mathbf{q}, m)\sigma_2 + a_2(\mathbf{q}, m)\sigma_2 + a_3(\mathbf{q}, m)\sigma_3. \quad (2.48)$$

We added a tunable parameter m governing the gap closing to Eq. (2.33). To study the gap closing, we assume that the gap is open within $m < m_0$, and that the gap closes at $\mathbf{q} = 0$ and $m = m_0$. We can determine band evolutions within $m > m_0$ by the number of the parameters necessary for the gap closing. In three-dimensional systems, a topological phase with a stable point, line and surface generally emerges when $m > m_0$, provided that difference between the number of variables and conditions for the gap closing is 1, 2 and 3, respectively.

When \mathbf{k}_0 is invariant under a certain unitary symmetry $g : \mathbf{k} \rightarrow D(g)\mathbf{k}$, the energy eigenstates at \mathbf{k}_0 are also eigenstates of g . We denote the eigenvalue of the conduction (valence) band as $R_c(R_v)$. Then, g is represented by

$$U_g = \begin{pmatrix} R_c & 0 \\ 0 & R_v \end{pmatrix}, \quad (2.49)$$

which yields a constraint given by

$$U_g H_{eff}(\mathbf{q}) U_g^{-1} = H_{eff}(D(g)\mathbf{q}). \quad (2.50)$$

Under this constraint, we must investigate how the gap closes at $\mathbf{k} = \mathbf{k}_0$. In this subsection, we exemplify the two cases where \mathbf{k}_0 is invariant under (I) rotational and (II) mirror symmetry according to Ref. [69]. Each case is further classified into two cases, (i) $R_c = R_v$ and (ii) $R_c \neq R_v$. In the following, we write U_g as g for simplicity. The results are listed in Tab. 2.1.

g	$R_c = R_v$	$R_c \neq R_v$
rotational symmetry	-	Weyl node
mirror symmetry	Weyl node	line node

Table 2.1: Types of the emergent nodes depending on the eigenvalues of the two bands at the symmetry points. On the rotational axis, the gap does not close if the conduction and the valence bands have the same rotational eigenvalues.

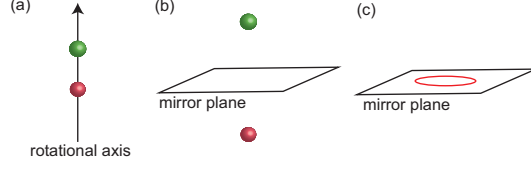


Figure 2.8: (a) and (b) show the Weyl nodes emerging from the pair creation on the rotational axis and the mirror plane, respectively. (c) shows the line node due to the gap closing between the two states with the opposite mirror eigenvalues.

(I) Rotational symmetries

When the gap closes on a rotational axis, Weyl nodes are created [Fig. 2.8(a)]. However, the gap closing can happen only when the conduction and the valence bands have different eigenvalues of the rotational operation. The emergent Weyl nodes move along the rotational axis within $m > m_0$. To see the behavior, we consider the gap closing on the twofold (C_2) rotational axis parallel to the z direction for example.

(i) Suppose that the two bands have the same C_2 eigenvalues, i.e., $C_2 = \pm i\sigma_0$. The effective Hamiltonian satisfies $H_{eff}(q_x, q_y, q_z, m) = H_{eff}(-q_x, -q_y, q_z, m)$. Because this condition does not impose any constraints on the effective Hamiltonian at $\mathbf{q} = 0$, $a_x(\mathbf{q} = 0, m) = a_y(\mathbf{q} = 0, m) = a_z(\mathbf{q} = 0, m) = 0$ cannot be satisfied simultaneously when we change the single parameter m . Therefore, the gap does not close between the two states with the same C_2 eigenvalues.

(ii) Next, suppose that the two bands have opposite C_2 eigenvalues, i.e., $C_2 = \pm i\sigma_z$. Then, we obtain $\sigma_z H_{eff}(q_x, q_y, q_z, m) \sigma_z = H_{eff}(-q_x, -q_y, q_z, m)$. This constraint leads to

$$H_{eff}(0, 0, q_z, m) = a_0(0, 0, q_z, m)\mathbf{1}_{2 \times 2} + a_z(0, 0, q_z, m)\sigma_z. \quad (2.51)$$

Since we have the two variables (q_z, m) , $a_z(0, 0, q_z, m) = 0$ can have a solution $q_z = b_z(m)$ by the assumption $a_z(0, m_0) = 0$. As a result, pair creation of Weyl nodes occurs at $(q_z, m) = (0, m_0)$, and the emergent Weyl nodes move along the C_2 axis.

Here, to know band structures at the pair creation, we expand $a_z(q_z, m)$ near $(q_z, m) = (0, m_0)$ to the first order: $a_z(q_z, m) = v_z q_z + A(m - m_0)$ where A is a constant. However, this equation is inconsistent with the gap within $m < m_0$. Thus, because the first order of q_z needs to vanish, the expansion of $a_z(q_z, m)$ is given by

$$a_z(q_z, m) = \gamma q_z^2 + A(m - m_0), \quad (2.52)$$

where γ and A are constants with opposite signs. Hence, the bands are quadratic in the direction along which the Weyl nodes move as a change of m . Indeed, the quadratic dispersion along the direction of the motion of Weyl nodes is universal in generic pair creations [53].

Among materials, tellurium (Te) is theoretically predicted to realize the gap closing on the rotational axes under high pressure [70]. Te is a semiconductor lacking an inversion center. There are two kinds of crystals of Te, and the space groups are No.152 and No.154. When the pressure reaches 2.17 GPa, the gap closes on four K - H lines which are the threefold screw axes. Eight Weyl nodes appear after the pair creations, and then they start to move along the threefold screw axes.

(II) Mirror symmetry

There are two types of band evolution after the gap closing on the mirror plane in the three-dimensional systems, as shown in Fig. 2.8 (b) and (c). The behavior depends on the mirror eigenvalues of the two bands. To see this, we assume that the mirror plane is the xy plane.

(i) Firstly, suppose that the two bands have the same mirror eigenvalues, i.e., $M = \pm i\sigma_0$. Thus, we obtain $H_{eff}(q_x, q_y, -q_z, m) = H_{eff}(q_x, q_y, q_z, m)$. Because this equation is satisfied automatically when $q_z = 0$, this condition does not affect the gap closing on the mirror plane. Therefore, after the gap closes between the two states with the same mirror eigenvalues at $m = m_0$, Weyl nodes appear symmetrically with respect to the mirror plane.

This type of the gap closing is expected to occur in LuSi under pressure [69]. LuSi belongs to the noncentrosymmetric space group No.174, and has mirror symmetry. If the pressure is applied to LuSi, the band gap closes at six points on the mirror plane. Then, LuSi becomes a WSM with twelve Weyl nodes.

(ii) Secondly, suppose that the two bands have opposite mirror eigenvalues, i.e., $M = \pm i\sigma_z$. Then, the effective Hamiltonian satisfies

$$H_{eff}(q_x, q_y, 0, m) = a_0(q_x, q_y, 0, m)\mathbf{1}_{2 \times 2} + a_z(q_x, q_y, 0, m)\sigma_z. \quad (2.53)$$

In this case, M reduces the number of the conditions for the gap closing by one, while we have three variables (q_x, q_y, m) on the mirror plane. Hence, a line node appears on the mirror plane after the gap closing.

As a candidate of the nodal-line semimetal, HfS is proposed [69]. The space group is No.187 which contains mirror symmetry but not inversion symmetry. When the S atoms are partially substituted by Se, the nodal line shrinks on the mirror plane. The nodal line also disappears if we apply pressure up to 9.0 GPa.

Finally, we comment on general gap closings at high-symmetry points. Some space groups allow high-symmetry points invariant under several rotational and mirror symmetries. In this case, more than two Weyl nodes and line nodes can appear from one symmetry point [69]. Meanwhile, we have discussed the band evolutions of the Weyl nodes and the line nodes in this subsection. For the cases (I)-(i) ((II)-(ii)), the Weyl (line) nodes move along the high-symmetry line (plane). In other words, the gapless nodes evolve along the high-symmetry line or plane giving the different symmetry eigenvalues to the two bands. The results can be generalized to many space groups. Namely, when topological nodes are formed by two bands with different symmetry eigenvalues, the nodes evolve on the high-symmetry line or plane which is associated with the different eigenvalues [69].

2.2.6 General theory of the Gap closing and the topological phase transitions

In order to realize a topological phase transition, a gap closing is necessary. However, to understand the topological phase transitions and the gap closing, we have used the simple two-band effective Hamiltonian. In this subsection, we intuitively explain that the two-band effective Hamiltonian is sufficient to describe the topological phase transitions if there are no band degeneracy. Detailed discussions about the gap closing can be seen in Ref. [71], for instance.

We consider a gap closing at $\mathbf{k} = \mathbf{k}_0$ in general systems with many nondegenerate bands. Even in such general cases, the gap closing occurs between two states near the Fermi energy after all. We call the two states $u_c(\mathbf{k}_0)$ and $u_v(\mathbf{k}_0)$ as shown in Fig. 2.9. Obviously, because the band gap locally closes between $u_c(\mathbf{k}_0)$ and $u_v(\mathbf{k}_0)$, the other bands are irrelevant to the gap. As a result, the gap closing can be described in the subspace of the Hilbert space spanned by $u_c(\mathbf{k}_0)$ and $u_v(\mathbf{k}_0)$ [71]. Hence, we can use a two-band effective Hamiltonian whose basis functions are $u_c(\mathbf{k}_0)$ and $u_v(\mathbf{k}_0)$ in order to study the gap closing.

The above statement also simplifies analysis of the topological phase transition followed by the gap closing. Topology of the occupied bands changes when the band gap closes. Meanwhile, the gap closing generally happens between the two states near the Fermi energy. Thus, we can know the change of the band topology by seeing only the two bands. In other words, the bands unrelated to the gap closing do not affect the change of the topology of the occupied bands, and therefore we only have to use the two-band effective Hamiltonian to investigate the topological phase transition.

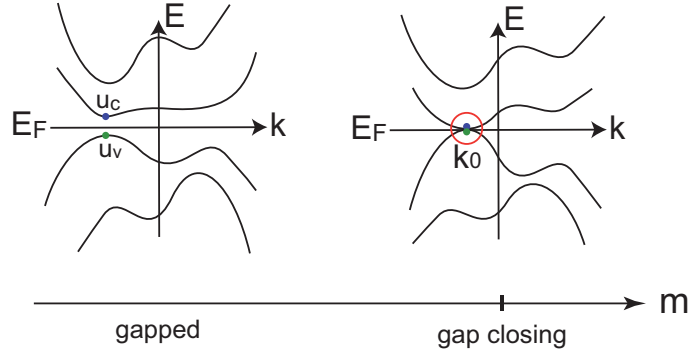


Figure 2.9: Schematic drawing of the gap closing between the two states $u_c(\mathbf{k}_0)$ and $u_v(\mathbf{k}_0)$. E_F represents the Fermi energy. When the parameter m is changed, the gap closes between the two states. The red circle indicates the gap closing at $\mathbf{k} = \mathbf{k}_0$.

2.2.7 Topological nodal-line semimetals

So far, we have considered topological materials with spin-orbit couplings. On the other hand, a novel topological semimetal phase appears in three-dimensional spinless systems. One example is a topological nodal-line (TNL) semimetal (SM). The TNLSM has a doubly degenerate nodal-line at general points near the Fermi energy [Fig. 2.10 (a)]. If spin degeneracy is considered in electronic systems, the TNL is fourfold degenerate. Therefore, TNLs are different from the nodal lines on the mirror plane explained in the previous subsection. We review the TNLSM in this subsection.

To realize the TNLSM phase, the system needs to have time-reversal and inversion symmetries. Let us discuss the requirements for the TNLSM phase. If the two symmetries are present in the spinless system, the Hamiltonian can be written as a real matrix when a suitable gauge is adopted [72, 73]. Because Kramers degeneracy is absent in the spinless system, gapless nodes at general points can be described by a two-band effective Hamiltonian. Since we can take the effective Hamiltonian to be real, it can be written as

$$H_{eff}(\mathbf{k}) = a_0(\mathbf{k})\mathbf{1}_{2\times 2} + a_x(\mathbf{k})\sigma_x + a_z(\mathbf{k})\sigma_z, \quad (2.54)$$

where the Pauli matrices act on the two-dimensional space spanned by the conduction band and the valence band. If the gapless nodes lie in the BZ, wavevectors satisfying $a_x = a_z = 0$ exist. Then, the solutions of $a_x = a_z = 0$ form lines in the BZ because there are three variables (k_x, k_y, k_z) in the three-dimensional system. Therefore, the TNLSM can be realized in the spinless system with time-reversal and inversion symmetries.

The TNLSM can have characteristic surface states called drumhead surface states. The drumhead surface states are nearly flat bands which typically appear inside the TNL projected onto the surface. However, existence of the drumhead surface states is not necessarily guaranteed because inversion symmetry characterizing the TNL is always broken at the surface [74, 75].

Experimentally, ZrSiS has been reported as a TNLSM [76–80]. The spin-orbit coupling is so weak that the gap is small enough to be negligible. The crystal structure is nonsymmorphic, and the space group is No. 129. The TNL in ZrSiS was observed on the glide plane by angle-resolved photoemission spectroscopy. Meanwhile, candidates of the TNLSM which await experimental verifications are carbon allotropes [72, 81, 82], Ca_3P_2 [83, 84], alkaline-earth metals [75, 85], $\text{Cu}_3(\text{Pd}, \text{Zn})\text{N}$ [86, 87], BaSn_2 [73], LaN [88], and compressed black phosphorus [89], CaP_3 [90] and so on.

In searching for the TNLSMs, the formula for the \mathbb{Z}_2 topological invariant using parity eigenvalues is useful [86]. The formula is given by

$$(-1)^{\nu_0} = \prod_{n_j=0,1} \prod_{m}^{occ.} \xi_m(\mathbf{\Gamma}_{n_1 n_2 n_3}), \quad (2.55)$$

where $\xi_m(\mathbf{\Gamma}_{n_1 n_2 n_3})$ is a parity eigenvalue of the m th occupied band at a TRIM $\mathbf{\Gamma}_{i=(n_1 n_2 n_3)}$ in Eq. (2.20). In the system with $\nu_0 = 1$, the energy bands necessarily have TNLs [86].

2.2.8 Topological protection of the topological nodal-line

The TNL is protected topologically by a quantized Berry phase ω [84, 86, 91]. The Berry phase ω is a loop integral of the Berry connection $\mathbf{A}(\mathbf{k})$ defined from all the occupied bands in the BZ [23]. The Berry phase is written as

$$\mathbf{A}(\mathbf{k}) = i \sum_n^{\text{occ.}} \langle u_{n\mathbf{k}} | \nabla_{\mathbf{k}} | u_{n\mathbf{k}} \rangle, \quad (2.56)$$

$$\omega = \oint_{\mathcal{C}} \mathbf{A}(\mathbf{k}) \cdot d\mathbf{k}, \quad (2.57)$$

where \mathcal{C} denotes a contour of the line integral. The Berry phase is quantized to only 0 or π modulo 2π in the spinless system with time-reversal and inversion symmetries [84, 86, 92], depending on the contour \mathcal{C} . To see a relationship between the TNL and the Berry phase, we calculate ω from the two-band Hamiltonian in Eq. (2.54). The Berry phase is given by [75, 93]

$$\omega = \pi \oint \frac{1}{2\pi} d\phi, \quad \tan \phi = \frac{a_z}{a_x}. \quad (2.58)$$

Therefore, we find that the Berry phase corresponds to a winding number of a map of the loop from \mathbf{k} space to (a_x, a_z) space. Thus, when \mathcal{C} surrounds a TNL like Fig. 2.10 (b), the Berry phase takes the value of π . Because the winding number is unchanged under a continuous change of the system, the TNLs are stable as long as time-reversal and inversion symmetries are present.

We can also exploit a Zak phase $\theta(\mathbf{k}_{\parallel})$ as another topological invariant [94]. The Zak phase is a Berry phase whose contour is a straight line connecting two equivalent ends of the BZ. \mathbf{k}_{\parallel} is a wavevector normal to the path. The Zak phase is sensitive to crystal symmetries [95, 96], and it is quantized to 0 or π modulo 2π in the TNLSM [75, 94, 95, 97]. This quantization also makes the TNLs stable topologically. The Zak phase jumps by π when the contour crosses the TNL.

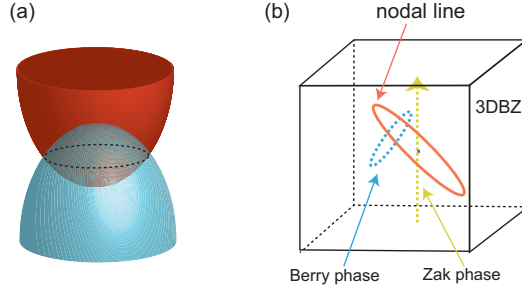


Figure 2.10: (a) shows the band structures of the TNLSM. (b) shows the contour of the Berry phase and the Zak phase which are equal to π . The blue and the yellow paths represent the contour of the Berry phase and the Zak phase, respectively.

Here, we show that in general no relationship exists between the drumhead surface states and the quantized Zak phase, although the Zak phase is one of the topological invariants. The Zak phase in the solid is proportional to surface charge density [95, 98]. The surface charge density per surface unit cell $\sigma_e(\mathbf{k}_{\parallel})$ is given by

$$\sigma_e(\mathbf{k}_{\parallel}) = \frac{e}{2\pi} \theta(\mathbf{k}_{\parallel}) \pmod{e}, \quad (2.59)$$

where the wavevector \mathbf{k}_{\parallel} is along the surface. In the TNLSM, the Zak phase can take the value of π , leading to $\sigma_e(\mathbf{k}_{\parallel}) = e/2$. On the other hand, surface states, if occupied, will contribute an integer multiple of e to $\sigma_e(\mathbf{k}_{\parallel})$, and therefore $\sigma_e(\mathbf{k}_{\parallel}) = e/2$ cannot be solely due to surface states. In fact, the surface charge is attributed to the bulk states [75]. Hence, the Zak phase is in general unrelated to the drumhead surface states. On the other hand, if the system has chiral symmetry, the surface states are related to the Zak phase. In the system with the chiral symmetry, the occupied and the unoccupied bands can contribute the surface charges equally. Thus, because the sum of the contributions is e , surface states can appear at zero energy [99].

2.2.9 Spinless nodal-line semimetals protected by mirror symmetry

Another type of nodal-line semimetals is also realizable on the mirror or the glide plane in spinless systems as explained in Sec. 2.2.5 because Kramers degeneracy is absent. The nodal line on the mirror plane is formed by two bands with opposite mirror eigenvalues. Therefore, the nodal lines stem from the same mechanism as the spinful nodal lines. Instead of mirror symmetry, glide symmetry allows the nodal line to appear on the glide plane. The spinless nodal-line semimetals have been reported in CaAgP and CaAgAs, which are noncentrosymmetric [100, 101]. In general, the protection by the mirror symmetry can coexist with the topological protection. Actually, the nodal lines in ZrSiS are protected also by the glide symmetry [76, 77].

2.2.10 Spinless Weyl semimetals

We can realize WSM phases in spinless systems when either time-reversal or inversion symmetry is absent [102–105], because the general two-band Hamiltonian in the spinless system is also given by Eq. (2.33). Then, if we realize spinless WSMs in electronic systems, the Weyl nodes are fourfold degenerate. The spinless WSM phase has been realized experimentally in a photonic crystal [106, 107]. Some spinless WSM phases appear between topologically trivial and nontrivial insulator phases characterized by some crystal symmetries [108, 109]. In some models, the spinless WSM is expected to be driven from the nodal-line semimetal by a circularly polarized light [110–115]. In the topological phase transition, if the drumhead surface states exist, Fermi arcs of the spinless WSM come from the tilted surface states of the nodal-line semimetal [112].

2.3 Topological superconductors

2.3.1 Bogoliubov-de Gennes Hamiltonian

In Sec. 2.1, we reviewed topological classification of the insulators. From the results, we can distinguish whether the gapped system is topological or not by means of the topological invariants. In this section, we extend the classification scheme to superconducting systems by considering the gap structure.

Before discussion of the topological classification, we introduce a Bogoliubov-de Gennes (BdG) Hamiltonian which describes quasiparticles in the superconductors (SCs). From the mean field theory, the BdG Hamiltonian is given by

$$H = \frac{1}{2} \sum_{\mathbf{k}, \alpha, \beta} (c_{\mathbf{k}\alpha}^\dagger, c_{-\mathbf{k}\alpha}) \mathcal{H}(\mathbf{k}) \begin{pmatrix} c_{\mathbf{k}\beta} \\ c_{-\mathbf{k}\beta}^\dagger \end{pmatrix}, \quad (2.60)$$

$$\mathcal{H}(\mathbf{k}) = \begin{pmatrix} \mathcal{E}_{\alpha\beta}(\mathbf{k}) & \Delta_{\alpha\beta}(\mathbf{k}) \\ \Delta_{\alpha\beta}^\dagger(\mathbf{k}) & -\mathcal{E}_{\alpha\beta}^t(-\mathbf{k}) \end{pmatrix}, \quad (2.61)$$

where $\mathcal{E}(\mathbf{k})$ is the normal-state Hamiltonian measured from the chemical potential, and $\Delta(\mathbf{k})$ is the gap function. The subscripts α and β indicate spin and orbital indices. Because of the fermion anticommutation relations, the gap function satisfies

$$\Delta_{\alpha\beta}(\mathbf{k}) = -\Delta_{\beta\alpha}(-\mathbf{k}). \quad (2.62)$$

Moreover, the BdG Hamiltonian has particle-hole symmetry C :

$$C\mathcal{H}(\mathbf{k})C^{-1} = -\mathcal{H}(-\mathbf{k}), \quad (2.63)$$

$$C = \begin{pmatrix} 0 & \mathbf{1}_N \\ \mathbf{1}_N & 0 \end{pmatrix} K, \quad C^2 = 1, \quad (2.64)$$

where $\mathbf{1}_N$ is the $N \times N$ unit matrix. By the particle-hole symmetry, the energy eigenvalue $E(-\mathbf{k})$ is equal to $-E(\mathbf{k})$. This particle-hole symmetry leads to difference between the insulators and the SCs in the topological classification [7].

Furthermore, particle-hole symmetry yields fermionic excitation which cannot be found in ordinary insulators. The fermion is called a Majorana fermion, which is a self-conjugate Dirac fermion. The Majorana fermion is identical with its antiparticle. In the SC, the quasiparticle is described as

$$\Psi(\mathbf{x}) = (c_\alpha(\mathbf{x}), c_\beta(\mathbf{x}), c_\alpha^\dagger(\mathbf{x}), c_\beta^\dagger(\mathbf{x}))^t. \quad (2.65)$$

Then, particle-hole symmetry C in Eq. (2.64) leads to

$$\Psi(\mathbf{x}) = C\Psi(\mathbf{x}). \quad (2.66)$$

From Eq. (2.66), the quasiparticle in the SC $\Psi(\mathbf{x})$ satisfies the self-conjugate condition since C is antiunitary. Therefore, this relationship suggests that Majorana fermions can appear in the SC.

In addition, we remark a relationship between the BdG Hamiltonian and crystal symmetries [116, 117]. When the normal state has a certain symmetry g which transforms \mathbf{k} as $\mathbf{k} \rightarrow D(g)\mathbf{k}$ with the matrix representation $D(g)$, the BdG Hamiltonian can preserve the symmetry depending on the gap function. For example, we assume that g is an unitary symmetry such as inversion and mirror symmetries of the normal state. By assumption, the normal-state Hamiltonian and g are related by

$$U_g \mathcal{E}(\mathbf{k}) U_g^{-1} = \mathcal{E}(D(g)\mathbf{k}), \quad (2.67)$$

where U_g is a matrix representation of g in the basis of the normal-state Hamiltonian. If the gap function is transformed by g as

$$U_g \Delta(\mathbf{k}) U_g^t = \eta_g \Delta(D(g)\mathbf{k}), \quad (2.68)$$

$$\eta_g = \pm 1, \quad (2.69)$$

the BdG Hamiltonian also has the symmetry g . Namely, the BdG Hamiltonian satisfies

$$\tilde{U}_g^{\eta_g} \mathcal{H}(\mathbf{k}) [\tilde{U}_g^{\eta_g}]^{-1} = \mathcal{H}(D(g)\mathbf{k}), \quad (2.70)$$

$$\tilde{U}_g^{\eta_g} = \begin{pmatrix} U_g & 0 \\ 0 & \eta_g U_g^* \end{pmatrix}. \quad (2.71)$$

When $\eta_g = 1(-1)$, particle-hole symmetry commutes (anticommutes) with g , which are given by

$$C \tilde{U}_g^{\eta_g} = \eta_g \tilde{U}_g^{\eta_g} C. \quad (2.72)$$

Therefore, we obtain

$$(C \tilde{U}_g^{\eta_g})^2 = \eta_g [\tilde{U}_g^{\eta_g}]^2. \quad (2.73)$$

In particular, when g is the space inversion P and $\eta_P = 1(-1)$, the SC is named an even-parity (odd-parity) SC. Spin-singlet and spin-triplet SCs typically belong to the even-parity and the odd-parity SCs, respectively. $\text{Cu}_x\text{Bi}_2\text{Se}_3$ is expected to realize an odd-parity SC [118–120]. In the inversion-symmetric SCs, we have from Eq. (2.73)

$$(C \tilde{U}_P^{\eta_P})^2 = \eta_P. \quad (2.74)$$

Meanwhile, when g is the mirror symmetry M and $\eta_M = 1(-1)$, we call the SC mirror-even (mirror-odd) SC [121, 122].

Hereafter, we do not distinguish g from U_g for brevity. In short, the matrix representation U_g is written as g below. We also denote $\tilde{U}_g^{\eta_g}$ as \tilde{g} , or as \tilde{g}^η with $\eta = \pm$ if necessary.

2.3.2 Spinless chiral p -wave superconductors

Firstly, we explain a two-dimensional spinless chiral SC as an example of the topological SCs. The chiral SC is realizable in spinless or spin-polarized systems. In general, spinless SCs are described by [123]

$$\mathcal{H}(\mathbf{k}) = \begin{pmatrix} \varepsilon_{\mathbf{k}} - \mu & \Delta(\mathbf{k}) \\ \Delta^*(\mathbf{k}) & -\varepsilon_{\mathbf{k}} + \mu \end{pmatrix} \equiv \mathbf{R}(\mathbf{k}) \cdot \boldsymbol{\tau}, \quad (2.75)$$

$$\mathbf{R}(\mathbf{k}) = (R_x, R_y, R_z) = (\text{Re}(\Delta(\mathbf{k})), -\text{Im}(\Delta(\mathbf{k})), \varepsilon_{\mathbf{k}} - \mu), \quad (2.76)$$

where $\boldsymbol{\tau} = (\tau_x, \tau_y, \tau_z)$ are Pauli matrices representing the particle-hole space, and $\varepsilon_{\mathbf{k}}$ and μ are the kinetic energy and the chemical potential, respectively. At small \mathbf{k} , $\varepsilon_{\mathbf{k}}$ is nearly equal to $\mathbf{k}^2/(2m^*)$ with the effective mass m^* . The energy eigenvalues are $E = \pm|R| = \pm\sqrt{R_x^2 + R_y^2 + R_z^2}$. The gap function is complex, and therefore the time-reversal symmetry is broken. Hence, we can use Eq. (2.4) to define a Chern number of the SC system if there is no node in the BZ. The Chern number is given by

$$n = \frac{1}{2\pi} \int dk_x dk_y \frac{-1}{2|R|^3} \varepsilon_{abc} R_a (\partial_{k_x} R_b) (\partial_{k_y} R_c), \quad (2.77)$$

where ε_{abc} is an antisymmetric tensor. If n is nonzero, gapless modes appear in the edge of the SC like a Chern insulator. However, the gapless edge modes do not carry charges because the quasiparticle is composed of an electron and a hole, although the SC is characterized by the same topological invariant as that of the Chern insulator.

Here, we consider a spinless chiral p -wave SC for example. For the chiral p -wave SCs, the gap function is an eigenfunction of angular momentum $l = \pm 1$. Now, let us treat the case for $l = -1$. The gap function at small \mathbf{k} takes the form

$$\Delta(\mathbf{k}) \simeq \hat{\Delta}(k_x - ik_y), \quad (2.78)$$

where $\hat{\Delta}$ is a positive constant. Then, we can write the BdG Hamiltonian near $\mathbf{k} = (0, 0)$ as

$$\mathcal{H}(\mathbf{k}) \simeq \hat{\Delta} k_x \tau_x + \hat{\Delta} k_y \tau_y - \mu \tau_z. \quad (2.79)$$

From Eq. (2.77) and (2.79), we obtain the Chern number $n = [1 + \text{sgn}(\mu)]/2$. Therefore, the chiral p -wave SC with $\mu > 0$ has gapless edge states. Then, from the similarity between Eq. (2.79) and Eq. (2.9), we apply a similar setup as used in Sec. 2.1.2 to confirm existence of the edge states. Let us assume $\mu(y) < 0$ ($\mu(y) > 0$) for $y > 0$ ($y < 0$). As a result, we obtain the gapless edge states with the energy $E = \hat{\Delta} k_x$:

$$\psi(x, y) = e^{ik_x x} e^{\frac{1}{\hat{\Delta}} \int_0^y \mu(y') dy'} \frac{1}{\sqrt{2}} \begin{pmatrix} 1 \\ -1 \end{pmatrix}. \quad (2.80)$$

From the argument in the previous subsection, the edge states behave as a Majorana fermion thanks to the particle-hole symmetry.

2.3.3 Weyl superconductors

If the time-reversal symmetry is broken, three-dimensional SCs can have point nodes formed by two nondegenerate states. In short, Weyl nodes can appear in the three-dimensional SC without the time-reversal symmetry. Such SCs are called Weyl SCs [124, 125]. The effective Hamiltonian near the Weyl node is described by

$$\mathcal{H}(\mathbf{k}) = v\mathbf{k} \cdot \boldsymbol{\tau}. \quad (2.81)$$

Thus, this Weyl node is characterized by the monopole charge $\text{sgn}(v)$.

From Eq. (2.81), we find that a relationship between the Weyl SC and the chiral SC is analogous to that between the WSM and the Chern insulator. This means that Weyl SCs have surface arc states between projections of the monopole and the antimonopole [124, 126, 127]. The arc is called a Majorana arc.

Unlike WSMs, Weyl SCs cannot be realized in the time-reversal invariant system without inversion symmetry. The reason stems from the intrinsic particle-hole symmetry in SCs. Thus, we consider monopole density in the time-reversal invariant SC to understand nonexistence of Weyl nodes. Particle-hole symmetry gives constraints on the Berry curvature $\boldsymbol{\Omega}(\mathbf{k})$ and the monopole density $\rho(\mathbf{k})$ [14],

$$\boldsymbol{\Omega}(\mathbf{k}) = \boldsymbol{\Omega}(-\mathbf{k}), \quad \rho(\mathbf{k}) = -\rho(-\mathbf{k}). \quad (2.82)$$

Now, because of the time-reversal symmetry, $\rho(\mathbf{k}) = \rho(-\mathbf{k})$ from Eq. (2.42). Therefore, the monopole density is always zero in the time-reversal invariant SC. In other words, the SC cannot have Weyl nodes in the presence of time-reversal symmetry. Actually, it is known that a gap closing gives rise to a topologically stable line node instead of Weyl nodes if the SC has time-reversal symmetry [128].

2.3.4 Topological crystalline superconductors

Although the spinless chiral p -wave SC is topologically nontrivial, it is realizable only in spinless systems. Therefore, a topological crystalline SC was proposed [121, 129], which can be realized in spinful systems. The topological crystalline SCs can appear when the BdG Hamiltonian has mirror symmetry. In this subsection, we discuss the topological crystalline SCs. We focus on SCs breaking time-reversal symmetry, whereas topological crystalline SCs are allowed in the presence of time-reversal symmetry [122, 129–131].

In mirror-symmetric SCs, we can label the states with mirror eigenvalues $\lambda = \pm i$ because $\tilde{M}\mathcal{H}(\mathbf{k})\tilde{M}^{-1} = \mathcal{H}(\mathbf{k})$ for the wavevector \mathbf{k} on the mirror plane. In other words, the BdG Hamiltonian on the mirror plane can be block-diagonalized in the diagonal basis of the mirror operation. Thus, we can write the BdG Hamiltonian on the mirror plane as

$$\mathcal{H}(\mathbf{k}) = \mathcal{H}_{+i}(\mathbf{k}) \oplus \mathcal{H}_{-i}(\mathbf{k}), \quad (2.83)$$

where $\mathcal{H}_{\pm i}(\mathbf{k})$ represents the mirror sector of $\lambda = \pm i$ after a unitary transformation. Therefore, we can define Chern numbers for each of the mirror sectors. The Chern numbers defined in this way are called mirror Chern numbers [11, 37]. To define the mirror Chern numbers, we introduce Berry connection $\mathbf{A}^\lambda(\mathbf{k})$ and Berry curvature $\mathbf{F}^\lambda(\mathbf{k})$ in the mirror sector $\mathcal{H}_\lambda(\mathbf{k})$ given by [121]

$$\mathbf{A}^\lambda(\mathbf{k}) = i \sum_n \langle u_n^\lambda(\mathbf{k}) | \nabla_{\mathbf{k}} | u_n^\lambda(\mathbf{k}) \rangle, \quad (2.84)$$

$$\mathbf{F}^\lambda(\mathbf{k}) = \nabla \times \mathbf{A}^\lambda(\mathbf{k}), \quad (2.85)$$

where $|u_n^\lambda(\mathbf{k})\rangle$ is the n th eigenstates of the BdG hamiltonian with the mirror eigenvalue λ . The sum in $\mathbf{A}^\lambda(\mathbf{k})$ is taken over the negative energy states. For instance, we take the mirror plane to be the xy plane. The mirror Chern number is then given by

$$\nu^{(\lambda)}(k_z) = \frac{1}{2\pi} \int dk_x dk_y F_z^\lambda, \quad (2.86)$$

where F_z^λ is integrated over the mirror plane ($k_z = 0$ or π). If the SC is gapped and some of $\nu^{(\lambda)}$ are nonzero, it is the topological crystalline SC.

Mirror-parity of the gap function determines properties of the mirror Chern numbers $\nu^{(\lambda)}$. To see this, we calculate a mirror eigenvalue of $C |u_n^\lambda(\mathbf{k})\rangle$. Because $C\tilde{M}^\eta = \eta\tilde{M}^\eta C$ where \tilde{M}^η with $\eta = \pm 1$ is the mirror operation, we obtain

$$\tilde{M}^\eta C |u_n^\lambda(\mathbf{k})\rangle = -\eta\lambda C |u_n^\lambda(\mathbf{k})\rangle. \quad (2.87)$$

Therefore, if the gap function is mirror-odd, each mirror sector has its own particle-hole symmetry because $C |u_n^\lambda(\mathbf{k})\rangle$ also has the same mirror eigenvalue as $|u_n^\lambda(\mathbf{k})\rangle$. Thanks to the particle-hole symmetry in each mirror sector, the nonzero mirror Chern number implies emergence of Majorana fermions on the edge [121]. Moreover, the mirror Chern numbers of the two sectors are independent [122]. On the other hand, if the gap function is mirror-even, each mirror sector does not support particle-hole symmetry because $C |u_n^\lambda(\mathbf{k})\rangle$ has the opposite mirror eigenvalue from that of $|u_n^\lambda(\mathbf{k})\rangle$. Thus, emergent gapless edge states are just Dirac fermions but not Majorana fermions [121]. Then, $\nu^{(+i)} = \nu^{(-i)}$ since particle-hole symmetry connects the two mirror sectors [122].

In three-dimensional topological crystalline SCs, strong and weak topological invariants are actually defined in a similar way as those of the \mathbb{Z}_2 topological insulators [131]. The strong topological invariant $N_{M\mathbb{Z}}$ is given by

$$N_{M\mathbb{Z}} = \text{sgn}(\nu(0) - \nu(\pi))(|\nu(0)| - |\nu(\pi)|), \quad (2.88)$$

where $\nu(k_z)$ represents either of $\nu^{(\pm i)}(k_z)$. The weak topological invariant N_{weak} is given by

$$N_{weak} = \begin{cases} \text{sgn}(\nu(0)) \min(|\nu(0)|, |\nu(\pi)|) & (\nu(0)\nu(\pi) > 0) \\ 0 & (\nu(0)\nu(\pi) < 0) \end{cases} \quad (2.89)$$

However, if the mirror symmetry is broken, the nontrivial invariants do not ensure existence of the surface states. The reason is that the bulk-edge correspondence is characterized by the mirror symmetry. Hence, in order to obtain the topological surface states, we need to terminate the topological crystalline SC while preserving the translational symmetry in the direction normal to the mirror plane [131].

2.3.5 Detection of topological superconductivity

In this subsection, we show several ways to observe topological superconductivity. Since Majorana fermions lie on the surface of topological SCs, the detection is very important to elucidate the nontrivial topology. Moreover, because gapless SCs such as Weyl SCs have bulk nodes, the phase can be determined from bulk thermodynamic properties.

To begin with, we introduce experimental methods of detection of the Majorana fermions. The famous example is tunneling spectroscopy which gives the tunneling conductance spectra. For instance, if one-dimensional topological superconductors without time-reversal symmetry have a single Majorana fermion, the zero-bias peak conductance is quantized to [132, 133]

$$\left. \frac{dI}{dV} \right|_{V=0} = \frac{2e^2}{h}, \quad (2.90)$$

where I is the tunneling current and V is the bias voltage. In two- and three-dimensional topological SCs, a broad zero-bias peak also appears. The zero-bias peak was observed in $\text{Cu}_x\text{Bi}_2\text{Se}_3$, which is a candidate of the topological SCs [120]. The experimental signature is expected to suggest existence of the Majorana fermions.

Next, we discuss thermodynamic properties of Weyl superconductivity. When the system is in the Weyl SC phase, the density of bulk states becomes different from that of the gapped SCs because of the Weyl nodes. Therefore, we expect to observe signature of the Weyl nodes from specific heat C , relaxation rate of nuclear magnetic resonance T_1 and so on, because they are dependent on the density of states [134]. Actually, if the point nodes exist in the SCs, C and T_1 shows unique dependence of temperature T [134], which are described by

$$C \propto T^3, \quad (2.91)$$

$$\frac{1}{T_1} \propto T^5. \quad (2.92)$$

For example, the specific heat was experimentally measured in $\text{PrOs}_4\text{Sb}_{12}$ [135], and the result is indicative of existence of the point nodes. $\text{PrOs}_4\text{Sb}_{12}$ is also theoretically expected to be nonunitary chiral SCs with Weyl nodes [136].

Chapter 3

Topological surface states and their evolution in Weyl semimetal and topological insulator phases

In this chapter, we discuss evolution of surface states when a topological phase transition occurs between Weyl semimetal (WSM) and three-dimensional \mathbb{Z}_2 topological insulator (TI) phases. We abbreviate the three-dimensional \mathbb{Z}_2 TI just to TI, in this chapter. Particularly, we investigate on time-reversal invariant systems without inversion symmetry, where both of the WSM and the TI are realizable. Firstly, we construct an effective Hamiltonian which describes the phase transition between the WSM and the insulating phases. Moreover, we show that Fermi arcs, which are surface states of the WSM, consist of top-surface and bottom-surface states with opposite velocities. Secondly, we study changes of the surface states at the phase transition from the WSM to the TI by using a lattice model. As a result, we find that a pair of surface Fermi arcs evolves into a surface Dirac cone when the system moves from the WSM to the TI. We also show that the results of the lattice model agree with those of the effective Hamiltonian. Finally, we also demonstrate that choices of surface termination affect the pairing of Weyl nodes, from which the Fermi arcs are formed.

This chapter is organized follows. In Sec. 3.1, we construct a two-band effective Hamiltonian, and calculate surface states of the WSM by using the effective Hamiltonian. In Sec. 3.2, we study changes of the surface states by using a lattice model realizing both TI and WSM phases when the topological phase transition happens between these two phases. We also discuss how the results of the changes of the surface states are applied to general WSMs. We summarize our results in Sec. 3.3

3.1 Effective Hamiltonian for NI-WSM-TI phase transition

3.1.1 Construction of the effective Hamiltonian

In this section, we construct an effective Hamiltonian describing the phase transition between WSM and insulator phases in order to investigate evolution of the surface energy bands. Because the energy bands are nondegenerate due to the breaking of inversion or time-reversal symmetry, the effective model can be described by a 2×2 Hamiltonian in Eq. (2.48),

$$H(\mathbf{k}, m) = a_0(\mathbf{k}, m) + \sum_{i=x,y,z} a_i(\mathbf{k}, m) \sigma_i, \quad (3.1)$$

where $\sigma_{x,y,z}$ are Pauli matrices representing a valence band and a conduction band. m is an arbitrary parameter which controls the phase transition. Suppose that the region $m > m_c$ is the WSM phase, and that $m < m_c$ is the insulating phase. Namely, the phase transition occurs at $m = m_c$ and the energy bands become gapless. Let us assume that $\mathbf{k} = \mathbf{k}_0$ is a gapless point at $m = m_c$, i.e.

$$a_i(\mathbf{k}_0, m_c) = 0 \quad (i = 1, 2, 3). \quad (3.2)$$

To see the dispersion at $m = m_c$, we expand $\mathbf{a} = (a_1, a_2, a_3)$ around (\mathbf{k}_0, m_c) up to linear order \mathbf{k} and m :

$$\mathbf{a}(\mathbf{k}, m) = M \Delta \mathbf{k} + \Delta m \mathbf{N}, \quad (3.3)$$

where $\Delta k_i = k_i - k_{0i}$, $\Delta m = m - m_c$, $M_{ij} = \frac{\partial a_i}{\partial k_j} |_{\mathbf{k}=\mathbf{k}_0, m=m_c}$ and $N_i = \frac{\partial a_i}{\partial m} |_{\mathbf{k}=\mathbf{k}_0, m=m_c}$. If $\det M \neq 0$, M^{-1} exists and we have

$$\Delta \mathbf{k} = -M^{-1} \mathbf{N} \Delta m. \quad (3.4)$$

Equation (3.4) means that gapless points are present in both of the regions $m < m_c$ and $m > m_c$. This result is inconsistent with the initial assumption, and therefore $\det M = 0$ holds true. Thus, M has a zero eigenvalue whose eigenvector satisfies

$$M \mathbf{n}_1 = 0. \quad (3.5)$$

Here, we define a matrix R by using all the normalized eigenvectors of M , \mathbf{n}_1 , \mathbf{n}_2 , and \mathbf{n}_3 as

$$R = (\mathbf{n}_1, \mathbf{n}_2, \mathbf{n}_3). \quad (3.6)$$

We rotate the coordinate by R , and we introduce a new basis \mathbf{p} defined as

$$\Delta \mathbf{k} = R \Delta \mathbf{p}. \quad (3.7)$$

Thus, we obtain up to the linear order in $\Delta \mathbf{p}$ and Δm ,

$$\mathbf{a} = \Delta p_2 \mathbf{u}_2 + \Delta p_3 \mathbf{u}_3 + \Delta m \mathbf{N}, \quad (3.8)$$

where $\mathbf{u}_i = M\mathbf{n}_i$. Since $\mathbf{u}_1 = M\mathbf{n}_1 = 0$, the linear term of Δp_1 in the expression of \mathbf{a} vanishes. Therefore, the lowest order of Δp_1 is quadratic [53], and we obtain

$$\mathbf{a}(\mathbf{q}, m) = \Delta p_2 \mathbf{u}_2 + \Delta p_3 \mathbf{u}_3 + (\Delta p_1)^2 \mathbf{u}_{11} + \Delta m \mathbf{N}, \quad (3.9)$$

where \mathbf{u}_{11} is a vector. Hence, we find that the gapless energy bands are quadratic in one direction in the wavevector space and linear in the other two directions at the phase transition point. To obtain the effective Hamiltonian, we assume for simplicity

$$\mathbf{u}_{11} = -\mathbf{N} = \begin{pmatrix} \gamma \\ 0 \\ 0 \end{pmatrix}, \quad \mathbf{u}_2 = \begin{pmatrix} 0 \\ v \\ 0 \end{pmatrix}, \quad \mathbf{u}_3 = \begin{pmatrix} 0 \\ 0 \\ v \end{pmatrix}, \quad (3.10)$$

where γ and v are nonzero constants. Thus, the two-band effective Hamiltonian is given by [17]

$$H = \gamma \{(\Delta p_1)^2 - \Delta m\} \sigma_x + v \Delta p_2 \sigma_y + v \Delta p_3 \sigma_z. \quad (3.11)$$

We put $a_0 = 0$ because this term only displaces the energy. From the first term in this Hamiltonian, the energy bands are gapless when $\Delta m > 0$, and gapped when $\Delta m < 0$. Therefore, this effective Hamiltonian indeed describes the energy bands in the topological phase transition between the WSM and the insulator. The details of the Hamiltonian are studied in the next subsection.

The effective Hamiltonian in Eq. (3.11) is applicable to general WSMs, regardless of breaking of inversion or time-reversal symmetry, because we just consider the topological phase transition between the WSM and the insulator. Hence, the effective Hamiltonian is valid as long as a monopole and an anti-monopole are close to each other.

3.1.2 Surface states from the effective Hamiltonian

We clarify properties of the surface states by using the effective Hamiltonian in this subsection. Hereafter, we put $\mathbf{k}_0 = 0$ and $m_c = 0$ by a shift of the origin. In addition, we take the rotated coordinate to simplify the effective Hamiltonian in Eq. (3.11), and we simply write \mathbf{k} instead of \mathbf{p} in Eq. (3.11). We also set γ and v to be positive for simplicity. Then, the effective Hamiltonian is written as

$$H = \gamma(k_x^2 - m)\sigma_x + vk_y\sigma_y + vk_z\sigma_z. \quad (3.12)$$

From the effective Hamiltonian, the bulk dispersion is given by

$$E = \pm \sqrt{\gamma^2(k_x^2 - m)^2 + v^2k_y^2 + v^2k_z^2}. \quad (3.13)$$

When $m < 0$, the energy bands are gapped out with a gap $2|\gamma m|$. In contrast, when $m > 0$, the bulk bands have two Weyl nodes $\mathbf{W}_\pm = (\pm\sqrt{m}, 0, 0)$. These Weyl nodes \mathbf{W}_+ and \mathbf{W}_- are a monopole and an antimonopole for the lower

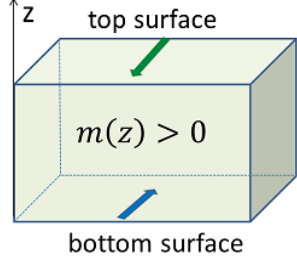


Figure 3.1: Top and bottom surfaces of the WSM with $m > 0$. The green and blue arrows represent the velocities of the top- and bottom-surface states of opposite signs, respectively.

band, respectively, because the monopole charge q_{\pm} at W_{\pm} is given by $q_{\pm} = \text{sgn}[\gamma k_x|_{k_x=\pm\sqrt{m}}]$.

Let us consider a surface of the WSM phase with $m > 0$, while regarding the vacuum as a region with negative m . Namely, m depends on the position and changes its sign at the boundary between the WSM and the vacuum. By assuming that the surface is along the xy plane for simplicity, the normal direction of the two surfaces are $\pm z$, corresponding to the top surface and the bottom one. Then, we put the z -dependence of $m(z)$ across the top surface as

$$m(z) = m_0 \quad z \rightarrow -\infty, \quad (3.14)$$

$$m(z) < 0 \quad z \rightarrow +\infty, \quad (3.15)$$

and that across the bottom surface as

$$m(z) < 0 \quad z \rightarrow -\infty, \quad (3.16)$$

$$m(z) = m_0 \quad z \rightarrow +\infty, \quad (3.17)$$

where m_0 is a positive constant characterizing the WSM (Fig. 3.1).

To find the surface states, we replace k_z with $-i\partial/\partial z$ because of the absence of the translational symmetry in the z direction. Moreover, by unitary transformation with $U = \frac{1}{\sqrt{2}}(1 - i\sigma_x)$, the Hamiltonian is transformed to

$$\begin{aligned} H' &\equiv U^{-1} H U = \gamma(k_x^2 - m)\sigma_x - iv\frac{\partial}{\partial z}\sigma_y - vk_y\sigma_z \\ &= \begin{pmatrix} -vk_y & \gamma(k_x^2 - m) - v\frac{\partial}{\partial z} \\ \gamma(k_x^2 - m) + v\frac{\partial}{\partial z} & vk_y \end{pmatrix}. \end{aligned} \quad (3.18)$$

By using the Hamiltonian H' , we obtain the bound states on the top surface given by

$$\psi_T = \begin{pmatrix} 1 \\ 0 \end{pmatrix} e^{-(\gamma/v) \int^z (k_x^2 - m(z)) dz}, \quad E = -vk_y \quad (3.19)$$

and that on the bottom surface given by

$$\psi_B = \begin{pmatrix} 0 \\ 1 \end{pmatrix} e^{(\gamma/v) \int^z (k_x^2 - m(z)) dz}, \quad E = vk_y. \quad (3.20)$$

They are respectively allocated as top-surface and bottom-surface states because otherwise the wave function diverges at some region and is not normalizable under the conditions (3.14)-(3.17). From the normalizability condition of the states (3.19) and (3.20), both surface states exist only when

$$-\sqrt{m_0} < k_x < \sqrt{m_0}. \quad (3.21)$$

At the Fermi energy $E = 0$, the top-surface and the bottom-surface states are degenerate, and are located at

$$k_y = 0, \quad -\sqrt{m_0} < k_x < \sqrt{m_0}, \quad (3.22)$$

which is a line connecting the two-dimensional projection of the Weyl points $W_{\pm} = (\pm\sqrt{m_0}, 0, 0)$ (Fig. 3.2(a) and 3.2(b)). Thus, these surface states are Fermi arcs. We also note that a velocity of the top-surface states is opposite to that of the bottom-surface states. The velocity of the top surface states is

$$\mathbf{v}_T = \frac{\partial E}{\partial \mathbf{k}} = (0, -v), \quad (3.23)$$

and that of the bottom surface states is

$$\mathbf{v}_B = \frac{\partial E}{\partial \mathbf{k}} = (0, v). \quad (3.24)$$

Their signs are consistent with the fact that W_{\pm} are a monopole and an anti-monopole, respectively. The velocity signs follow from the fact that on the slice of the three-dimensional Brillouin zone (BZ) at $k_x = \text{const.}$, the lower band has a Chern number 0 for $\sqrt{m_0} < |k_x|$ and -1 for $-\sqrt{m_0} < k_x < \sqrt{m_0}$ owing to the antimonopole at W_- .

Next, we focus on the energy band away from the Fermi energy $E = 0$. When the system has the surface, the energy bands have not only the surface states but also the bulk bands projected onto the surface BZ. Hence, to understand how the bulk bands and the surface bands are related, we project the bulk dispersion represented by Eq. (3.13) onto the surface. The projection of the bulk bands is in the region

$$E \geq \sqrt{\gamma(k_x^2 - m)^2 + v^2 k_y^2}, \quad (3.25)$$

$$E \leq -\sqrt{\gamma(k_x^2 - m)^2 + v^2 k_y^2}, \quad (3.26)$$

which describe the conduction and the valence bands, respectively. These projected bulk bands naturally have two point nodes at $W_{\pm} = (\pm\sqrt{m_0}, 0)$, which correspond to the bulk Weyl nodes, as seen in Figs. 3.2(a) and 3.2(b). On the

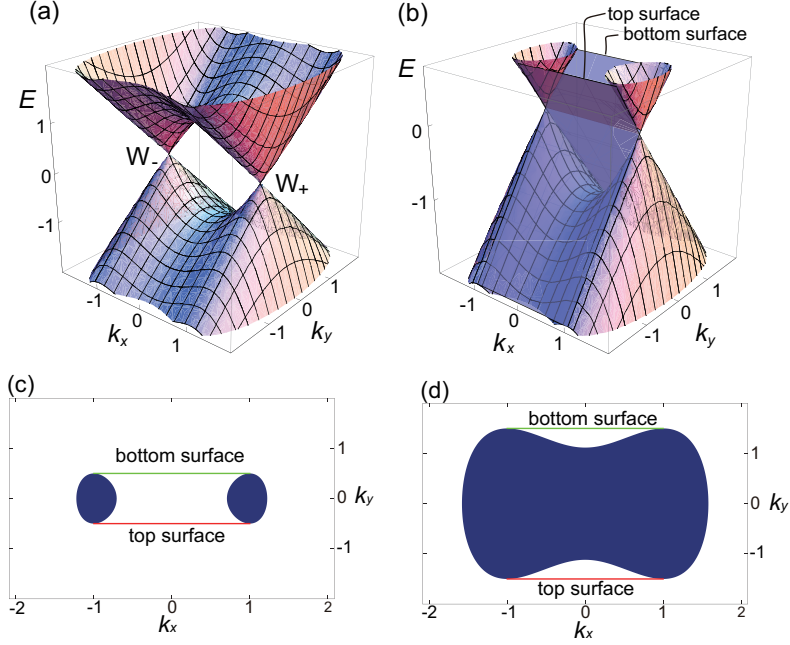


Figure 3.2: Bulk and surface states of the effective model (3.12) for the WSM. The parameters are set as $v = \gamma = m_0 = 1$. (a) shows the bulk states, and (b) shows the surface Fermi arcs and the bulk states. (c) and (d) The Fermi surface for the Fermi energy at (c) $E = 0.5$ and at (d) $E = 1.5$.

other hand, the surface states are tangential to these conical dispersions. While the surface states tangential to the cones are proposed in Ref [9] without calculations, the results are confirmed by our calculation based on the effective Hamiltonian.

In order to see a further relationship between the projection of the bulk bands and the surface bands, we show the Fermi surface at a constant energy. The bulk-band projection changes its topology at $E = \pm\gamma m_0$ by two distinct pockets becoming one pocket. When $-\gamma m_0 < E < \gamma m_0$, the bulk-band projection forms two distinct pockets as shown in Fig. 3.2(c). Meanwhile, when $|E| > \gamma m_0$, it forms one pocket with a dumb-bell-like structure [Fig. 3.2(d)]. Nevertheless, it is remarkable that the Fermi arcs merge to the bulk-band projection at the two ends, and at both ends they are tangential to the projected bulk bands independently of the topology of the bulk-band projection.

It should be noted that the above results can be applied to generic WSMs because the generic effective Hamiltonian are used for the calculations. Hence, we expect that this dispersion holds for general WSMs with a pair of Weyl nodes that are close to each other.

3.2 Numerical calculation of surface states of Weyl semimetal in a lattice model

3.2.1 Model

In this section, we numerically calculate surface states in a WSM phase to compare the results with the discussion in Sec 3.1. For this purpose, we begin with the Fu-Kane-Mele (FKM) tight-binding model [28], which is known to show various TI phases. This tight-binding model is defined on a diamond lattice and it has both inversion and time-reversal symmetries. Therefore, the FKM model does not show the WSM phase. To study the WSM phase, we add a staggered on-site potential to the model to break inversion symmetry. The FKM model with the additional on-site potential is

$$H = \sum_{\langle i,j \rangle} t_{ij} c_i^\dagger c_j + i \frac{8\lambda_{so}}{a^2} \sum_{\langle\langle i,j \rangle\rangle} c_i^\dagger \mathbf{s} \cdot (\mathbf{d}_{ij}^1 \times \mathbf{d}_{ij}^2) c_j + \lambda_v \sum_i \xi_i c_i^\dagger c_i, \quad (3.27)$$

where \mathbf{s} are Pauli matrices and a is the lattice constant for the cubic unit cell. The first term is the nearest-neighbor hopping with hopping amplitude t_{ij} . The second term represents the spin-orbit interaction for next-nearest-neighbor hopping with a spin-orbit coupling parameter λ_{so} . \mathbf{d}_{ij}^1 and \mathbf{d}_{ij}^2 are the nearest neighbor vectors connecting second-neighbor sites i and j . The third term represents the staggered on-site energy $\pm\lambda_v$, where λ_v is a constant and $\xi_i = \pm 1$ depends on the sublattices, i.e. $\xi = +1$ for the A sublattice and $\xi = -1$ for B sublattice for the diamond lattice.

Before studying the WSM phase, we briefly explain the model of Eq. (3.27) without the third term. It is the FKM model, and it is time-reversal invariant and inversion-symmetric. In the diamond lattice, there are four directions of the nearest-neighbor bonds. The hopping integrals along the bonds in the 111, $1\bar{1}\bar{1}$, $\bar{1}1\bar{1}$, and $\bar{1}\bar{1}1$ directions are denoted as t_1 , t_2 , t_3 , and t_4 , respectively. When the four nearest-neighbor hoppings t_α ($\alpha = 1, 2, 3, 4$) are different, the band structure of the FKM model are gapped. The system shows various TI phases of either strong topological insulator (STI) or weak topological insulator (WTI) phases. On the other hand, provided that the nearest-neighbor hopping t_{ij} are identical, the energy bands of the FKM model are gapless and form Dirac cones at three X points. However, it is not a WSM but a Dirac semimetal which is not protected topologically because of the inversion and the time-reversal symmetries.

To realize the WSM phase, we need to break inversion or time-reversal symmetry. Now, we consider the time-reversal invariant WSM phase which appears between the STI and the WTI phases, to see a relationship between the Fermi arc and the Dirac cone. In Ref. [53], it is shown that by adding the λ_v term to the FKM model, this model shows the WSM phase breaking inversion symmetry. The Hamiltonian matrix is

$$\mathcal{H}(\mathbf{k}) = \begin{pmatrix} \lambda_v \mathbf{1} + \sum_{i=1}^3 F_i s_i & f \mathbf{1} \\ f^* \mathbf{1} & -\lambda_v \mathbf{1} - \sum_{i=1}^3 F_i s_i \end{pmatrix}, \quad (3.28)$$

where

$$f = t_1 + t_2 e^{i\mathbf{k}\cdot\mathbf{a}_2} + t_3 e^{i\mathbf{k}\cdot\mathbf{a}_3} + t_4 e^{i\mathbf{k}\cdot\mathbf{a}_1}, \quad (3.29)$$

$$F_x = -4\lambda_{so} \sin \frac{a}{2} k_x \left(\cos \frac{a}{2} k_y - \cos \frac{a}{2} k_z \right), \quad (3.30)$$

and F_y and F_z are given by cyclic permutation of the subscripts x , y , and z in F_x . The primitive vectors of the fcc lattice are defined as $\mathbf{a}_1 = \frac{a}{2}(1, 1, 0)$, $\mathbf{a}_2 = \frac{a}{2}(0, 1, 1)$, $\mathbf{a}_3 = \frac{a}{2}(1, 0, 1)$. The energy eigenvalues are

$$E(\mathbf{k}) = \pm \sqrt{(\lambda_v \pm |\mathbf{F}|)^2 + |f|^2}, \quad (3.31)$$

where $\mathbf{F} = (F_x, F_y, F_z)$. Therefore, the spectrum is gapless when

$$\text{Re}f = \text{Im}f = 0, \quad \lambda_v = \pm |\mathbf{F}|. \quad (3.32)$$

In some parameter region, the three equations (3.32) for three parameters k_x , k_y , and k_z have solutions, showing the locations of the Weyl nodes. The bulk gap is then closed and the WSM phase appears there.

3.2.2 Numerical calculation of surface states

In Ref. [53], phase diagrams of this model are studied and this model is shown to exhibit the STI, WTI, and WSM phases by changing parameters. As an example, we assume $t_1 = t + \delta t_1$, $t_2 = t + \delta t_2$, $t_3 = t_4 = t$ and $\delta t_- = \delta t_1 - \delta t_2$ is fixed to be positive while $\delta t_+ = \delta t_1 + \delta t_2$ is varied. For the case with inversion symmetry, i.e. $\lambda_v = 0$, a band inversion at $X^x = \frac{2\pi}{a}(1, 0, 0)$ occurs at $\delta t_+ = 0$, accompanied by a phase transition between the STI phase with the Z_2 topological number 1;(111) ($\delta t_+ > 0$) and the WTI phase with the Z_2 topological number 0;(010) ($\delta t_+ < 0$) [28]. As a result, when the system is in the STI phase, a surface Dirac cone arises at the point $X^x = \frac{2\pi}{a}(1, 0, 0)$ projected onto the surface BZ, while in the WTI phases there is no surface Dirac cone at this point.

If one introduces an on-site staggered potential λ_v , the inversion symmetry is broken while the time-reversal symmetry is preserved. Then the WSM phase intervenes between the STI and the WTI phases, as shown in Fig. 3.3 (a). In the WSM phase, there are four Weyl nodes around the X^x point, as found in Ref. [53]. These four Weyl nodes move as the parameter $\delta t_+ = \delta t_1 + \delta t_2$ changes. Among these four Weyl nodes, two are monopoles and the other two are antimonopoles, which distribute symmetrically with respect to the X^x point. On the surface, two Fermi arcs will arise, connecting monopole-antimonopole pairs. For calculations we fix $\delta t_- = \delta t_1 - \delta t_2 = 0.1t$ and $\lambda_{so} = 0.1t$.

To see surface states, we numerically diagonalize Eq. (3.27) in a slab geometry with (111) surfaces. To show the surface states, we take the z axis to be the surface normal along [111], the x axis along the surface in the $\mathbf{a}_3 - \mathbf{a}_1$ direction and the y axis to be perpendicular to the x and z axes. The top surface of the slab is composed of lattice sites in the sublattice A and the bottom surface is

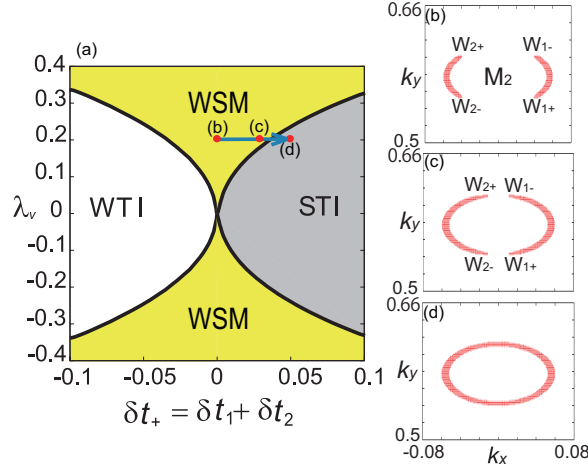


Figure 3.3: (a) Phase diagram in the $\delta t_+ - \lambda_v$ plane, with $\delta t_- = 0.1t$ and $\lambda_{so} = 0.1t$, where $\delta t_{\pm} = \delta t_1 \pm \delta t_2$. The axes are in the unit of t . When $\lambda_v = 0$, the system is inversion-symmetric, and no WSM phase appears. (b)-(d) Surface Fermi surface at $E = 0$ around the point M_2 near the Fermi level with $\lambda_v = 0.2t$ and the following values for δt_+ : (b) $\delta t_+ = 0$ (WSM), (c) $\delta t_+ = 0.03t$ (WSM), and (d) $\delta t_+ = 0.05t$ (STI). The axes are in the unit of $2\pi/b$. (b) and (c) show Fermi arcs in the WSM phase, and (d) shows a surface Dirac cone in the STI phase. We note that the end points of the surface Fermi arcs in the WSM phase are the gapless points of the bulk bands.

composed of lattice sites in the sublattice B. Because the point X^x is projected to the point $M_2 = \frac{2\pi}{b}(0, 1/\sqrt{3})$ in the hexagonal surface BZ, the Dirac cones and the Fermi arcs appear around the point M_2 . Here $b = a/\sqrt{2}$ is the length of the primitive vectors of the slab.

Figures 3.3 (b)-(d) show Fermi surfaces of a slab at $E = 0$ for various values of δt_+ , with $\delta t_- = 0.1t$ and $\lambda_{so} = 0.1t$. For (b) $\delta t_+ = 0$ and (c) $\delta t_+ = 0.03$, the system is in the WSM phase, and Fermi arcs appear around the point M_2 in the surface BZ, corresponding to the point X^x in the bulk BZ. The ends of the arcs are the Weyl nodes projected onto the surface BZ. Among the four Weyl points, let W_{1+} and W_{2+} denote the monopoles, and let W_{1-} and W_{2-} denote the antimonopoles, which are shown in Figs. 3.3 (b) and (c). As δt_+ is changed, the Weyl nodes move around this M_2 point, and concomitantly the Fermi arcs grow as seen in Figs. 3.3(b) and (c). As δt_+ is increased further, the system eventually enters the STI phase. At the WSM-STI phase transition, the Weyl nodes annihilate pairwise for (W_{1-}, W_{2+}) and (W_{1+}, W_{2-}) , and there is no Weyl node in the STI phase, with a nonzero bulk gap. Correspondingly, as we see in Fig. 3.3(d), the two Fermi arcs in the WSM phase are merged into a surface Dirac cone in the STI phase.

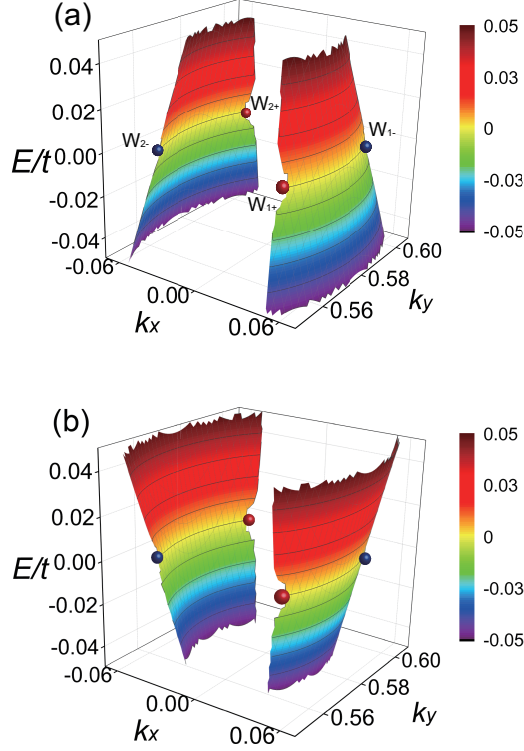


Figure 3.4: Side views of the Fermi arcs around the point $M_2 = \frac{2\pi}{b}(0, 1/\sqrt{3})$ with $\lambda_v = 0.2t$, $\delta t_+ = 0$ (WSM phase) for (a) the top surface and (b) the bottom surface. The k_x and k_y axes are in the unit of $2\pi/b$. The red (blue) points are the gapless points which have positive (negative) monopole charges for the Berry curvature.

So far we have discussed the surface states on $E = 0$, where the states on the top surface and those on the bottom surface are degenerate. The top-surface states and bottom-surface states are expected to have different dispersions, as Fig. 3.2 (b) shows. Figure 3.4 shows the results for the dispersion of the Fermi arcs on the top- and bottom-surface states in the present model. We note that the top- and bottom-surface states between a pair of Weyl nodes have opposite velocities, and the signs of the velocities are consistent with the monopole charges of $W_{i\pm}$ ($i = 1, 2$). To see this, let us focus on the surface Fermi arc between W_{1+} and W_{1-} as an example, and ignore the other Fermi arc. Let us take a two-dimensional slice of the three-dimensional BZ, which includes the surface normal ([111] direction). If the slice does not intersect the line between $W_{1\pm}$, the Chern number is zero within this two-dimensional slice, while it is one when the slice intersects the line between $W_{1\pm}$ because of the presence of the

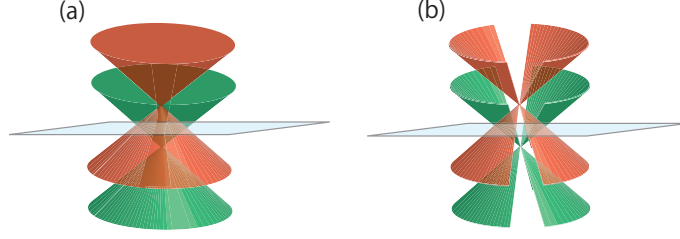


Figure 3.5: Schematic drawing of the surface energy bands around a TRIM. The red (green) cone is the top (bottom) surface states. (a) In the STI phase, the two Dirac cones on the top and bottom surfaces are split in energy when the inversion symmetry is broken. (b) In the WSM phase, there are a pair of Fermi arcs on each surface. These Fermi arcs will evolve into a Dirac cone shown in (a) in the STI phase.

monopole at W_{1+} . This means that within this slice there should be a clockwise topological edge mode, which appears as a surface mode with negative velocity $v_x < 0$ on the top surface and that with positive velocity $v_x > 0$ on the bottom surface. As is consistent with the result of the effective model (Fig. 3.2 (b)), each of these surface Fermi arcs is bridged between two Dirac cones around the Weyl nodes. As δt_+ is increased and the system undergoes the phase transition from the WSM phase into the STI phase, the two Fermi arcs merge into a single Dirac cone on the top surface, and the same occurs on the bottom surface. As a result there arises a top-surface Dirac cone and a bottom-surface Dirac cone, which are nondegenerate as shown schematically in Fig. 3.5(a). This splitting of the Dirac cones are natural, because of the breaking of the inversion-asymmetry due to the staggered on-site energy λ_v . In the present case, the topmost layer in the top (bottom) surface is A sublattice (B sublattice), and therefore the top-surface (bottom-surface) states have a larger (smaller) energy due to the staggered on-site energy λ_v .

The surface states in the whole BZ for $\delta t_+ = 0$ (WSM) and $\delta t_+ = 0.05t$ (STI) when $\lambda_v = 0.2t$ are shown in Figs. 3.6 (a1) and (b1). In addition to the surface states around M_2 , there are Dirac cones around M_1 and M_3 . Nevertheless, they are intact at the WTI-WSM-STI phase transition, because this phase transition is related with a band inversion at X_x , which is projected onto the M_2 point.

3.2.3 WSM-TI phase transition and evolution of the Fermi-arc surface states

Based on the calculation results on the model (3.27), here we discuss general features of the evolution of the Fermi-arc surface states in the WSM phase when some parameter is changed. In the WSM phase there are an even number of Weyl nodes. In the inversion-asymmetric phases with time-reversal symmetry, the minimal number is four, i.e., two monopoles and two antimonopoles. In this

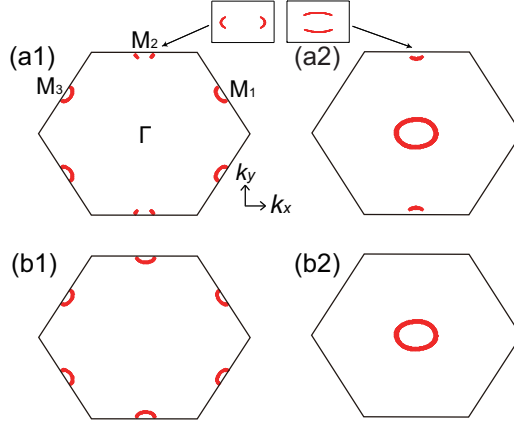


Figure 3.6: The surface Fermi surfaces at $E = 0$ in the whole BZ when $\lambda_v = 0.2t$. The values of δt_+ is $\delta t_+ = 0$ (WSM) for (a1) and (a2), and $\delta t_+ = 0.05t$ (STI) for (b1) and (b2). In (a1) and (b1), the surfaces are terminated without dangling bonds, and in (a2) and (b2) with dangling bonds. The insets show the magnified images of the surface Fermi surface around the M_2 point.

case of two monopoles and antimonopoles, symmetrically distributed around a TRIM \mathbf{k}_Γ , the Fermi arcs are formed between monopole-antimonopole pairs, as exemplified in Fig. 3.3. Suppose then we change some parameter in the system. Due to topological nature of Weyl nodes, the monopoles and antimonopoles move in the two-dimensional surface BZ. Eventually, they may undergo some pair annihilations, which occur symmetrically with respect to the TRIM \mathbf{k}_Γ ; the bulk bands become gapped. If a pair annihilation occurs for a pair connected by a Fermi arc, the Fermi arc eventually vanishes and the surface becomes gapped. On the other hand, if the pair annihilation occurs between a monopole and an antimonopole, which are not connected to each other by the Fermi arc, the pair annihilations will make all the Fermi arcs into a single loop encircling the TRIM \mathbf{k}_Γ . This loop constitutes a Dirac cone around the TRIM.

From the viewpoint of the change of the \mathbb{Z}_2 topological number and associated surface states (see Sec. 2.2.4 for details), the evolution of the surface states accompanying the WTI-STI topological phase transition occurs in the following way. When the inversion-symmetry is broken, there should generally arise a WSM phase between the WTI-STI phase transition. In the WTI-WSM phase transition, two pairs of Weyl nodes are created close to a TRIM \mathbf{k}_Γ [8]. As the system enters the WSM phase, a Fermi arc is formed between the two Weyl nodes within each pair. Thus there are two Fermi arcs which are symmetric with respect to the TRIM. As a control parameter is changed, the Fermi arcs grow as the Weyl nodes travel around the TRIM. Eventually, at the WSM-STI phase transition, the four Weyl nodes annihilate pairwise, causing a fusion of two Fermi arcs into a single Dirac cone encircling the TRIM, as shown in Fig. 3.5

As discussed in Sec. 2.1.5, when inversion symmetry is preserved, a \mathbb{Z}_2 topological index $\tilde{\pi}_a$ defined for each surface TRIM indicates whether the focused surface TRIM is inside or outside the surface Fermi surface [37]. It is also concluded that this index depends on the surface termination. Within this argument in Ref. [37], the surface should include the inversion center, and therefore there are two possible surface terminations for a fixed surface orientation. If we change one surface termination into the other, surface TRIM which were inside the Fermi surface will become outside the Fermi surface, and vice versa. We now try to apply this scenario to our model. However, the inversion symmetry is broken in our model, and the discussion in Ref. [37] is not directly applied. Nevertheless, we can expect the similar physics from continuity argument, by switching on the inversion-symmetry breaking. For example, in Figs. 3.6 (a1) and (b1), we show the Fermi surface on the (111) surface with the surface terminated with the atoms, each of which has three bonds along $\bar{1}\bar{1}\bar{1}$, $\bar{1}\bar{1}\bar{1}$, and $\bar{1}\bar{1}\bar{1}$. In this surface termination, the top surface is terminated by atoms in the A sublattice, and the bottom surface by atoms in the B sublattice. By adding bonds (i.e., “dangling bonds”) along 111 directions to the topmost atoms, we can switch from one surface termination to the other, namely the top and the bottom surfaces terminated by B and A sublattices, respectively. The results are plotted in Figs. 3.6 (a2) and (b2), whose parameters are identical with (a1) and (b1), respectively. We can see that the physics discussed in Ref. [37] carries over to the present model as well. For example, the M_1 and M_3 points are inside the Fermi surfaces when the dangling bonds are absent (Figs. 3.6(a1) and (b1)), but when the dangling bonds are added, the Fermi surfaces around the M_1 and M_3 points disappear (Figs. 3.6(a2) and (b2)). On the other hand, there appear a new Fermi surface around the Γ point when the dangling bonds are added. The remarkable phenomenon occurs around the M_2 point. The Fermi surface around the M_2 point in the STI phase in (b1) disappears in the plot (b2) where the dangling bonds are present. This also affects the neighboring WSM phase, as can be seen by comparing (a1) and (a2). Among the Weyl nodes in (a1) the Fermi arcs arise between W_{1+} - W_{1-} and between W_{2+} - W_{2-} . Meanwhile in (a2), the Fermi arcs arise between W_{1+} - W_{2-} and between W_{2+} - W_{1-} . Thus we have shown that the change of surface termination exchanges the pairs of Weyl nodes, out of which the Fermi arcs are formed.

This change of pairing of Weyl nodes by varying surface terminations occurs in generic WSMs. The Dirac cones in TIs depend on surface terminations, as shown in Ref. [37]. Because the WSM phase is next to the TI phase [8, 53], the dependence on the surface termination in general WSMs (with time-reversal symmetry) follows from that in the TIs, as we discussed in this paper. When the surface termination is varied, the pairing of the Weyl nodes will change, and the union of the pairing of the Weyl nodes before and after the change of surface termination forms a loop, which turns out to be the surface Fermi surface in the TI phase around a particular TRIM. In the present case, the pairing is $\{(W_{1+}, W_{1-}), (W_{2+}, W_{2-})\}$ or $\{(W_{1+}, W_{2-}), (W_{2+}, W_{1-})\}$, depending on the surface termination, and their union forms a loop around the M_2

point. This also implies that the pairing of the Weyl nodes for the Fermi arc is not solely determined from bulk band structure, because it depends on surface terminations.

3.3 Conclusion

In the present chapter, we study dispersions of Fermi arcs in the Weyl semimetal phase. We first construct a simple effective model, describing the Weyl semimetal with two Weyl nodes close to each other. We find that the dispersions of Fermi-arc states for top and bottom surfaces cross around the Weyl point, and they have opposite velocities. These Fermi-arc dispersions are tangential to the bulk Dirac cones around the Weyl points. These results are confirmed by a calculation using a tight-binding model with time-reversal symmetry but without inversion symmetry. In this model calculations, we see that the Fermi arcs gradually grow by changing a model parameter, and that two Fermi arcs finally merge together to form a single Dirac cone when the system transits from the Weyl semimetal to the topological insulator phase. We also find that by changing the surface termination, the pairing between the two monopoles and two anti-monopoles to make Fermi arcs is switched. These results reveal an interesting interplay between the surface and the bulk electronic states in Weyl semimetals and topological insulators.

Chapter 4

Topological phase transition of spinless topological semimetals

In this chapter, we study a generic topological phase transition from a topological nodal-line (TNL) semimetal (SM) to a spinless Weyl semimetal (WSM). To elucidate the phase transition, we classify TNLs into two types, type-A and type-B. The type-A and type-B TNLs are distinguished by their locations and shapes, which roughly corresponds to whether or not the TNLs enclose a time-reversal invariant momentum (TRIM). We show that, depending on the type of the TNL, its topological nature and its evolution under symmetry-breaking perturbations are quite varied. It is shown that the type-A TNLSM phase always becomes the spinless WSM phase when the time-reversal symmetry is broken. Furthermore, we show how other crystallographic symmetries constrain positions of the TNLs in the type-A TNLSMs. As a result, even if the inversion symmetry is broken, the system remains in a nontrivial topological semimetal phase by the crystal symmetries in many cases. We also demonstrate the phase transition between the TNLSM phase and the WSM phase by using a lattice model to confirm our theory.

This chapter is organized as follows. We classify the topological nodal line into the type-A and the type-B TNLSMs and show corresponding effective models in Sec. 4.1. In Sec. 4.2, we show general phase transitions in TNLSMs when the time-reversal or inversion symmetry is broken. We elucidate effects of other crystal symmetries on band structures and nodal lines of the topological semimetals in Sec. 4.3. In Sec. 4.4, we discuss phase transitions in TNLSMs with additional crystallographic symmetries, when the time-reversal or the inversion symmetry is broken. Our results are summarized in Sec. 4.5.

4.1 Classification of TNLSMs into two types

In this section we classify TNLSs into two types: type-A and type-B. We consider systems with inversion and time-reversal symmetries, whose operators are denoted by P and Θ , respectively. Θ is a complex conjugation operator K . These symmetries give constraints $H(-\mathbf{k}) = PH(\mathbf{k})P^{-1} = \Theta H(\mathbf{k})\Theta^{-1}$, where $H(\mathbf{k})$ is the Hamiltonian. Because of these symmetries, it is important to describe behaviors of the energy bands at a TRIM.

We classify TNLSs based on their shapes around one of the TRIM. Because of the time-reversal symmetry, TNLSs appear symmetrically with respect to TRIM. When there are more than one TNLS in the Brillouin zone, we consider each TNLS separately. It may sometimes happen that a single TNLS is not time-reversal invariant in itself, i.e. it is not symmetric with respect to the TRIM considered; in such cases, we consider instead a pair of TNLSs which is symmetric with respect to the TRIM, as shown in Fig. 4.1(b). Obviously, this pairing of TNLSs is independent of the choice of the TRIM. It may also happen that some TNLSs may traverse across the Brillouin zone, like an “open orbit” of an electron under a magnetic field within semiclassical theory. Our theory also works in such cases.

To classify individual TNLSs, we first define a time-reversal invariant plane, as a plane in \mathbf{k} space containing the TRIM considered. This plane is invariant under the time-reversal symmetry. Since the TNLSs are symmetric with respect to the TRIM, the TNLS always intersects with the time-reversal invariant plane $2(2N + 1)$ or $4N$ times, where N is a non-negative integer (Fig. 4.1). If the TNLS intersects with the time-reversal-invariant plane $2(2N + 1)$ times, the TNLS encloses the TRIM as shown in Fig. 4.1(a), and we call the TNLS a type-A TNLS. On the other hand, if the number of the intersection points is $4N$, we call the TNLS a type-B TNLS as shown in Fig. 4.1(b). If the TNLSs are tangential to the time-reversal invariant plane, we slightly move the time-reversal-invariant plane to eliminate the points of tangency, and count the number of intersections. This classification is independent of the choice of the time-reversal invariant plane for the fixed choice of the TRIM. Furthermore, it is also independent of the choice of the TRIM, which can be directly shown by considering a time-reversal invariant plane containing more than one TRIM.

In the following, we construct a two-band effective Hamiltonian consisting of the conduction and the valence bands around the TRIM, in order to facilitate our understanding of the behaviors of the TNLSs. To construct an effective Hamiltonian we assume that each TNLS is isolated, meaning that we can take a vicinity of the TRIM which contain only one TNLS. First, we consider the case where the parity eigenvalues of the conduction and the valence bands are different at the TRIM, and are inverted from the other TRIM. As we see later, this corresponds to the type-A TNLS. Then the inversion symmetry is given by $P = \pm\sigma_z$, where $\sigma_{i=x,y,z}$ denote Pauli matrices acting on the space spanned by the conduction and the valence bands. Then, from the time-reversal and inversion symmetries, the effective Hamiltonian is

$$H_{\text{TNL}}(\mathbf{q}) = a_y(\mathbf{q})\sigma_y + a_z(\mathbf{q})\sigma_z, \quad (4.1)$$

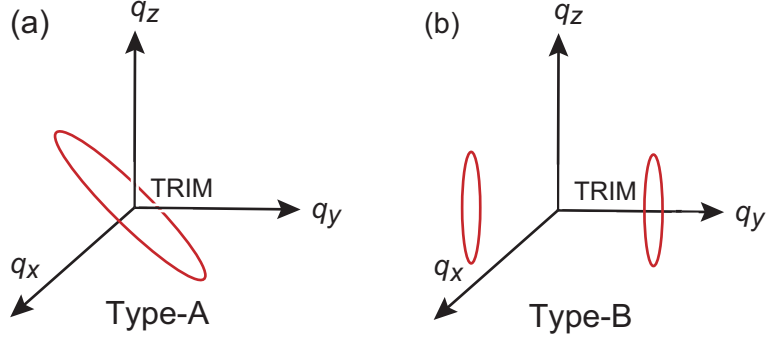


Figure 4.1: Schematic drawing of (a) type-A and (b) type-B TNLs. (a) When a type-A TNL encloses the TRIM, the type-A TNL intersects with any of the TR-invariant planes including the TRIM $2(2N + 1)$ times. (b) A type-B TNL intersects with the TR-invariant plane $4N$ times.

where \mathbf{q} is a wavevector measured from the TRIM, $a_y(-\mathbf{q}) = -a_y(\mathbf{q})$, and $a_z(-\mathbf{q}) = a_z(\mathbf{q})$. Therefore, the TNL is represented by $a_y(\mathbf{q}) = 0$ and $a_z(\mathbf{q}) = 0$. Here, we are considering the case where the parities of the bands at the TRIM are inverted from those at other TRIM. Therefore, the coefficient $a_z(\mathbf{q})$ changes sign as we go away from the TRIM ($\mathbf{q} = 0$). Hence, the equation $a_z(\mathbf{q}) = 0$ defines a closed surface encircling the TRIM, and together with the other condition $a_y(\mathbf{q}) = 0$, it indeed defines a TNL enclosing the TRIM, corresponding to the type-A TNL. In this case, a sign of a parameter m defined by $m \equiv a_z(\mathbf{q} = 0)$ describes whether the bands are inverted or not. Suppose we start from the TNLSM phase and change this parameter m across zero. As m approaches zero, the nodal line shrinks. At $m = 0$ the gap closes at the TRIM ($\mathbf{q} = 0$), and then the gap opens.

In addition, some of the type-B TNLs can also be described by Eq. (4.1). It happens when the sign of $a_z(\mathbf{q})$ at $\mathbf{q} = 0$ and that away from $\mathbf{q} = 0$ are the same, whereas $a_z(\mathbf{q})$ vanishes at some \mathbf{q} . This corresponds to the type-B TNL, by counting the number of intersections between the TNL and the TR-invariant plane.

Second, when the parity eigenvalues of the conduction and the valence bands are identical at the TRIM, $P = \pm\sigma_0$ and the effective Hamiltonian is

$$H_{\text{TNL}}(\mathbf{q}) = a_x(\mathbf{q})\sigma_x + a_z(\mathbf{q})\sigma_z, \quad (4.2)$$

where $a_x(-\mathbf{q}) = a_x(\mathbf{q})$ and $a_z(-\mathbf{q}) = a_z(\mathbf{q})$. TNLs exist if $a_x(\mathbf{q}) = 0$ and $a_z(\mathbf{q}) = 0$. It is straightforward to see that the number of intersections between the TNL and the TR-invariant plane is $4N$, meaning that this TNL is of type B. Unlike Eq. (4.1), the gap closing at the TRIM is prohibited by level repulsion. Meanwhile, as we explained later, the TNL can be annihilated without crossing the TRIM.

In some cases, there are more than one TNLs in the Brillouin zone. Ca (calcium) has four type-A TNLs and Yb (ytterbium) without the spin-orbit coupling has six pairs of type-B TNLs [75]. Let n_A and n_B denote the number of type-A TNLs and that of type-B TNLs, respectively. Then one can relate these numbers with the \mathbb{Z}_2 topological invariants ν_i ($i = 0, 1, 2, 3$) introduced in Ref. [86]. The topological invariants are defined as

$$(-1)^{\nu_0} = \prod_{n_j=0,1} \prod_{m}^{occ.} \xi_m(\mathbf{\Gamma}_{n_1 n_2 n_3}), \quad (4.3)$$

$$(-1)^{\nu_i} = \prod_{n_i=1, n_{j \neq i}=0,1} \prod_{m}^{occ.} \xi_m(\mathbf{\Gamma}_{n_1 n_2 n_3}), \quad (4.4)$$

where $\xi_m(\mathbf{\Gamma}_{n_1 n_2 n_3})$ is a parity eigenvalue of the m -th occupied band at a TRIM $\mathbf{\Gamma}_{n_1 n_2 n_3} = (n_1 \mathbf{G}_1 + n_2 \mathbf{G}_2 + n_3 \mathbf{G}_3)/2$, $n_i = 0, 1$. $\mathbf{G}_{i=1,2,3}$ are reciprocal vectors. (Equation (4.3) is the same as Eq. (2.55).) These topological invariants determine whether the number of intersections between the TNLs and a half of an arbitrary plane including four TRIM is even or odd [86]. In particular, it directly follows from Ref. [86] that

$$\nu_0 \equiv n_A \pmod{2}. \quad (4.5)$$

For example, both in Ca and Yb (without the the spin-orbit coupling), the \mathbb{Z}_2 topological numbers are trivial, i.e. $(\nu_0; \nu_1 \nu_2 \nu_3) = (0; 000)$ [75], and it agrees with the number of TNLs, $(n_A, n_B) = (4, 0)$ in Ca and $(n_A, n_B) = (0, 6)$ in Yb.

Next we consider an evolution of a TNL under continuous deformation of the system. A TNL may change its shape under the deformation, and sometimes the number of intersections with a time-reversal invariant plane may change. We first note that as long as the TNL does not go across the TRIM, the number of intersections between a TNL and a time-reversal invariant plane can change only by an integer multiple of four, because the TNL remains symmetric with respect to the TRIM. Therefore, a type-B TNL can shrink and be annihilated without crossing the TRIM, because $4N \equiv 0 \pmod{4}$. On the other hand, to annihilate a type-A TNL, it should go across the TRIM, and thereby the gap closes at the TRIM. From the argument of the \mathbb{Z}_2 topological numbers, in order to annihilate a type-A TNL, the \mathbb{Z}_2 topological number should change, and thus this gap closing should necessarily accompany an exchange of the parity eigenvalues at the TRIM between the valence and the conduction bands. This agrees with the argument in Eq. (4.1). If the two bands forming the TNL have the same parity eigenvalues, the gap closing at the TRIM is not allowed because of the level repulsion. Meanwhile, when the bands have opposite parity eigenvalues, there are no constraints for gap-closing points. We remark that one can change the numbers of type-A TNLs and type-B TNLs under continuous deformation of the system without changing the topological invariant ν_0 . For example, one can continuously deform from the TNLs in Ca to those in Yb via Lifshitz transitions, without changing ν_0 .

4.2 Phase transition involving TNLSMs

To elucidate phase transitions involving the TNLSM phase, we add symmetry-breaking perturbations to the system. We use the effective Hamiltonians for the TNLSMs described by Eqs. (4.1) and (4.2). We assume that the TNLs are realized before breaking the symmetry, and let ℓ denote the TNL. On the TNLs, $a_y(\mathbf{q}) = a_z(\mathbf{q}) = 0$ in Eq. (4.1) or $a_x(\mathbf{q}) = a_z(\mathbf{q}) = 0$ in Eq. (4.2) holds. In this section, we ignore crystallographic symmetries other than inversion symmetry.

4.2.1 Type-A TNLSMs with broken time-reversal symmetry

Firstly, we break the time-reversal symmetry in type-A TNLSMs. The allowed perturbation term is $a_x(\mathbf{q})\sigma_x$ which satisfies $a_x(-\mathbf{q}) = -a_x(\mathbf{q})$ because of the inversion symmetry. (Actually, small perturbations $\delta a_{y,z}(\mathbf{q})\sigma_{y,z}$ can be also added. However, since the terms do not change the number of the conditions determining structures of the gapless nodes, they change only the size of the TNL. Therefore, the terms $\delta a_{y,z}(\mathbf{q})\sigma_{y,z}$ are negligible.) We can assume that the perturbation is so small that the coefficients of Eq. (4.1) remain zero on ℓ after the time-reversal breaking. Thus, the gap closes when $a_x(\mathbf{q}) = 0$,³ $\mathbf{q} \subset \ell$ in the presence of the small time-reversal breaking term. In fact, such wavevectors satisfying $a_x(\mathbf{q}) = 0$ always exist somewhere on ℓ because $a_x(\mathbf{q})$ is an odd function of \mathbf{q} and the type-A TNL ℓ encloses the TRIM represented by $\mathbf{q} = 0$. The emergent gapless points are Weyl nodes [Fig. 4.2 (a)]. The Weyl nodes appear symmetrically with respect to the TRIM, and the minimal number of Weyl nodes is two. The two Weyl nodes are related by the inversion symmetry, and thus have opposite monopole charges. Hence, when the time-reversal symmetry is broken, the system changes from the type-A TNLSM phase to the spinless WSM phase.

We also show another proof of the appearance of the spinless WSM phase by breaking the time-reversal symmetry based on a topological description. We assume that a type-A TNL encloses a TRIM Γ , and that the energy bands are gapless only on the TNL. We consider a time-reversal invariant plane P_Γ which includes Γ . The time-reversal invariant plane has $2(2N + 1)$ intersection points $\pm \mathbf{k}_i (i = 1, \dots, 2N + 1)$ with the type-A TNL. We focus on pairs of the gapless points on P_Γ , which are related by the inversion symmetry. Because the closings of the gap at these gapless points are protected topologically by the time-reversal and inversion symmetries, the bands generally become gapped at these points when we weakly break the time-reversal symmetry. The perturbation terms obtained in each pair $\pm \mathbf{k}_i$ have opposite signs, because of the inversion symmetry. Thus, the bands at each pair of wavevectors $\pm \mathbf{k}_i$ contribute by $+1$ or -1 to the Chern number defined on the plane P_Γ [20]. By summing over all the $(2N + 1)$ pairs, the Chern number on the plane P_Γ is nonzero. On the other hand, we introduce another plane $P_{\Gamma\parallel}$ which is parallel to P_Γ , but does not intersect nodal lines [Fig. 4.2 (b)]. By assumption, the Chern number defined on $P_{\Gamma\parallel}$ is zero before introducing the perturbation. As long as the perturbation

is small, the band gap does not close on the plane $P_{\Gamma\parallel}$, and the Chern number remains zero on $P_{\Gamma\parallel}$ after the time-reversal symmetry is broken. Therefore, the Chern numbers are different between P_{Γ} and $P_{\Gamma\parallel}$, which means that between P_{Γ} and $P_{\Gamma\parallel}$ the energy bands should have gapless points, i.e. Weyl nodes. As a consequence, the WSM phase necessarily emerges from the type-A TNLSM phase by breaking the time-reversal symmetry.

4.2.2 Type-A TNLSMs with inversion-symmetry breaking

Secondly, we introduce a term which weakly breaks the inversion symmetry but preserves the time-reversal symmetry in type-A TNLSMs. The allowed term is described by $a_x(\mathbf{q})$ which satisfies $a_x(-\mathbf{q}) = a_x(\mathbf{q})$. Then, $a_x(\mathbf{q})$ can be nonzero on the whole loop ℓ since $a_x(\mathbf{q})$ is an even function of \mathbf{q} . Therefore, the energy bands can become gapped. It is natural from the viewpoint of topology; because the perturbation terms obtained in each pair $\pm\mathbf{k}_i$ have the same signs, the Chern number on the plane P_{Γ} is zero, implying that there appear no gapless points in general.

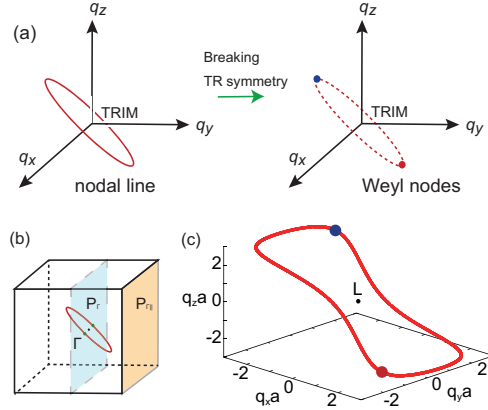


Figure 4.2: (a) Schematic drawing of the band evolution. The red solid line is the TNL around the TRIM. The blue and the red points are the spinless Weyl nodes left on the loop ℓ (red dashed line). The difference between colors of the Weyl nodes corresponds to opposite monopole charges. (b) Schematic drawing of the type-A TNL and the time-reversal invariant planes. The red line is the type-A TNL. The blue and orange regions represent P_{Γ} and $P_{\Gamma\parallel}$, respectively. The green dots are the intersection points of the type-A TNL and P_{Γ} . (c) Change of the band structure from the type-A TNL to the spinless Weyl nodes in a lattice model. The axes represent wavevectors measured from the point L . The red loop is the type-A TNL around the L point when $t_{\tau}/t_{\delta_1} = 1.4$, $t_{\delta_2}/t_{\delta_1} = 1.1$, $t_{\delta_3}/t_{\delta_1} = 0.9$, and $t/t_{\delta_1} = 0.1$. The blue and red dots are the Weyl nodes which appear from the type-A TNL for the finite time-reversal breaking $\phi = 0.1$.

4.2.3 Type-B TNLSMs with broken time-reversal or inversion symmetry

Next, we study a phase transition of the type-B TNLSM phase by breaking the time-reversal or inversion symmetry. The additional perturbation term for Eq. (4.1) and (4.2) for breaking either of the time-reversal or inversion symmetries is $a_x(\mathbf{q})\sigma_x$ and $a_y(\mathbf{q})\sigma_y$, respectively. Now the perturbation is generally nonzero everywhere on ℓ , whichever symmetry is broken. Even if the perturbation term is an odd function of \mathbf{q} , it can be nonzero on ℓ because the type-B TNLs do not enclose the TRIM, unlike the type-A TNLs. Therefore, in general, by breaking the time-reversal or inversion symmetry, a gap opens, and the WSM phase does not appear from the type-B TNLSM phase.

4.2.4 Phase transition in a lattice model

In this subsection, we see a phase transition from the type-A TNLSM phase to the spinless WSM phase by using a lattice model, and we see agreement with the discussion in Sec. 4.2.1. We use a model on a diamond lattice given by

$$H = \sum_{\langle ij \rangle} t_{ij} c_i^\dagger c_j + \sum_{\ll ij \gg} t'_{ij} c_i^\dagger c_j. \quad (4.6)$$

The first term represents nearest-neighbor hoppings between the sublattices A and B. Here, we denote the three translation vectors by $\mathbf{t}_1 = \frac{a}{2}(0, 1, 1)$, $\mathbf{t}_2 = \frac{a}{2}(1, 0, 1)$, and $\mathbf{t}_3 = \frac{a}{2}(1, 1, 0)$, where a is a lattice constant. Then, the four nearest-neighbor bonds are $\boldsymbol{\tau} = \frac{a}{4}(1, 1, 1)$, and $\boldsymbol{\delta}_{i=1,2,3} = \boldsymbol{\tau} - \mathbf{t}_{i=1,2,3}$. We express the hoppings in the direction of $\boldsymbol{\delta}$ as subscripts. For example, the hoppings in the direction of $\boldsymbol{\tau}$ and $\boldsymbol{\delta}_{i=1,2,3}$ are written by $t_{\boldsymbol{\tau}}$ and $t_{\boldsymbol{\delta}_{i=1,2,3}}$, respectively. The second term represents the next nearest-neighbor hoppings. The twelve next nearest-neighbor bonds are represented by $\pm \mathbf{t}_{i=1,2,3}$, and $\pm \mathbf{u}_{i=1,2,3}$, where $\mathbf{u}_1 = \mathbf{t}_3 - \mathbf{t}_2$, $\mathbf{u}_2 = \mathbf{t}_3 - \mathbf{t}_1$, and $\mathbf{u}_3 = \mathbf{t}_1 - \mathbf{t}_2$. In addition, we denote the next nearest-neighbor hoppings between the same sublattices A(B) by $t_{\boldsymbol{\delta}}'^{A(B)}$. When the system is inversion-symmetric, $t_{\boldsymbol{\tau}}$ and $t_{\boldsymbol{\delta}_{i=1,2,3}}$ are real, and $t_{\boldsymbol{\delta}}'^A = (t_{\boldsymbol{\delta}}'^B)^*$. The Hamiltonian in the momentum space is

$$H(\mathbf{k}) = \left[2 \sum_{\mathbf{d}} \text{Re}[t_{\mathbf{d}}'^A] \cos \mathbf{k} \cdot \mathbf{d} \right] \sigma_0 + \left[t_{\boldsymbol{\tau}} + \sum_i t_{\boldsymbol{\delta}_i} \cos \mathbf{k} \cdot \mathbf{t}_i \right] \sigma_x \\ + \left[\sum_i t_{\boldsymbol{\delta}_i} \sin \mathbf{k} \cdot \mathbf{t}_i \right] \sigma_y + \left[2 \sum_{\mathbf{d}} \text{Im}[t_{\mathbf{d}}'^A] \sin \mathbf{k} \cdot \mathbf{d} \right] \sigma_z, \quad (4.7)$$

where \mathbf{d} in the sum runs over $\mathbf{t}_{i=1,2,3}$ and $\mathbf{u}_{i=1,2,3}$. The Pauli matrices $\sigma_{i=0,x,y,z}$ act on the sublattice degree of freedom. In this model, the parity operator is represented by $P = \sigma_x$. Then, the parity eigenvalues ξ of the occupied bands at the TRIM $\Gamma_{n_1 n_2 n_3}$ are given by

$$\xi(\Gamma_{n_1 n_2 n_3}) = -\text{sgn} \left[t_{\boldsymbol{\tau}} + \sum_i t_{\boldsymbol{\delta}_i} (-1)^{n_i} \right]. \quad (4.8)$$

The topological invariant ν_0 is obtained from $(-1)^{\nu_0} = \prod_{n_j=0,1} \xi(\mathbf{\Gamma}_{n_1 n_2 n_3})$.

When $t_{\delta}^{\prime A(B)}$ are real i.e. $\text{Im}[t_{\delta}^{\prime A}] = 0$, the model has TR symmetry, which case has been studied in Ref. [137]. In Ref. [137], it is shown that the energy bands can have a type-A TNL around the TRIM $\mathbf{\Gamma}_{111} = L = \frac{\pi}{a}(1, 1, 1)$. The type-A TNL exists when the parity eigenvalue $\xi(\mathbf{\Gamma}_{111})$ is opposite from those at the other TRIM. To realize it, we set $t_{\tau}/t_{\delta_1} = 1.4$, $t_{\delta_2}/t_{\delta_1} = 1.1$, and $t_{\delta_3}/t_{\delta_1} = 0.9$. We also assume that all the second nearest neighbor hopping are identical, having the values $t_{\delta}^{\prime A}/t_{\delta_1} = 0.1$. Since all the nearest-neighbor hoppings are different and real, the model has only time-reversal and inversion symmetries. Then, the type-A TNL appears around the L point as seen in Fig. 4.2 (c), which is as expected from our argument in Sec. 4.2.1.

Next we break the time-reversal symmetry by adding finite imaginary parts of $t_{\delta}^{\prime A}$. For example, this time-reversal breaking can be included as Peierls phases from magnetization. We put $t_{\mathbf{d}}^{\prime A} = t e^{i\phi}$ for the next nearest-neighbor hoppings represented by $\mathbf{d} = \mathbf{t}_{i=1,2,3}$ and $\mathbf{u}_{i=1,2,3}$, where t and ϕ are real constants. Then, $t_{\mathbf{d}}^{\prime A} = t e^{-i\phi}$ when $\mathbf{d} = -\mathbf{t}_{i=1,2,3}$ and $-\mathbf{u}_{i=1,2,3}$. In order to break the time-reversal symmetry, we put $t/t_{\delta_1} = 0.1$ and $\phi = 0.1$ for instance. Consequently, we find that a topological phase transition occurs from the type-A TNLSM phase to the spinless WSM phase. Figure 4.2 (c) shows the two Weyl nodes which emerge from the type-A TNL.

Instead of the TR-breaking, we can break the I symmetry by adding an on-site staggered potential given by $H_{IB} = M_s \sum_i \lambda_i c_i^{\dagger} c_i$, where λ_i takes values $+1$ for the A sublattices and -1 for the B sublattices. Then, we can directly see that the type-A TNL becomes gapped.

4.3 Crystal symmetries and band structures of type-A TNLSMs

In Sec. 4.2, we discussed the TNLSMs by considering only time-reversal and inversion symmetries. In this section, we also take account into twofold rotational (C_2) and mirror (M) symmetries, because $C_2 M$ is equal to the space inversion. Particularly, we show how the two symmetries, C_2 and M , constrain band structures having type-A TNLs.

4.3.1 Band structures of the type-A TNLSMs

Now, we classify the type-A TNLs into two cases according to whether or not the TRIM which the TNLs enclose is invariant under C_2 and M symmetries. Because $P = C_2 M$, in inversion-symmetric systems, a little group of the TRIM often contains C_2 and M symmetries in pairs. If the TRIM is not invariant under the two symmetries, we call this case (I). When the TRIM considered is invariant under C_2 and M , we call the case (II). Here, twofold screw symmetries and glide symmetries can be treated similarly to C_2 and M symmetries, respectively, and the systems with these symmetries can be included in the case (II), except for

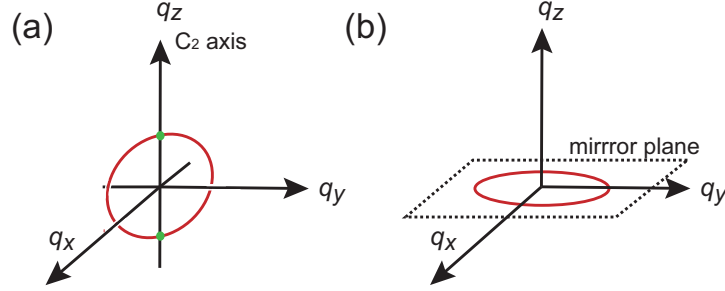


Figure 4.3: Schematic positions of the nodal lines in the type-A TNL around the TRIM. (a) The type-A TNL for the case (i) has the intersection points with the C_2 invariant axis, which are indicated by the green dots. (b) For the case (ii), the type-A TNL appears on the mirror-invariant plane.

some special cases at the Brillouin zone boundary for nonsymmorphic space groups (see the Appendix A). Actually, the case (II) is more important for application to real materials because 89 space groups of all the 92 space groups with inversion symmetry have the two symmetries [138].

In fact, the band structures and the phase transition of the type-A TNLSMs for (I) have already been studied in Secs. 4.1 and 4.2, because there is no additional symmetry which further constrains the phase transition. For example, CaP_3 [90] is included in the case (I).

In the case (II), the two symmetries C_2 and M give some constraints to the effective Hamiltonian described by Eq. (4.1). Since the parity eigenvalues are different for the conduction and the valence bands of the type-A TNLSs, either of the C_2 or the M symmetry has different eigenvalues for the conduction and the valence bands. In spinless systems, eigenvalues of the C_2 and the M symmetries take values ± 1 . Then, because $P = MC_2$, there are two cases for combinations of eigenvalues C_2 and M at the TRIM; (II)-(i) eigenvalues of M are the same and those of C_2 are different, and (II)-(ii) eigenvalues of M are different and those of C_2 are the same. They correspond to two different matrix representations: (II)-(i) $M = \pm\sigma_0$ and $C_2 = \pm\sigma_z$, and (II)-(ii) $M = \pm\sigma_z$ and $C_2 = \pm\sigma_0$. We can calculate the band structures for these cases, and the details are shown in the Appendix A. The resulting positions of the nodal lines are shown in Fig. 4.3, where we set the twofold rotational axis and the mirror plane to be the z axis and xy plane, respectively. For (II)-(i), as seen in Fig. 4.3 (a), the type-A TNL encircles the TRIM and intersects the C_2 -invariant axis. The TNL is symmetric with respect to the mirror plane $q_z = 0$. For (II)-(ii), the type-A TNL appears on the mirror-invariant plane as shown in Fig. 4.3 (b).

4.3.2 Applications of the theory of the band structures to the candidate materials of TNLSMs

The results in the previous subsection can be easily generalized to little groups with many different pairs of C_2 and M symmetries. We apply the theory to several candidates of the type-A TNLSMs. First, we consider fcc Ca, whose space group is No. 225 [75]. Ca have four type-A TNLs near each of the four TRIM L . The little group at the L points is D_{3d} which contains three C_2 -rotational operations. The two bands forming the TNLs belong to A_{1g} and A_{2u} states at the point L , and they have different C_2 eigenvalues. Therefore, the TNLs in Ca intersect the L - W lines, which are the C_2 invariant axes but do not lie on mirror planes, in accordance with our theory.

Next, we apply the theory to Cu_3ZnN [86]. The space group of Cu_3ZnN is No. 221. The energy bands have type-A TNLs around the three TRIM X , whose little groups are D_{4h} . The type-A TNLs are formed by A_{2u} and A_{1g} states at the X points. The D_{4h} group contains a fourfold-rotational (C_4) operation, four C_2 operations whose rotational axes are normal to the principal axis, and the corresponding five mirror operations. Then, the A_{2u} and A_{1g} states have opposite eigenvalues of the four C_2 symmetries. Thus, the TNLs cross the X - M lines and X - R lines, which are the C_2 -invariant axes. Meanwhile, the two states have the same eigenvalues of the C_4 symmetry. Hence, $C_4 = \sigma_0$ leads to different eigenvalues of the mirror symmetry $M = P(C_4)^2 = \sigma_z$. Therefore, the TNLs also appear on the mirror-invariant plane normal to the C_4 -invariant axis. As a result, the type-A TNLs in Cu_3ZnN not only cross the C_2 -invariant axes but also exist on the mirror plane.

Last, we remark that the type-A TNLs are predicted to appear on the mirror planes in many candidates such as $\text{Cu}_3(\text{Pd}, \text{Zn})\text{N}$ [86, 87], Ca_3P_2 [83, 84], LaN [88], and compressed black phosphorus [89]. They belong to (II)-(ii) and the existence of TNLs is understood from the difference in eigenvalues of M between the conduction and valence bands.

4.4 Phase transitions of type-A TNLSMs and crystal symmetries

In this section, we show that for type-A TNLSMs in the case (II), the presence of C_2 and M symmetries changes phase transitions when we break time-reversal or inversion symmetry.

4.4.1 Type-A TNLs protected by crystal symmetries with broken time-reversal symmetry

Here, we break the time-reversal symmetry in the type-A TNL. When energy bands cross on high-symmetry lines or planes, and have different eigenvalues of crystal symmetries, the band crossing is protected by the symmetries. Therefore,

such degeneracy remains on high-symmetry lines or planes, even when the time-reversal symmetry is broken. Therefore, in the case (II)-(i), where the type-A TNL crosses the C_2 -invariant axis, the time-reversal breaking creates Weyl nodes on the C_2 -invariant axis as shown in Fig. 4.4. In the effective model, the protection originates from the fact that the perturbation $a_x(0, 0, q_z)$ always vanishes on the C_2 axis.

Next, in the case (II)-(ii), where the type-A TNL is always on the mirror-invariant plane, the nodal line remains on the mirror plane even without the time-reversal symmetry. In the effective 2×2 model, it is seen from the fact that the perturbation $a_x(q_x, q_y, 0)$ vanishes on the mirror plane. In particular, one needs to break the M symmetry in order to realize the WSM phase.

4.4.2 Type-A TNLs protected by crystal symmetries with inversion-symmetry breaking

We study effects of the inversion breaking for the case (II) in this subsection. In the case (II), where the system has C_2 and M symmetries, violation of the inversion symmetry is equivalent to breaking either C_2 or M symmetry because $P = MC_2$. Therefore, the topological semimetal phases may survive in a different way between (II)-(i) and (II)-(ii).

First, we consider the case (II)-(i). When the type-A TNL intersects C_2 -invariant axes, the system becomes a spinless WSM phase by breaking the inversion symmetry while retaining the C_2 symmetries. Then, we obtain Weyl nodes not only on the C_2 invariant axes but also on the ΘC_2 -invariant plane ($q_z = 0$), because of the symmetry protection. In the effective model, $\Theta C_2 = K\sigma_z$ symmetry leads to $a_x(q_x, q_y, 0) = 0$, meaning that the perturbation is absent on this ΘC_2 -invariant plane. Here, within each pair of nodes related by the time-reversal symmetry, monopole charges are the same. The four nodes correspond to the minimal number of Weyl nodes in time-reversal invariant WSMs [8]. In fact, the appearance of four Weyl nodes can be understood by expanding the inversion-breaking perturbation term proportional to σ_x . The term expanded near the TRIM to the lowest order is $a_x(\mathbf{q}) = (\alpha q_x + \beta q_y)q_z$. Therefore, we can see that the Weyl nodes appear when either $q_z = 0$ or $q_x = q_y = 0$ is satisfied, giving the four Weyl nodes.

On the other hand, for the case (II)-(ii) of the type-A TNLs on the mirror plane, if we leave the M symmetry and break the C_2 symmetry, the nodal line survives because of the M symmetry. The mirror symmetry protects the nodal lines regardless of existence of the inversion symmetry. Hence, even if the inversion symmetry is broken, the nodal line remains unless the mirror symmetry is broken.

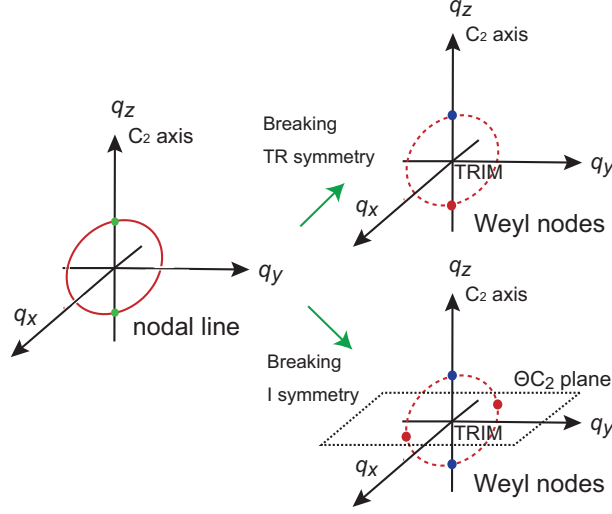


Figure 4.4: Realization of the spinless Weyl nodes by breaking the time-reversal or the inversion symmetry in the case (II). The blue and the red points represent the Weyl nodes. If the time-reversal symmetry is broken, the Weyl nodes appear on the C_2 invariant axis. When the inversion symmetry is broken, we obtain a pair of Weyl nodes on the C_2 -invariant axis and another pair on the ΘC_2 -invariant plane.

4.5 Conclusion and discussion

In the present chapter, we study phase transitions and band evolutions of topological nodal-line semimetals. We classified topological nodal-line semimetals into type-A and type-B in order to describe general phase transitions by breaking time-reversal or inversion symmetry. This classification is based on the geometrical positions of the nodal lines, and we give effective Hamiltonians for each case for analysis of symmetry breaking. The results show that the topological nodal lines enclosing a TRIM (type-A topological nodal lines) always become Weyl nodes when the time-reversal symmetry is broken. However, breaking of inversion symmetry opens a band gap in the type-A topological nodal-line semimetals, and it is confirmed by our calculation on the lattice model. On the other hand, it is shown that the type-B topological nodal lines, which do not enclose a TRIM, become gapped by breaking time-reversal symmetry. The two types are distinguishable from the shapes of the topological nodal lines.

We also showed how band structures of type-A topological nodal lines are determined by the little group at the TRIM. When the topological nodal line encircles the TRIM, which is invariant under C_2 and M symmetries of the system, they cross the C_2 -invariant axis and/or appear on the mirror-invariant

plane, and consequently are protected by the symmetries. Therefore, the nodal lines or points survive in some cases, even when the time-reversal or the inversion symmetries is broken. The revealed properties are also useful to search spinless topological semimetals in many materials because many space groups with inversion symmetry have various C_2 and M symmetries. As a result, the spinless WSMs can be predicted in many candidates of the topological nodal-line semimetals protected by the C_2 symmetries when we break the inversion symmetry.

Our study tells us how to realize a spinless WSM phase. In electronic systems, the spinless WSM phase appear from the type-A topological nodal-line semimetal phases not only by a circularly polarized light [110–115] but also by magnetic ordering, an external electric field, structural transition, and so on. Moreover, our theory can be applied to spinless fermions in cold atoms and bosonic bands. This can be potentially realizable in bosonic metamaterials of photons and phonons where lattice structure and its symmetry are flexibly controllable.

Chapter 5

General phase transition of Weyl superconductivity in mirror-symmetric superconductors

In this chapter, we study topological phase transitions in three-dimensional odd-parity and noncentrosymmetric superconductors with mirror symmetry when time-reversal symmetry is broken. We construct a generic phase diagram for Weyl superconductivity in the mirror-symmetric superconductors (SCs). It is shown that Weyl superconductivity generally emerges between the trivial and the topological crystalline superconductor phases. We demonstrate how a trajectory of the Weyl nodes determines the change of mirror Chern numbers in the topological phase transition. We also discuss a relationship between particle-hole symmetry and the Weyl-node trajectory which realizes the topological crystalline SC phase.

The chapter is organized as follows. In Sec. 5.1, we construct an effective Hamiltonian in order to discuss Weyl SCs in mirror-symmetric SCs. In Sec. 5.2, we study generic topological phase transition to give a universal phase diagram for Weyl SCs. Moreover, we give a model calculation to confirm our theory of the topological phase transition in Sec. 5.3. We also show evolution of the surface states in the topological phase transition in Sec. 5.4. We present our conclusion in Sec. 5.5.

5.1 Theory of gap closing in mirror-symmetric superconductors

To begin with, we construct an effective Hamiltonian to study the topological phase transition involving the Weyl SC phase because the gap closing is necessary for the Weyl nodes. We assume that all the bands are nondegenerate. Thus, we can describe a gap closing at $\mathbf{k} = \mathbf{k}_0$ by a two-band effective Hamiltonian. The behavior of the gap closing can be determined by symmetries which leave $\mathbf{k} = \mathbf{k}_0$ invariant [69]. In this section, we extend the theory of noncentrosymmetric semiconductor in Sec. 2.2.5 to time-reversal breaking SCs.

5.1.1 Gap closing in noncentrosymmetric SCs

In noncentrosymmetric SCs without time-reversal symmetry, a generic two-band effective Hamiltonian can be written by

$$H_{eff}(\mathbf{q}, m) = a_0(\mathbf{q}, m)\sigma_0 + a_1(\mathbf{q}, m)\sigma_1 + a_2(\mathbf{q}, m)\sigma_2 + a_3(\mathbf{q}, m)\sigma_3, \quad (5.1)$$

where $\mathbf{q} = \mathbf{k} - \mathbf{k}_0$, and m is a tunable parameter. Here, $\sigma_{0,1,2,3}$ are Pauli matrices, and $\sigma_3 = +1$ and -1 indicate the electron and the hole bands, respectively. Therefore, we can use the same discussion as that in Sec. 2.2.5. To investigate the gap closing, suppose that the gap is open within $m < m_0$, and that the gap closes at $\mathbf{q} = 0$ and $m = m_0$. The emergent gapless phase within $m > m_0$ varies, depending on difference between the number of variables and conditions for the gap closing, as discussed in Sec. 2.2.5. For example, we consider a gap closing at general points. Then, there is no constraint by symmetries on the effective Hamiltonian. Because we have four variables (\mathbf{q}, m) in the three-dimensional system, three conditions ($a_{1,2,3} = 0$) should be satisfied. Thus, if the gap closing occurs at $(\mathbf{q}, m) = (0, m_0)$, a pair of Weyl nodes is created [8, 53, 69].

Now because we consider the topological phase transition in mirror symmetric SCs, we need to clarify a behavior of a gap closing on the mirror plane. For simplicity, we assume that the mirror plane is the xy plane. Then, the effective Hamiltonian satisfies

$$\tilde{M}H_{eff}(q_x, q_y, -q_z, m)\tilde{M}^{-1} = H_{eff}(q_x, q_y, q_z, m), \quad (5.2)$$

where \tilde{M} is mirror operator in the SC.

The structures of the nodes after the gap closing on the mirror plane vary depending on mirror eigenvalues of the two states. If the two states have the same mirror eigenvalues, i.e., $\tilde{M} = \pm i\sigma_0$, Eq. (5.2) becomes $H_{eff}(q_x, q_y, -q_z, m) = H_{eff}(q_x, q_y, q_z, m)$. Thus, the gap closing is not affected by this condition on the mirror plane ($q_z = 0$). Therefore, Weyl nodes appear after the gap closing between the two states with the same mirror eigenvalues [69].

On the other hand, if the two states have the opposite mirror eigenvalues, i.e., $\tilde{M} = \pm i\sigma_3$, Eq. (5.2) is reduced to $\sigma_3 H_{eff}(q_x, q_y, -q_z, m)\sigma_3 = H_{eff}(q_x, q_y, q_z, m)$. As a result, we obtain $H_{eff}(q_x, q_y, 0, m) = a_0(q_x, q_y, 0, m)\sigma_0 + a_3(q_x, q_y, 0, m)\sigma_3$ on the mirror plane ($q_z = 0$). Hence, a line node appears on the mirror plane after the gap closing like normal states [69].

5.1.2 Gap closing in inversion-symmetric SCs

If SCs have inversion symmetry \tilde{P} , positive and negative energy states at \mathbf{q} are related by particle-hole symmetry C . Therefore, we need to take $C\tilde{P}$ symmetry into account when we construct the effective Hamiltonian of the inversion-symmetric SCs. The effective Hamiltonian also satisfies

$$C\tilde{P}H_{eff}(\mathbf{q})(C\tilde{P})^{-1} = -H_{eff}(\mathbf{q}). \quad (5.3)$$

We use the same notation as that in Sec. 2.3. Namely, we describe a relationship between crystal symmetry and particle-hole symmetry by using superscripts \pm of the symmetry operators.

Firstly, we consider odd-parity SCs. Since $(C\tilde{P}^-)^2 = -1$, $C\tilde{P}^- = -i\sigma_2 K$ can be chosen [139], which leads to $a_0(\mathbf{q}) = 0$. Then, the effective Hamiltonian becomes

$$H_{eff}(\mathbf{q}, m) = a_1(\mathbf{q}, m)\sigma_1 + a_2(\mathbf{q}, m)\sigma_2 + a_3(\mathbf{q}, m)\sigma_3. \quad (5.4)$$

From Eq. (5.4), the odd-parity SCs have the same conditions for the gap closing as the noncentrosymmetric SCs. Hence, we can apply the same discussion on the gap closing as used in Sec. 5.1.1. We note that the gap closes and the Weyl nodes appear at zero energy by $C\tilde{P}$ symmetry. In addition, we show that $C\tilde{P}$ symmetry determines mirror operator \tilde{M} which acts on the effective Hamiltonian. In mirror-symmetric SCs, the mirror symmetry satisfies $\tilde{M}^\eta C = \eta C\tilde{M}^\eta$. We assume that the positive-energy state $|E_+, \lambda\rangle$ has a mirror eigenvalue $\lambda = \pm i$ on the mirror plane. Then, the negative-energy state $C\tilde{P}|E_+, \lambda\rangle$ has a mirror eigenvalue $-\eta\lambda$ because

$$\tilde{M}^\eta C\tilde{P}|E_+, \lambda\rangle = \eta C\tilde{P}\tilde{M}^\eta|E_+, \lambda\rangle = -\eta\lambda C\tilde{P}|E_+, \lambda\rangle. \quad (5.5)$$

Thus, the mirror operation is represented as $\tilde{M}^\eta = \lambda \text{diag}(1, -\eta)$. In other words, when the gap function is mirror-odd (even), the mirror eigenvalues of the two states are the same (different). Hence, the gap closing on the mirror plane leads to pair creation of Weyl nodes in the odd-parity SCs with the mirror-odd gap function. This is consistent with the fact that each mirror sector has its own particle-hole symmetry in the mirror-odd SC. On the other hand, in the odd-parity SCs with the mirror-even gap function, a nodal line appears from the gap closing on the mirror plane.

Secondly, we construct the effective Hamiltonian for even-parity SCs. Then, $C\tilde{P}^+ = \sigma_1 K$ which yields $(C\tilde{P}^+)^2 = 1$ can be chosen [139]. Thus, because we obtain $H_{eff}(\mathbf{q}, m) = a_3(\mathbf{q}, m)\sigma_3$ from Eq. (5.1), there is one condition for the gap closing. As a result, the gap closing produces a surface node [116, 140–143]. This case is not treated in this thesis because we are interested in the Weyl SCs.

5.2 General phase transition of Weyl superconductivity in mirror-symmetric superconductors

We start with a brief introduction of a topological crystalline SC phase in order to discuss topological phase transitions in mirror-symmetric SCs. The details are in Sec. 2.3. If a Bogoliubov-de Gennes (BdG) Hamiltonian without time-reversal symmetry has a mirror symmetry, the system can realize a topological crystalline SC phase [121, 122, 129, 130, 144]. When the normal state is mirror-symmetric, the mirror symmetry is preserved in the BdG Hamiltonian if the gap function is mirror-odd or even, i.e. $M\Delta(\mathbf{k})M^t = \mp\Delta(\mathbf{k})$ on the mirror plane. M and $\Delta(\mathbf{k})$ are the mirror operation in the normal state and the gap function of the SC, respectively. The topological SC is characterized by a mirror Chern number [37]. The mirror Chern number $\nu^{(\lambda)}$ is a Chern number defined in the mirror sector of the mirror eigenvalue $\lambda = \pm i$ on the mirror plane. We denote the BdG Hamiltonian in the mirror sector of λ as $\mathcal{H}_\lambda(\mathbf{k})$. When the SC is gapped and some of mirror Chern numbers are nonzero, a topological crystalline SC is realized.

To define the mirror Chern number, we introduce Berry connection $\mathbf{A}^\lambda(\mathbf{k})$ and Berry curvature $\mathbf{F}^\lambda(\mathbf{k})$ in the mirror sector $\mathcal{H}_\lambda(\mathbf{k})$ given by [121]

$$\mathbf{A}^\lambda(\mathbf{k}) = i \sum_n \langle u_n^\lambda(\mathbf{k}) | \nabla_{\mathbf{k}} | u_n^\lambda(\mathbf{k}) \rangle, \quad (5.6)$$

$$\mathbf{F}^\lambda(\mathbf{k}) = \nabla_{\mathbf{k}} \times \mathbf{A}^\lambda(\mathbf{k}), \quad (5.7)$$

where $|u_n^\lambda(\mathbf{k})\rangle$ is the n -th eigenstate of the BdG Hamiltonian with the mirror eigenvalue λ . The sum in $\mathbf{A}^\lambda(\mathbf{k})$ is taken over the negative energy states. For example, we take the mirror plane to be the xy plane. The mirror Chern number is then given by

$$\nu^{(\lambda)}(k_z) = \frac{1}{2\pi} \int dk_x dk_y F_z^\lambda, \quad (5.8)$$

where F_z^λ is integrated over the mirror plane $k_z = 0$ or π . As seen from Eq. (5.8), to change the mirror Chern number, the system needs a gap closing between the negative and the positive energy states with the same mirror eigenvalues. The properties of the mirror Chern numbers vary according to mirror-parity of the gap function. In the mirror-odd (mirror-even) SC, $\nu^{(+i)}$ and $\nu^{(-i)}$ are independent (equal) because each mirror sector has (does not have) its own particle-hole symmetry [121, 122].

Hereafter, by using the above arguments, let us discuss a topological phase transition to realize topological crystalline SC phases in three-dimensional SCs. We set any tunable parameter m , which governs the topological phase transition in the mirror-symmetric SC without time-reversal symmetry. Below, we make the following assumptions: (i) All the states are nondegenerate in the SC. (ii) The mirror symmetries in the SC are invariant by a change of the parameter

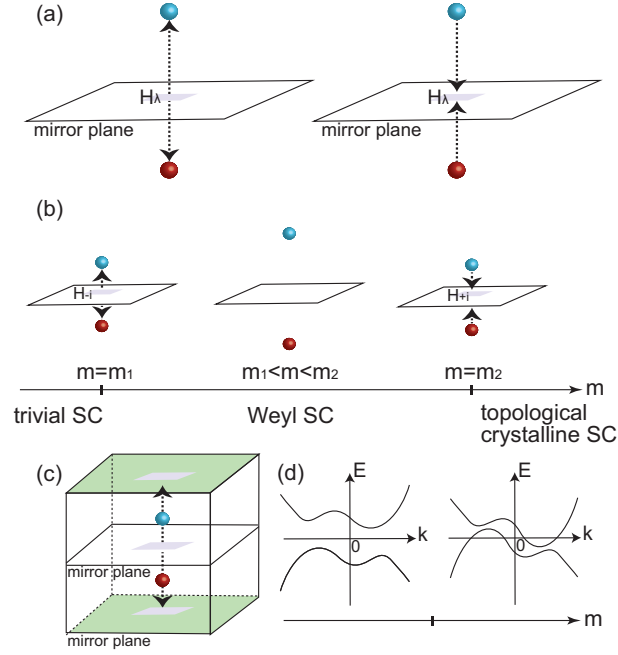


Figure 5.1: (a) The pair creation and annihilation of Weyl nodes in the mirror sector \mathcal{H}_λ . The two colors of the Weyl nodes correspond to opposite monopole charges. Because of the gap closing on the mirror plane, the mirror Chern number $\nu^{(\lambda)}$ changes by ± 1 . (b), (c) Examples of a trajectory formed by one pair of Weyl nodes between trivial and topological crystalline SC phases. (d) Schematic drawing of the band evolution near zero energy in the absence of inversion and time-reversal symmetries. The maximum energy of the hole bands can exceed zero energy.

m . (iii) The SC becomes gapful all over the Brillouin zone within a finite range of the parameter m .

First, we investigate a topological phase transition in odd-parity SCs. The positive and the negative energy bands at \mathbf{k} are symmetric with respect to zero energy due to the particle-hole and inversion symmetries. To see the topological phase transition, we begin with a gapful and trivial SC when $m < m_1$. If the mirror Chern number becomes nonzero while we change the parameter m , a gap closes between two states with the same mirror eigenvalues on the corresponding mirror plane. Now, let us assume that the gap closes at $m = m_1$ in the mirror sector \mathcal{H}_λ . The gap closing not only changes the mirror Chern number $\nu^{(\lambda)}$ but also leads to pair creation of Weyl nodes [Fig. 5.1 (a)]. As $m(> m_1)$ is increased, the Weyl nodes move in the Brillouin zone until the pair annihilation. Consequently, the SC is in the Weyl SC phase. Furthermore, we assume that the SC becomes gapped again after a further change of m annihilates all the

Weyl nodes at $m = m_2$. Whether the gapful SC phase in $m > m_2$ is trivial or topological is determined by the trajectory of the Weyl nodes in the Brillouin zone. To elucidate a relationship between the trajectory and the topological phase transition, suppose that one pair of Weyl nodes is created at $m = m_1$ in the \mathcal{H}_{-i} sector on a mirror plane. Then, the SC system enters the Weyl SC phase with nonzero $\nu^{(-i)}$. If the Weyl nodes return to the \mathcal{H}_{-i} sector on the same mirror plane at $m = m_2$, the mirror Chern number $\nu^{(-i)}$ becomes zero. Thus, the SC phase in $m > m_2$ is trivial. As another example, suppose that the Weyl nodes are pair annihilated at $m = m_2$ in \mathcal{H}_{+i} sector on the same mirror plane as illustrated in Fig. 5.1 (b). Then, the pair annihilation changes $\nu^{(+i)}$, whereas $\nu^{(-i)}$ remains nonzero. As a result, topological crystalline SC phase is realized. In this trajectory, the Chern number $\nu = \nu^{(+i)} + \nu^{(-i)}$ on the mirror plane is zero in the topological crystalline SC phase. Hence, the mirror symmetry is essential for the topological phase transition. Moreover, the Weyl nodes can vanish on another mirror plane. The trajectory also realizes a topological crystalline SC phase with nonzero Chern numbers [Fig. 5.1 (c)]. Generally, there can be more than one pair of Weyl nodes and several mirror planes, and pair creation and annihilation may not occur on the mirror plane. However, changes of mirror Chern numbers accompany pair creation or annihilation on the mirror plane. In this way, the generic topological phase transition can be understood from the trajectories formed by all the Weyl nodes. As a result, the Weyl SC phase can be regarded as an intermediate nodal state between the gapful SC phases with different mirror Chern numbers.

Secondly, we comment on a topological phase transition between trivial and topological crystalline SC phases in noncentrosymmetric SCs. Because the BdG Hamiltonian breaks both time-reversal and inversion symmetries, the maximum energy of the hole bands may be larger than zero [145–147], depending on the parameter m [Fig. 5.1 (d)]. Hence, Weyl nodes formed by the electron and the hole bands can deviate from zero energy in general. Then, the mirror Chern numbers in Eq. (5.8) are not available for characterization of the topological phase because the Berry connection is defined from the negative-energy states. However, we can use the mirror Chern numbers by replacing the sum of the negative states with that of the hole bands in Eq. (5.6) even if the maximum energy of the hole bands exceeds zero energy. The reason is that the mirror Chern number defined by the hole bands are unchanged as long as the gap survives between the hole and the electron bands. Therefore, our theory on trajectories of Weyl nodes is also applicable to the topological phase transition in the mirror-symmetric SCs breaking inversion symmetry.

Finally, we show that the mirror-parity of the gap function restricts the trajectories to realize a topological crystalline SC phase. There is no such restriction on the trajectory in Weyl semimetals without time-reversal symmetry since the mirror-parity is related to particle-hole symmetry [121, 122, 131]. In the following, we clarify the possible trajectories and the behavior of the gap closing, which depend on the mirror-parity of the gap function.

We begin with a SC with a mirror-odd gap function. Since $\nu^{(+i)}$ and $\nu^{(-i)}$ are independent, the topological crystalline SC phase is realizable from the

trajectory as shown in Fig. 5.1 (b). Moreover, when inversion symmetry is present, a gap closing occurs on the mirror plane between the positive and the negative energy states with the same mirror eigenvalues due to particle-hole symmetry in each of the mirror sectors. Namely, the gap closing in the SC necessarily leads to pair creation of Weyl nodes. Next, we consider a topological phase transition in a SC with a mirror-even gap function. Then, $\nu^{(+i)}$ is always equal to $\nu^{(-i)}$, unlike the mirror-odd SC. Thus, pair creation or annihilation in the \mathcal{H}_{+i} sector coincides with that in the \mathcal{H}_{-i} sector. Hence, if the two pairs of the Weyl nodes emerge from the mirror plane and they return to the same mirror plane, the gapful SC becomes topologically trivial again. In order to reach the nontrivial phase, the Weyl nodes need to vanish away from the mirror plane where they have emerged. Additionally, the gap on the mirror plane can close between the two states with opposite mirror eigenvalues since each of the mirror sectors does not keep particle-hole symmetry. The gap closing then yields a nodal line on the mirror plane.

5.3 Model calculation

To demonstrate our theory, we study a SC modeled on a cubic lattice with mirror symmetry. As an example, we consider a BdG Hamiltonian written by $H = \frac{1}{2} \sum_{\mathbf{k}} \Psi_{\mathbf{k}}^\dagger \mathcal{H}(\mathbf{k}) \Psi_{\mathbf{k}}$ with $\Psi_{\mathbf{k}}^\dagger = (c_{\mathbf{k}\uparrow}^\dagger, c_{\mathbf{k}\downarrow}^\dagger, c_{-\mathbf{k}\uparrow}, c_{-\mathbf{k}\downarrow})$ and

$$\mathcal{H}(\mathbf{k}) = \begin{pmatrix} \xi_{\mathbf{k}} - Bs_z & \Delta(\mathbf{k}) \\ \Delta^\dagger(\mathbf{k}) & -\xi_{\mathbf{k}} + Bs_z \end{pmatrix}. \quad (5.9)$$

Here, $\xi_{\mathbf{k}} = 2t_x \cos k_x + 2t_y \cos k_y + 2t_z \cos k_z - \mu$ is a kinetic energy, and $\Delta(\mathbf{k}) = i\mathbf{d} \cdot \mathbf{s} s_y$ is a gap function, with $\mathbf{d} = \Delta(\sin k_x, \sin k_y, \sin k_z)$ and $\mathbf{s} = (s_x, s_y, s_z)$ being the Pauli matrices acting on the spin space. B is an external magnetic field breaking time-reversal symmetry. The eigenvalues are

$$E(\mathbf{k}) = \pm \left[\xi_{\mathbf{k}}^2 + B^2 + \sum_i d_i^2 \pm 2B\sqrt{\xi_{\mathbf{k}}^2 + d_z^2} \right]^{1/2}. \quad (5.10)$$

We note that this model describes an odd-parity SC. This model without the magnetic field is studied as a time-reversal invariant topological SC [148].

Now, the normal state has a mirror symmetry with respect to the xy plane, and the mirror operation is given by $M_z = -is_z$. Thus, the gap function is mirror-odd because $M_z \Delta(k_x, k_y, k_z) M_z^\dagger = -\Delta(k_x, k_y, -k_z)$. The BdG Hamiltonian also has a mirror symmetry described by $\tilde{M}_z = \text{diag}(M_z, M_z)$. Therefore, the mirror Chern numbers $\nu^{(\pm i)}(k_z)$ can be defined on the planes $k_z = 0$ and π in this model.

On the mirror planes, the Hamiltonian can be block-diagonalized in the diagonal basis of \tilde{M}_z . Each mirror sector of the eigenvalues $\pm i$ is described by

$$\mathcal{H}_{\pm i}(\mathbf{k}) = \pm \Delta \sin k_x \tau_x - \Delta \sin k_y \tau_y + [\xi_{\mathbf{k}} \pm B] \tau_z, \quad (5.11)$$

where $\tau_{x,y,z}$ are the Pauli matrices. According to Eq. (5.11), the mirror Chern numbers change when $\xi_{\mathbf{k}} \pm B = 0$ on the mirror planes.

Figure 5.2 (a) and (b) show phase diagrams in this model with $\Delta = 0.3t_z$ and $0.1t_z$, respectively. Both of the phase diagrams are obtained when $\mu = 0.25t_z$ and $B = 0.05t_z$. For example, we see the topological phase transition along the $t_y = t_x$ line represented by the arrow in the phase diagram of Fig. 5.2 (a). The band evolution is shown in Fig. 5.2 (c). When $t_y = 0.425t_z$, the pair creation happens at $\mathbf{k} = (\pi, \pi, 0)$ in the \mathcal{H}_{-i} sector. The Weyl nodes move along the line $\mathbf{k} = (\pi, \pi, k_z)$ as $t_y (= t_x)$ becomes larger. Eventually, the Weyl nodes are pair-annihilated at $\mathbf{k} = (\pi, \pi, 0)$ in the \mathcal{H}_{+i} sector when $t_y = 0.45t_z$. The trajectory is identical to that in Fig. 5.1 (b), realizing the topological crystalline SC phase.

Moreover, we see a topological phase transition for $\Delta = 0.1t_z$. We also consider band evolution along $t_y = t_x$ line in Fig. 5.2 (b). When $t_y = 0.37t_z$, four Weyl nodes emerge at points on the $\mathbf{k} = (\pi, \pi, k_z)$ line but not on the mirror plane. When we increase $t_y = t_x$, the one pair vanishes in the \mathcal{H}_{-i} sector, and then the other pair does in the \mathcal{H}_{+i} sector. This trajectory also realizes a topological crystalline SC phase because the two pairs vanish in the different mirror sectors. Therefore, in both cases, the SC system enters into the topological crystalline SC phase via the Weyl SC phase, which is consistent with our theory.

5.4 Evolution of Majorana surface states: from Majorana arc to Majorana cone

Topological SCs generally exhibit surface states protected topologically. Therefore, we here discuss evolutions of the topological surface states and the bulk states in a topological phase transition between Weyl and topological crystalline SC phases. To understand how the surface states evolve, we use the SC model with the mirror-odd gap function described by Eq. (5.9). In general, Weyl SCs have Majorana arc states on the surface [124, 126, 127]. The Majorana arc states lie between projections of Weyl nodes with opposite monopole charges onto the surface. On the other hand, topological crystalline SCs show Majorana surface states when the gap function is mirror-odd [121, 122, 131].

We calculate surface states for a slab with a (100) surface to preserve mirror symmetry of the model. We choose the same parameters $\mu = 0.25t_z$ and $B = 0.05t_z$ as used in the previous subsection [Fig. 5.2 (a) and (b)]. We also investigate the evolution of the surface states along the $t_y = t_x$ line described by the arrows in the phase diagrams. Figure 5.3 (a) and (b) show evolutions of the surface bands on the line $\mathbf{k} = (k_y = \pi, k_z)$ of the model when $\Delta = 0.3t_z$ and $0.1t_z$, respectively. First, we see the band evolutions of the surface states when $\Delta = 0.3t_z$, as shown in Fig. 5.3 (a). If the system enters the Weyl SC phase from the trivial SC phase, Majorana arc states appear between the projections of the Weyl nodes which have emerged from the mirror plane. The Majorana arc extends after the phase transition between the trivial and the Weyl SC phases.

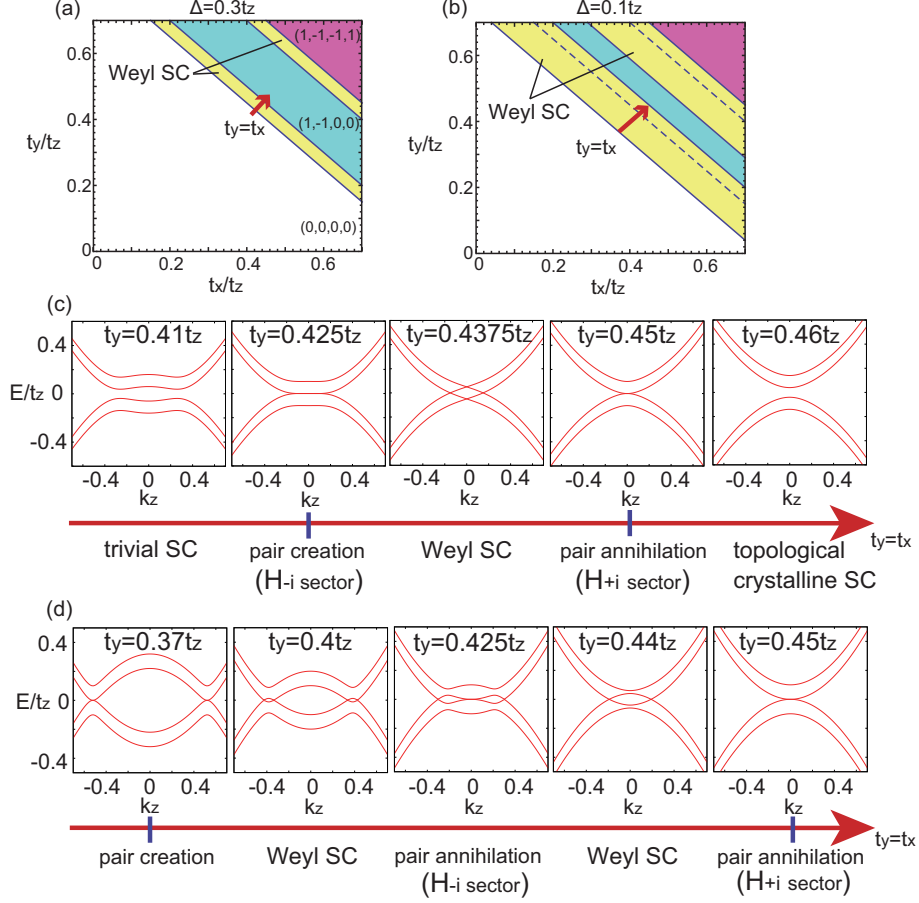


Figure 5.2: (a) The phase diagram with $\mu = 0.25t_z$, $B = 0.05t_z$ and $\Delta = 0.3t_z$. The blue and the purple regions are SC phases with the nonzero mirror Chern numbers $(\nu^{(+i)}(0), \nu^{(-i)}(0), \nu^{(+i)}(\pi), \nu^{(-i)}(\pi)) = (1, -1, 0, 0)$ and $(1, -1, -1, 1)$, respectively. The yellow regions are Weyl SC phases. (b) The same as (a) with $\mu = 0.25t_z$, $B = 0.05t_z$ and $\Delta = 0.1t_z$. The dashed lines represent the parameters where a pair annihilation happens on the mirror plane while the system remains in the Weyl SC phase. (c), (d) Band evolutions of the SC on the line $\mathbf{k} = (\pi, \pi, k_z)$ along the arrows in (a) and (b). The arrows in the phase diagrams indicate the line $t_y = t_x$. In (c), the mirror Chern number $\nu^{(-i)}(0)(\nu^{(+i)}(0))$ changes at $t_y = 0.425t_z(0.45t_z)$. The Weyl node at $\pm k_z$ ($k_z > 0$) has monopole charge ± 1 . In (d), the pair creation happens at $t_y = 0.37t_z$. The Weyl nodes at k_z^1 and k_z^2 ($k_z^1 > k_z^2 > 0$) have monopole charges -1 and $+1$.

As the system approaches the topological crystalline SC phase, the Majorana arc gradually shortens. When the phase transition occurs between the Weyl and the topological crystalline SC phases, the Majorana arc disappears by pair annihilation of the Weyl nodes. Nevertheless, the Majorana surface states survive because the mirror Chern numbers are nonzero on the bulk $k_z = 0$ plane.

Next, we consider the evolution of the surface states when $\Delta = 0.1t_z$ [Fig. 5.3 (b)]. Because the four Weyl nodes emerge in the bulk in the Weyl SC phase, two Majorana arcs can be found. When we increase the parameter along the $t_y = t_x$ line, the four Weyl nodes move toward the mirror plane $k_z = 0$. The four Weyl nodes vanish on the mirror plane when the SC shows a transition from the Weyl SC phase to the topological crystalline SC phase. Then, the emergent Majorana arcs disappear by the pair annihilations on the mirror plane. Eventually, the Majorana surface states remain at $k_z = 0$ in the topological crystalline SC phase. Therefore, we can see that the shrinking Majorana arcs turn into the Majorana states in the topological crystalline SC phases, although the trajectories of the Weyl nodes are different for $\Delta = 0.3t_z$ and $0.1t_z$.

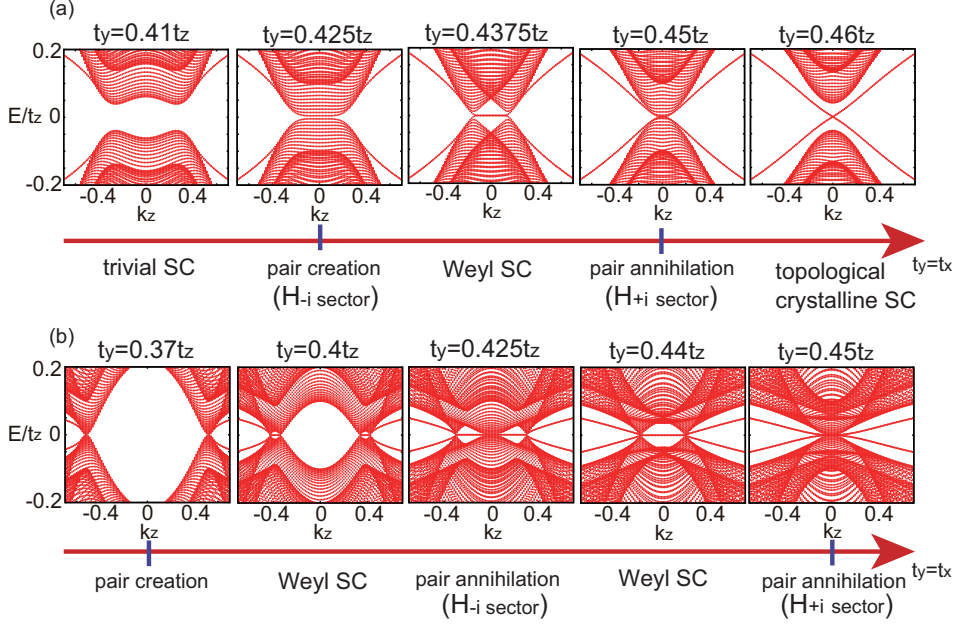


Figure 5.3: (a) and (b) Surface band evolutions on the line $\mathbf{k} = (\pi, k_z)$ along the arrow $t_y = t_x$ in Fig. 5.2 (a) and (b).

5.5 Conclusion and discussion

In the present chapter, we have investigated Weyl superconductivity in mirror symmetric superconductors without time-reversal symmetry. We have shown that Weyl superconductivity universally emerges between the trivial and the topological crystalline superconductor phases in odd-parity and in noncentrosymmetric superconductors. We have also discussed a relationship between the Weyl nodes and the topological phase transition. It is shown that trajectories of the Weyl nodes determine the topological phase after the pair annihilation.

Our generic results are applicable to various unconventional superconductors breaking time-reversal symmetry because many crystals have mirror symmetry. Thus, the theory is useful for prediction of Weyl and topological crystalline superconductors in addition to theoretical construction of the topological phase diagram. For example, recent papers have shown that an external magnetic field moves Weyl nodes in the Brillouin zone [57, 149]. As shown in our model calculation, changing shapes of Fermi surfaces in the normal state can also induce the topological phase transition, which is expected to occur by means of doping and pressure. Hence, the topological phase transition predicted in this thesis can be realized by controlling these parameters experimentally.

Chapter 6

Summary and Outlook

In this thesis, we studied various topological phases of quantum matters. We established general theories of the topological phase transitions for topological semimetals and gapless superconductors. We also elucidate relationships between the band structures and the topological phase transitions. We summarize our results as follows.

In Chapter 3, we focused on a relationship between surface states and topological phase transitions from the Weyl semimetal to the \mathbb{Z}_2 topological insulator. By using an effective model and a lattice model which describe the topological phase transition, we revealed generic dispersions of the Weyl semimetals. Moreover, we found that two Fermi arcs merge into one Dirac cone when the topological phase transition happens from the Weyl semimetal phase to the \mathbb{Z}_2 topological insulator phase experimentally. We also demonstrated that connectivity of the Fermi arcs changes if the surface termination is changed.

Especially, our calculation is also useful to investigate the topological phase transition between the time-reversal invariant Weyl semimetal phase and the \mathbb{Z}_2 topological insulator phase. Because the topological surface states are one of characteristics of the topological materials, measurement of the surface band structures is a strong means to determine the phase of the matter. On the other hand, the results in Chapter 3 show how the surface states evolve when the system moves from the Weyl semimetal phase to the \mathbb{Z}_2 topological insulator phase. If the topological phase transition can be induced experimentally, which will be realizable by controlling composition ratio of the compounds comprising the crystal for instance, the evolution of the surface states can be compared with our theory to observe the topological phase transition.

In Chapter 4, we presented a general theory of the topological phase transition between the topological nodal-line semimetal and the Weyl semimetal in the spinless system. It is shown that breaking of time-reversal symmetry necessarily creates spinless Weyl nodes if the nodal line encloses one time-reversal invariant momenta. Furthermore, we showed that when crystal symmetries protect the nodal-line, the gapless phase can survive even if the inversion symmetry is broken. Meanwhile, we clarified a relationship between crystal symmetries and

band structures of the nodal lines.

The results in Chapter 4 give a generic framework to search for the spinless Weyl semimetal phases experimentally. Until now, there are no experimental reports about the spinless Weyl semimetals. Thus, we expect our universal theory to help us realize the spinless Weyl semimetal. In addition, our results are applicable not only in electronic systems with negligible spin-orbit interaction but also in generic spinless systems such as photon, phonon, magnon and so on. Therefore, Weyl physics will be seen in the nonelectronic systems without spin-orbit interaction by using our theory.

In Chapter 5, we constructed a universal topological phase diagram for Weyl superconductivity in the mirror-symmetric superconductors without time-reversal symmetry. As a result, we found that the Weyl superconductor phase universally emerges between the trivial and the topological crystalline superconductor phases in the odd-parity and in the noncentrosymmetric superconductors. We also investigated the band evolution when the topological phase transitions occurs among the trivial, the Weyl and the topological crystalline superconductor phases.

The Weyl superconductors are typically difficult to predict from crystal symmetries as with Weyl semimetals since their Weyl nodes are created by accidental band touching in the three-dimensional system. However, our theory guarantees that the Weyl superconductor phase necessarily intervenes between the trivial and the topological crystalline superconductor phases in the odd-parity superconductors and in the noncentrosymmetric ones without time-reversal symmetry. This theory is valid as long as all the states are nondegenerate in the superconductor, and the nondegenerate states can be allowed by strong spin-orbit interaction in inversion-asymmetric systems and by the Zeeman effect. Thus, we expect that our results can describe the topological phase transition in many mirror-symmetric superconductors.

Our general results are widely available for prediction of the topological materials because our theory is completely based on symmetry and topology, independent of details of the system. The theory is beneficial for realization of the topological phase transitions as suggested in this thesis, which is observable by direct observation of the band structure. Moreover, the experimental realization can lead to elucidation of new properties of the topological matters through measurement of the transport phenomena. Hence, we expect that our results in this thesis will contribute to further progress and deeper understanding in the field of the topological materials.

Appendix A

Classification of the type-A TNLs and their band structures

We have classified type-A TNLs into the two cases (I) and (II) in Sec. 4.3. The classification provides us with information on band evolutions and phase transitions involving the type-A TNLs. In this appendix, we explain band structures of type-A TNLs in the two cases (I) and (II). The type-A TNLs are formed by two bands with opposite parity eigenvalues at the TRIM, and they can be described by the two-band effective Hamiltonian by Eq. (4.1). Here, to describe the TNLs by the two-band effective Hamiltonian, we assume that the TNLs are formed only by two nondegenerate states. In fact, a similar two-band effective Hamiltonian has been used in spinful WSMs in order to describe band evolutions in Ref. [69], and therefore, here we can extend the analysis in Ref. [69] to some of the spinless TNLSMs as well. In Ref. [69], it is shown that when two bands touch each other on high-symmetry lines or planes, emergent gapless nodes evolve along the lines and the planes where the two bands have the different eigenvalues. These results are also discussed in Sec. 2.2.5. By using these results, we can understand band structures of the type-A TNLs.

For example, in Sec. 4.3 we introduced two cases (II)-(i) and (ii) for type-A TNLs, formed by two bands with C_2 and M symmetry. These two cases are classified according to the C_2 and M eigenvalues at the TRIM, and the effective Hamiltonian for the two cases are constrained by these two symmetries. For simplicity, we set the C_2 axis and the M plane to be the z axis and xy plane, respectively. From the constraints, we obtain $\sigma_z H_{\text{TNL}}(-q_x, -q_y, q_z) \sigma_z = H_{\text{TNL}}(q_x, q_y, q_z)$ in the case (II)-(i). Meanwhile, in the case (II)-(ii), we obtain $\sigma_z H_{\text{TNL}}(q_x, q_y, -q_z) \sigma_z = H_{\text{TNL}}(q_x, q_y, q_z)$. Although eigenvalues of the C_2 and M symmetries are different in spinless and spinful systems, the expressions for these constraints are the same both in spinless and in spinful cases [69]. As a result, the type-A TNL of the case (II)-(i) crosses the C_2 axis while the type-A

TNL of the case (II)-(ii) appears on the M plane, both in spinless and in spinful systems. In some cases, several type-A TNLs can enclose the same TRIM if a little group at the TRIM contains some C_2 and M symmetries.

There are various options for the little group at the TRIM, which affects the position of the type-A TNLs. (I) refers to the case where the TRIM is neither C_2 - nor M -symmetric. Therefore, the little group is C_i or C_{3i} . In this case (I), the type-A TNL does not necessarily cross high-symmetry lines. For example, if the two bands have the same C_3 eigenvalues at the TRIM whose little group is C_{3i} , the type-A TNL lies at a general position.

(II) refers to the case where the TRIM is C_2 - and M -symmetric. In this case, as we have shown in Sec. 4.3, the type-A TNLs necessarily cross the high-symmetry lines or appear on the mirror-invariant planes, thanks to symmetry protection. The little groups can also have rotational symmetries besides the C_2 symmetry. When the conduction and the valence bands belong to different subspaces of the C_n -rotational symmetries, the type-A TNLs can intersect the high-symmetry lines. On the other hand, when the two bands belong to different subspaces of the mirror symmetry, the type-A TNLs are on the mirror-invariant plane. In particular, if the eigenvalues of the C_4 or C_6 symmetry are the same, the type-A TNL exists on the mirror-invariant plane perpendicular to the C_4 - or C_6 -invariant axes because $(C_4)^2 = C_2$ and $(C_6)^3 = C_2$.

Here we comment on TNLs in systems with a nonsymmorphic space group having twofold screw (S_2) symmetries or glide (G) symmetries. Inside the Brillouin zone, the TNLs are similar to those with a symmorphic space group, because there is no extra degeneracy due to nonsymmorphic symmetry together with TR symmetry. Meanwhile, S_2 and G symmetries may give rise to extra degeneracy on the Brillouin zone boundary by TR symmetry, if the square of the symmetry operations becomes -1 . For example, by combinations of several G symmetries and the TR symmetry, spinless nodal lines can contain fourfold-degenerate points at the TRIM on the surface of the Brillouin zone [150]. As another example, a nodal surface appears on the ΘS_2 -invariant plane on the surface of the Brillouin zone [151]. Such cases are beyond the scope of this thesis because the band crossing cannot be described by the two-band effective Hamiltonian.

References

- [1] K. v. Klitzing, G. Dorda, and M. Pepper, Phys. Rev. Lett. **45**, 494 (1980).
- [2] C. L. Kane and E. J. Mele, Phys. Rev. Lett. **95**, 226801 (2005).
- [3] C. L. Kane and E. J. Mele, Phys. Rev. Lett. **95**, 146802 (2005).
- [4] M. König et al., Science **318**, 766 (2007).
- [5] M. Z. Hasan and C. L. Kane, Rev. Mod. Phys. **82**, 3045 (2010).
- [6] X.-L. Qi and S.-C. Zhang, Rev. Mod. Phys. **83**, 1057 (2011).
- [7] A. P. Schnyder, S. Ryu, A. Furusaki, and A. W. W. Ludwig, Phys. Rev. B **78**, 195125 (2008).
- [8] S. Murakami, New J. Phys. **9**, 356 (2007).
- [9] X. Wan, A. M. Turner, A. Vishwanath, and S. Y. Savrasov, Phys. Rev. B **83**, 205101 (2011).
- [10] L. Fu, Phys. Rev. Lett. **106**, 106802 (2011).
- [11] T. H. Hsieh et al., Nat. Commun. **3**, 982 (2012).
- [12] C.-K. Chiu, J. C. Y. Teo, A. P. Schnyder, and S. Ryu, Rev. Mod. Phys. **88**, 035005 (2016).
- [13] S. Jia, S.-Y. Xu, and M. Z. Hasan, Nat. Mater. **15**, 1140 (2016).
- [14] M. Sato and S. Fujimoto, J. Phys. Soc. Jpn **85**, 072001 (2016).
- [15] M. Sato and Y. Ando, Reports on Progress in Physics **80**, 076501 (2017).
- [16] A. A. Burkov, Journal of Physics: Condensed Matter **27**, 113201 (2015).
- [17] R. Okugawa and S. Murakami, Phys. Rev. B **89**, 235315 (2014).
- [18] R. Okugawa and S. Murakami, Phys. Rev. B **96**, 115201 (2017).
- [19] R. Okugawa and T. Yokoyama, arXiv:1709.01101 (2017).

- [20] F. D. M. Haldane, Phys. Rev. Lett. **61**, 2015 (1988).
- [21] C.-Z. Chang et al., Science **340**, 167 (2013).
- [22] D. J. Thouless, M. Kohmoto, M. P. Nightingale, and M. den Nijs, Phys. Rev. Lett. **49**, 405 (1982).
- [23] M. V. Berry, Proceedings of the Royal Society of London A: Mathematical, Physical and Engineering Sciences **392**, 45 (1984).
- [24] M. Kohmoto, Annals of Physics **160**, 343 (1985).
- [25] M. Oshikawa, Phys. Rev. B **50**, 17357 (1994).
- [26] Y. Hatsugai, Phys. Rev. Lett. **71**, 3697 (1993).
- [27] B. A. Bernevig, T. L. Hughes, and S.-C. Zhang, Science **314**, 1757 (2006).
- [28] L. Fu and C. L. Kane, Phys. Rev. B **76**, 045302 (2007).
- [29] H. Zhang et al., Nat. Phys. **5**, 438 (2009).
- [30] D. Hsieh et al., Nature **452**, 970 (2008).
- [31] Y. Xia et al., Nat. Phys. **5**, 398 (2009).
- [32] J. E. Moore and L. Balents, Phys. Rev. B **75**, 121306 (2007).
- [33] L. Fu and C. L. Kane, Phys. Rev. B **74**, 195312 (2006).
- [34] L. Fu, C. L. Kane, and E. J. Mele, Phys. Rev. Lett. **98**, 106803 (2007).
- [35] R. Roy, Phys. Rev. B **79**, 195322 (2009).
- [36] R. Roy, Phys. Rev. B **79**, 195321 (2009).
- [37] J. C. Y. Teo, L. Fu, and C. L. Kane, Phys. Rev. B **78**, 045426 (2008).
- [38] S. Murakami, S. Iso, Y. Avishai, M. Onoda, and N. Nagaosa, Phys. Rev. B **76**, 205304 (2007).
- [39] B. Q. Lv et al., Phys. Rev. X **5**, 031013 (2015).
- [40] B. Q. Lv et al., Nat. Phys. **11**, 724 (2015).
- [41] S.-Y. Xu et al., Nat. Phys. **11**, 748 (2015).
- [42] L. Yang et al., Nat. Phys. **11**, 728 (2015).
- [43] S.-Y. Xu et al., Sci. Adv. **1**, e1501092 (2015).
- [44] N. Xu et al., Nat. Commun. **7**, 11006 (2016).
- [45] H. Weng, C. Fang, Z. Fang, B. A. Bernevig, and X. Dai, Phys. Rev. X **5**, 011029 (2015).

- [46] S.-M. Huang et al., Nat. Commun. **6**, 7373 (2015).
- [47] K.-Y. Yang, Y.-M. Lu, and Y. Ran, Phys. Rev. B **84**, 075129 (2011).
- [48] G. Xu, H. Weng, Z. Wang, X. Dai, and Z. Fang, Phys. Rev. Lett. **107**, 186806 (2011).
- [49] Z. Wang et al., Phys. Rev. Lett. **117**, 236401 (2016).
- [50] H. Yang et al., New J. Phys. **19**, 015008 (2017).
- [51] M. Ikhlas et al., Nat. Phys. **13**, 1085 (2017).
- [52] K. Kuroda et al., Nat. Mater. **16**, 1090 (2017).
- [53] S. Murakami and S.-i. Kuga, Phys. Rev. B **78**, 165313 (2008).
- [54] S. M. Young et al., Phys. Rev. Lett. **108**, 140405 (2012).
- [55] Z. Wang et al., Phys. Rev. B **85**, 195320 (2012).
- [56] Z. Wang, H. Weng, Q. Wu, X. Dai, and Z. Fang, Phys. Rev. B **88**, 125427 (2013).
- [57] B.-J. Yang and N. Nagaosa, Nat. Commun. **5**, 4898 (2014).
- [58] Z. Liu et al., Science **343**, 864 (2014).
- [59] Z. Liu et al., Nat. Mater. **13**, 677 (2014).
- [60] S.-Y. Xu et al., Science **347**, 294 (2015).
- [61] S. Borisenko et al., Phys. Rev. Lett. **113**, 027603 (2014).
- [62] A. A. Burkov and L. Balents, Phys. Rev. Lett. **107**, 127205 (2011).
- [63] T. Ojanen, Phys. Rev. B **87**, 245112 (2013).
- [64] H. Nielsen and M. Ninomiya, Nuclear Physics B **185**, 20 (1981).
- [65] H. Nielsen and M. Ninomiya, Nuclear Physics B **193**, 173 (1981).
- [66] J. Liu and D. Vanderbilt, Phys. Rev. B **90**, 155316 (2014).
- [67] M. Bahrany, B.-J. Yang, R. Arita, and N. Nagaosa, Nat. Commun. **3**, 679 (2011).
- [68] B.-J. Yang et al., Phys. Rev. Lett. **110**, 086402 (2013).
- [69] S. Murakami, M. Hirayama, R. Okugawa, and T. Miyake, Sci. Adv. **3**, e1602680 (2017).
- [70] M. Hirayama, R. Okugawa, S. Ishibashi, S. Murakami, and T. Miyake, Phys. Rev. Lett. **114**, 206401 (2015).

- [71] C. Herring, Phys. Rev. **52**, 361 (1937).
- [72] H. Weng et al., Phys. Rev. B **92**, 045108 (2015).
- [73] H. Huang, J. Liu, D. Vanderbilt, and W. Duan, Phys. Rev. B **93**, 201114 (2016).
- [74] C. Fang, Y. Chen, H.-Y. Kee, and L. Fu, Phys. Rev. B **92**, 081201 (2015).
- [75] M. Hirayama, R. Okugawa, T. Miyake, and S. Murakami, Nat. Commun. **8**, 14022 (2017).
- [76] L. M. Schoop et al., Nat. Commun. **7**, 11696 (2016).
- [77] M. Neupane et al., Phys. Rev. B **93**, 201104 (2016).
- [78] J. Hu et al., Phys. Rev. Lett. **117**, 016602 (2016).
- [79] X. Wang et al., Advanced Electronic Materials **2**, 1600228 (2016).
- [80] R. Singha, A. K. Pariari, B. Satpati, and P. Mandal, Proc. Nat. Acad. Sci. **114**, 2468 (2017).
- [81] Y. Chen et al., Nano lett. **15**, 6974 (2015).
- [82] J.-T. Wang et al., Phys. Rev. Lett. **116**, 195501 (2016).
- [83] L. S. Xie et al., APL Materials **3**, 083602 (2015).
- [84] Y.-H. Chan, C.-K. Chiu, M. Y. Chou, and A. P. Schnyder, Phys. Rev. B **93**, 205132 (2016).
- [85] R. Li et al., Phys. Rev. Lett. **117**, 096401 (2016).
- [86] Y. Kim, B. J. Wieder, C. L. Kane, and A. M. Rappe, Phys. Rev. Lett. **115**, 036806 (2015).
- [87] R. Yu, H. Weng, Z. Fang, X. Dai, and X. Hu, Phys. Rev. Lett. **115**, 036807 (2015).
- [88] M. Zeng et al., arXiv:1504.03492 (2015).
- [89] J. Zhao, R. Yu, H. Weng, and Z. Fang, Phys. Rev. B **94**, 195104 (2016).
- [90] Q. Xu, R. Yu, Z. Fang, X. Dai, and H. Weng, Phys. Rev. B **95**, 045136 (2017).
- [91] G. P. Mikitik and Y. V. Sharlai, Phys. Rev. Lett. **82**, 2147 (1999).
- [92] T. Kariyado and Y. Hatsugai, Phys. Rev. B **88**, 245126 (2013).
- [93] J. N. Fuchs, F. Piéchon, M. O. Goerbig, and G. Montambaux, Eur. Phys. J. B **77**, 351 (2010).

- [94] J. Zak, Phys. Rev. Lett. **62**, 2747 (1989).
- [95] R. D. King-Smith and D. Vanderbilt, Phys. Rev. B **47**, 1651 (1993).
- [96] R. Okugawa, J. Tanaka, T. Koretsune, S. Saito, and S. Murakami, Phys. Rev. Lett. **115**, 156601 (2015).
- [97] M. Hirayama, R. Okugawa, and S. Murakami, arXiv:1708.05791 (2017).
- [98] D. Vanderbilt and R. D. King-Smith, Phys. Rev. B **48**, 4442 (1993).
- [99] S. Ryu and Y. Hatsugai, Phys. Rev. Lett. **89**, 077002 (2002).
- [100] A. Yamakage, Y. Yamakawa, Y. Tanaka, and Y. Okamoto, J. Phys. Soc. Jpn **85**, 013708 (2016).
- [101] Y. Okamoto, T. Inohara, A. Yamakage, Y. Yamakawa, and K. Takenaka, J. Phys. Soc. Jpn **85**, 123701 (2016).
- [102] J. L. Mañes, Phys. Rev. B **85**, 155118 (2012).
- [103] C. Fang, M. J. Gilbert, X. Dai, and B. A. Bernevig, Phys. Rev. Lett. **108**, 266802 (2012).
- [104] L. Lu, L. Fu, J. D. Joannopoulos, and M. Soljačić, Nat. photon. **7**, 294 (2013).
- [105] J.-Y. Zou and B.-G. Liu, Phys. Rev. B **93**, 205435 (2016).
- [106] L. Lu et al., Science **349**, 622 (2015).
- [107] W.-J. Chen, M. Xiao, and C. T. Chan, Nat. Commun. **7**, 13038 (2016).
- [108] A. Alexandradinata, C. Fang, M. J. Gilbert, and B. A. Bernevig, Phys. Rev. Lett. **113**, 116403 (2014).
- [109] H. Kim and S. Murakami, Phys. Rev. B **93**, 195138 (2016).
- [110] A. Narayan, Phys. Rev. B **94**, 041409 (2016).
- [111] Z. Yan and Z. Wang, Phys. Rev. Lett. **117**, 087402 (2016).
- [112] C.-K. Chan, Y.-T. Oh, J. H. Han, and P. A. Lee, Phys. Rev. B **94**, 121106 (2016).
- [113] K. Taguchi, D.-H. Xu, A. Yamakage, and K. T. Law, Phys. Rev. B **94**, 155206 (2016).
- [114] M. Ezawa, Phys. Rev. B **96**, 041205 (2017).
- [115] Z. Yan and Z. Wang, Phys. Rev. B **96**, 041206 (2017).
- [116] S. Kobayashi, K. Shiozaki, Y. Tanaka, and M. Sato, Phys. Rev. B **90**, 024516 (2014).

- [117] S. Kobayashi, Y. Yanase, and M. Sato, Phys. Rev. B **94**, 134512 (2016).
- [118] M. Sato, Phys. Rev. B **81**, 220504 (2010).
- [119] L. Fu and E. Berg, Phys. Rev. Lett. **105**, 097001 (2010).
- [120] S. Sasaki et al., Phys. Rev. Lett. **107**, 217001 (2011).
- [121] Y. Ueno, A. Yamakage, Y. Tanaka, and M. Sato, Phys. Rev. Lett. **111**, 087002 (2013).
- [122] K. Shiozaki and M. Sato, Phys. Rev. B **90**, 165114 (2014).
- [123] N. Read and D. Green, Phys. Rev. B **61**, 10267 (2000).
- [124] T. Meng and L. Balents, Phys. Rev. B **86**, 054504 (2012).
- [125] S. A. Yang, H. Pan, and F. Zhang, Phys. Rev. Lett. **113**, 046401 (2014).
- [126] J. D. Sau and S. Tewari, Phys. Rev. B **86**, 104509 (2012).
- [127] M. A. Silaev and G. E. Volovik, Phys. Rev. B **86**, 214511 (2012).
- [128] M. Sato, Phys. Rev. B **73**, 214502 (2006).
- [129] F. Zhang, C. L. Kane, and E. J. Mele, Phys. Rev. Lett. **111**, 056403 (2013).
- [130] T. Morimoto and A. Furusaki, Phys. Rev. B **88**, 125129 (2013).
- [131] C.-K. Chiu and A. P. Schnyder, Phys. Rev. B **90**, 205136 (2014).
- [132] K. T. Law, P. A. Lee, and T. K. Ng, Phys. Rev. Lett. **103**, 237001 (2009).
- [133] K. Flensberg, Phys. Rev. B **82**, 180516 (2010).
- [134] M. Sigrist and K. Ueda, Rev. Mod. Phys. **63**, 239 (1991).
- [135] E. D. Bauer, N. A. Frederick, P.-C. Ho, V. S. Zapf, and M. B. Maple, Phys. Rev. B **65**, 100506 (2002).
- [136] V. Kozii, J. W. F. Venderbos, and L. Fu, Sci. Adv. **2**, e1601835 (2016).
- [137] R. Takahashi and S. Murakami, Phys. Rev. B **88**, 235303 (2013).
- [138] C. Bradley and A. Cracknell, *The mathematical theory of symmetry in solids: representation theory for point groups and space groups*, Oxford University Press, 2010.
- [139] Y. X. Zhao, A. P. Schnyder, and Z. D. Wang, Phys. Rev. Lett. **116**, 156402 (2016).
- [140] D. F. Agterberg, P. M. R. Brydon, and C. Timm, Phys. Rev. Lett. **118**, 127001 (2017).

- [141] C. Timm, A. P. Schnyder, D. F. Agterberg, and P. M. R. Brydon, Phys. Rev. B **96**, 094526 (2017).
- [142] T. Bzdušek and M. Sigrist, Phys. Rev. B **96**, 155105 (2017).
- [143] O. Türker and S. Moroz, arXiv:1709.01561 (2017).
- [144] C.-K. Chiu, H. Yao, and S. Ryu, Phys. Rev. B **88**, 075142 (2013).
- [145] C. L. M. Wong, J. Liu, K. T. Law, and P. A. Lee, Phys. Rev. B **88**, 060504 (2013).
- [146] L. Hao and C. S. Ting, Phys. Rev. B **94**, 134513 (2016).
- [147] A. Daido and Y. Yanase, Phys. Rev. B **95**, 134507 (2017).
- [148] M. Sato, Phys. Rev. B **79**, 214526 (2009).
- [149] A. Daido and Y. Yanase, Phys. Rev. B **94**, 054519 (2016).
- [150] R. Takahashi, M. Hirayama, and S. Murakami, Phys. Rev. B **96**, 155206 (2017).
- [151] Q.-F. Liang, J. Zhou, R. Yu, Z. Wang, and H. Weng, Phys. Rev. B **93**, 085427 (2016).

List of Publications and Preprints

List of Publications

- (1) R. Okugawa and S. Murakami, “Dispersion of Fermi arcs in Weyl semimetals and their evolutions to Dirac cones”, *Phys. Rev. B*, **89**, 235315 (2014).
- (2) M. Hirayama, R. Okugawa, S. Ishibashi, S. Muarkami and T. Miyake, “Weyl Node and Spin Texture in Trigonal Tellurium and Selenium”, *Phys. Rev. Lett.* **114**, 206401 (2015).
- (3) R. Okugawa, J. Tanaka, T. Koretsune, S. Saito and S. Murakami, “In-Plane Electric Polarization of Bilayer Graphene Nanoribbons Induced by an Interlayer Bias Voltage”, *Phys. Rev. Lett.* **115**, 156601 (2015).
- (4) M. Hirayama, R. Okugawa, T. Miyake and S. Murakami, “Topological Dirac nodal lines and surface charges in fcc alkaline earth metals”, *Nat. Commun.* **8** 14022 (2017).
- (5) S. Murakami, M. Hirayama, R. Okugawa and T. Miyake, “Emergence of topological semimetals in gap closing in semiconductors without inversion symmetry”, *Sci. Adv.* **3**, e1602680 (2017).
- (6) R. Okugawa and S. Murakami “Universal phase transition and band structures for spinless nodal-line and Weyl semimetals”, *Phys. Rev. B* **96**, 115201 (2017).

List of Preprints

- (7) R. Okugawa and T. Yokoyama, “Generic phase diagram for Weyl superconductivity in mirror-symmetric superconductors”, *arXiv:1709.01101* (2017)

Chapters 3, 4 and 5 in this thesis are based on the author's papers (1), (6) and (7), respectively.